

The Applied Tomography Experiment of 1990

Technical Report
APL-UW TR9106
28 February 1991



Applied Physics Laboratory University of Washington
1013 NE 40th Street Seattle, Washington 98105-6698

Contract N00039-88-C-0054
Approved for public release; distribution is unlimited.

PREFACE

This report has been a joint effort. Mike Carnes at the Naval Oceanographic and Atmospheric Research Laboratory contributed to the sections "Comparisons with AXBT Data" and "Comparisons with OTIS Fields," and Steve Foster at the Institute for Naval Oceanography contributed to the section "Comparisons with OOC Fronts."

ACKNOWLEDGMENTS

The Applied Tomography Experiment of 1990 included many participants:

Kurt Metzger from the University of Michigan was responsible for the receiving equipment and the signal-processing software. Ted Birdsall assisted during the "turn-on" period.

Peter Worcester and Bruce Cornuelle at the Scripps Institution of Oceanography provided the source instrumentation and much of the analysis software. Steve Abbott, Kevin Hardy, David Horwitt, Betty Ma, Doug Peckham, and Bob Truesdale assisted.

Jim Cummings, Ken Pollack, and Mike Clancy at the Fleet Numerical Oceanography Center provided the output of the FNOC Optimal Thermal Interpolation System.

Jimmy Mitchell coordinated the effort by the Naval Oceanographic and Atmospheric Research Laboratory. Janice Boyd obtained the AXBT data. Mike Carnes, Don Johnson, Donna Blake, and Dan Fox analyzed some of the data. David King, Linda Knauer (from PSI), and Lucy Fitzgerald (from Sverdrup) assisted.

Steve Foster, Lannie Yeskie, and Jim Corbin at the Institute for Naval Oceanography (INO) provided independent data analysis. Valentine Anantharaj of INO organized the data inventory, and Bob Wilms of INO organized the Workshop on Tomographic Data in Ocean Models, a spin-off of this project.

Chris Hall and Phil Bylsma provided support from the Operational Oceanography Center.

Larry Mendlow and Maureen Smith from the Naval Facilities Engineering Command, Chesapeake Division, and the captain and crew of OCP *Seacon* helped install the acoustic sources off Bermuda.

Peggy Haeger at the Naval Oceanographic Office provided initial acoustic predictions, and Frank Marchant and Vytautas Aleksandravicius provided the necessary charts.

Bruce Williams at the Naval Ocean Systems Center provided acoustic modeling support.

The captain and crew of USNS *Bold* provided support in taking measurements with a towed array.

Navy personnel at the Navy facilities, AT&T, and PMW181 went out of their way to support us. Capt. Coen and Lt. Cmdr. Hughes at OP-024 and Capt. John Parrish at COSL smoothed the waters for us.

The sponsor of this project was Rear Adm. R. Pittenger, Oceanographer of the Navy, and his technical director, R. Winokur (OP-096). R. Feden, M. Briscoe, and K. W. Lackie with the Office of Naval Research provided contract management and Navy liaison. Funding was administered by the Office of Naval Research.

The APL-UW effort was lead by Bruce Howe, James Mercer, Robert Odom, and Robert Spindel with support from Kate Bader, Brad Bell, Monty Bolstad, Don Reddaway, Gordon Glass, Burt Gropper, Ken Kientz, Kelley Knickerbocker, Carl Larson, Shaun Leach, Anne Marshall, Le Olson, Beau Paisley, Dave Ramstad, Kay Runciman-Moore, Chris Walter, Tim Wen, Eric Winkelman, and many others too numerous to mention.

ABSTRACT

The feasibility of an operational tomography capability has been demonstrated. Daily inversions of acoustic travel time data produced sound speed profiles that were successfully integrated into the standard Navy operational product for the NW Atlantic. Improved estimates of the sound speed (and thus temperature) reduced the error variance approximately 20% along the source-receiver vector. The resultant temperature fields, produced on a daily basis, have been reformulated as synthetic bathythermographs for input to the Optimal Thermal Interpolation System at the Fleet Numerical Oceanography Center. Sound speed fields based on tomographic results change predicted convergence zone ranges by about 10 km, with corresponding changes in the local acoustic intensity of 10 dB or greater. In addition, acoustic transmissions from Bermuda through the Gulf Stream were used to estimate the position of the Gulf Stream in real time. The precision (using air-dropped expendable bathythermograph (AXBT) data as ground truth) is better than 10 km under certain circumstances. This information can be used by the Operational Oceanography Center to improve estimates of Gulf Stream frontal location, which are presently based on IR satellite images. The transmissions from Bermuda northward are continuing. The deployment of six acoustic sources south of Bermuda in 1991 will improve the horizontal resolution. Recommendations are given for future work.

CONTENTS

| | | |
|----|--|-----|
| 1. | INTRODUCTION..... | 1 |
| 2. | EXPERIMENT..... | 5 |
| | 2.1 Instrumentation..... | 6 |
| | 2.2 Signal Processing | 13 |
| | 2.3 Data Processing | 19 |
| | 2.4 Data Analysis | 25 |
| | 2.5 Other Data | 34 |
| 3. | RESULTS | 50 |
| | 3.1 Comparisons with AXBT Data | 50 |
| | 3.2 Comparisons with OOC Fronts | 65 |
| | 3.3 Comparisons with OTIS Fields | 68 |
| | 3.4 Acoustic Comparisons | 80 |
| | 3.5 SURTASS Data | 80 |
| 4. | DISCUSSION | 101 |
| 5. | CONCLUSIONS AND RECOMMENDATIONS | 105 |
| 6. | REFERENCES | 110 |

LIST OF FIGURES

| | <i>Page</i> |
|--|-------------|
| Figure 1. Initial concept of the Applied Tomography Project | 2 |
| Figure 2. Data flow and analysis plan for ATE90..... | 4 |
| Figure 3. Source instrument package being deployed from OCP <i>Seacon</i> | 7 |
| Figure 4. A photograph of the bottom at the location of source 1 | 10 |
| Figure 5. A photograph of the bottom on Bowditch Seamount | 11 |
| Figure 6. The five equipment racks installed at the Navy facilities | 13 |
| Figure 7. A typical equipment rack installed at a Navy facility | 14 |
| Figure 8. The data-acquisition system..... | 15 |
| Figure 9. Signal processing flow chart | 16 |
| Figure 10. Typical relative arrival patterns measured at the various arrays..... | 18 |
| Figure 11. Data processing for path 1006 | 20 |
| Figure 12. Data processing for path 1015 | 22 |
| Figure 13. Data processing for path 1011 | 23 |
| Figure 14. Sound speed field and error field for day 199 (18 July 1990) along path 1006, calculated from the OTIS temperature and salinity sections..... | 24 |
| Figure 15. A section of the ray paths through the sound speed section in Figure 14 | 25 |
| Figure 16. Predicted arrival times and measured arrival pattern for path 1006 on day 199 | 26 |
| Figure 17. Predicted dot plot for path 1006 | 27 |
| Figure 18. Empirical orthogonal functions used in the analysis..... | 30 |
| Figure 19. Data analysis flow chart | 35 |
| Figure 20. OTIS sections along path 1006 on 18 July 1990 | 36 |
| Figure 21. Sound speed field derived from the temperature and salinity fields given in the previous figure, and rms sound speed error | 37 |

| | | |
|------------|--|----|
| Figure 22. | EOF amplitude error variances as a function of range along the 1006 path..... | 38 |
| Figure 23. | EOF amplitude error variances after being increased to account for time offsets | 39 |
| Figure 24. | Sound speed error section from OTIS and after increasing the errors.. | 40 |
| Figure 25. | Covariance matrix for EOF 1..... | 41 |
| Figure 26. | Sound speed and temperature EOF amplitudes and standard errors as a function of range along path 1006 after assimilating the travel time data | 42 |
| Figure 27. | Sound speed and temperature perturbations as a function of range and depth corresponding to the EOF amplitudes in Figure 26..... | 43 |
| Figure 28. | Total sound speed and temperature sections..... | 44 |
| Figure 29. | Estimated errors in the sound speed and temperature sections..... | 45 |
| Figure 30. | Depth-averaged sound speed and temperature perturbations, and depth-averaged rms sound speed and temperature error before and after assimilation of the tomography data..... | 46 |
| Figure 31. | Sea surface temperature in the experimental area, from AVHRR satellite data | 47 |
| Figure 32. | Dot plot of the acoustic arrival patterns measured on the towed array from USNS <i>Bold</i> | 49 |
| Figure 33. | Temperature sections from 18 July along slice 1006 | 51 |
| Figure 34. | Temperature sections from 22 July along slice 1006 | 53 |
| Figure 35. | Relative Gulf Stream position from day 198 to day 205 (17 July to 24 July) | 55 |
| Figure 36. | Tomography temperature field for 22 July..... | 59 |
| Figure 37. | Tomography temperature field for 22 July minus the tomography temperature field for 18 July..... | 59 |
| Figure 38. | Temperature sections along path 1006 for 11 September | 60 |
| Figure 39. | Temperature sections along path 1006 for 14 September | 61 |
| Figure 40. | Surface topography maps derived from OTIS of the experimental area for 7, 8, and 13 September..... | 62 |

| | | |
|------------|--|----|
| Figure 41. | Average and rms differences between OTIS and tomography results, OTIS and AXBT results, and tomography and AXBT results, for each water mass in two depth intervals. For 11 September..... | 63 |
| Figure 42. | Average and rms differences between OTIS and tomography results, OTIS and AXBT results, and tomography and AXBT results, for each water mass in two depth intervals. For 14 September..... | 64 |
| Figure 43. | Relative front locations of Gulf Stream north wall along path 1006.... | 66 |
| Figure 44. | Relative Gulf Stream north wall front location along path 1015 | 67 |
| Figure 45. | Temperature along slice 1006 (section 2) for 26 August (day 238)..... | 70 |
| Figure 46. | Daily rms difference between standard OTIS and tomography temperature as a function of depth for the different water masses | 71 |
| Figure 47. | Standard OTIS temperature on 4 September minus tomography temperature | 72 |
| Figure 48. | OTIS temperature section for 31 August and 10 September for slice 1006 | 73 |
| Figure 49. | Temperature section for 24 August along slice 1006: (a) OTIS, (b) tomography | 74 |
| Figure 50. | Temperature section for 7 September along slice 1006: (a) OTIS, (b) tomography | 75 |
| Figure 51. | Mean and rms difference between tomography results and OTIS results, front and eddy models, and GDEM predictions | 79 |
| Figure 52. | Percent reduction in temperature variance averaged along the slice as a function of time | 82 |
| Figure 53. | Transmission loss along path 1006 calculated using the sound speed field derived from OTIS | 83 |
| Figure 54. | Transmission loss along path 1006 calculated using the sound speed field incorporating tomography data..... | 85 |
| Figure 55. | Difference in transmission losses calculated from OTIS results and from tomography results as a function of range and depth for a source at 122 m..... | 87 |
| Figure 56. | Track of the SURTASS ship from year day 197 through 203 north of Bermuda..... | 89 |

| | | |
|------------|--|-----|
| Figure 57. | Typical reception during day 197 | 90 |
| Figure 58. | Plot of all arrivals..... | 91 |
| Figure 59. | Arrival peaks after subtracting travel time to the array using a sound speed of 1492 m/s | 96 |
| Figure 60. | Peaks after smoothing..... | 97 |
| Figure 61. | Comparison with the three ray trace simulations along FNOC slices | 98 |
| Figure 62. | Figure demonstrating complexity of the Gulf Stream meander system and how multiple front crossings of rays make estimating frontal location difficult..... | 99 |
| Figure 63. | In this figure OOC positions were used to calculate travel times for the later axial arrivals..... | 100 |
| Figure 64. | Map showing possible ray paths between the AMODE moorings and fixed receivers..... | 104 |
| Figure 65. | An idea for using applied tomography in the North Atlantic | 109 |

1. INTRODUCTION

For the Navy to perform its mission, it must have good descriptions of the environment in which it is operating. Knowing the sound speed field in the ocean is crucial. Our approach to ocean environmental prediction in general, and to the sound speed field in particular, has been to assimilate all possible forms of data into numerical models based on ocean physics to produce nowcasts and forecasts of fields of interest. This methodology is still in its infancy; it is still both model and data limited. This report addresses part of the data limitation issue.

Acoustic tomography has been under development for the past ten years as a measurement technique that can provide direct, synoptic, large-scale, *in situ*, quantitative estimates of the sound speed field. A partial description of this research can be found in the works of Munk and Wunsch [1979], the Ocean Tomography Group [1982], Cornuelle et al. [1985], Howe et al. [1987], and Worcester et al. [1990]. The focus of the Applied Tomography Project is to transition this research work into Navy operations. Figure 1 illustrates, in cartoon fashion, the concept of applied tomography. Because the effectiveness of tomography increases with the square of the number of instruments employed, all available sources and receivers should be utilized. These include fixed receivers, moored and cabled transceivers, drifting buoys with hydrophone arrays, and towed sources and receivers. In all cases, precise timekeeping and positioning are essential. The tomographic measurements do not stand alone; they must be combined with other, complementary measurements—such as XBT and altimetry data and satellite IR images—in a real-time “Ocean System.”

The Applied Tomography Experiment of 1990 (ATE90), conducted in the Northwest Atlantic, was a first step in adding a tomographic component to the Ocean System. The objectives of the experiment were to (1) integrate tomographic measurements into Navy environmental products in real time, and (2) demonstrate the value of the tomographic data.

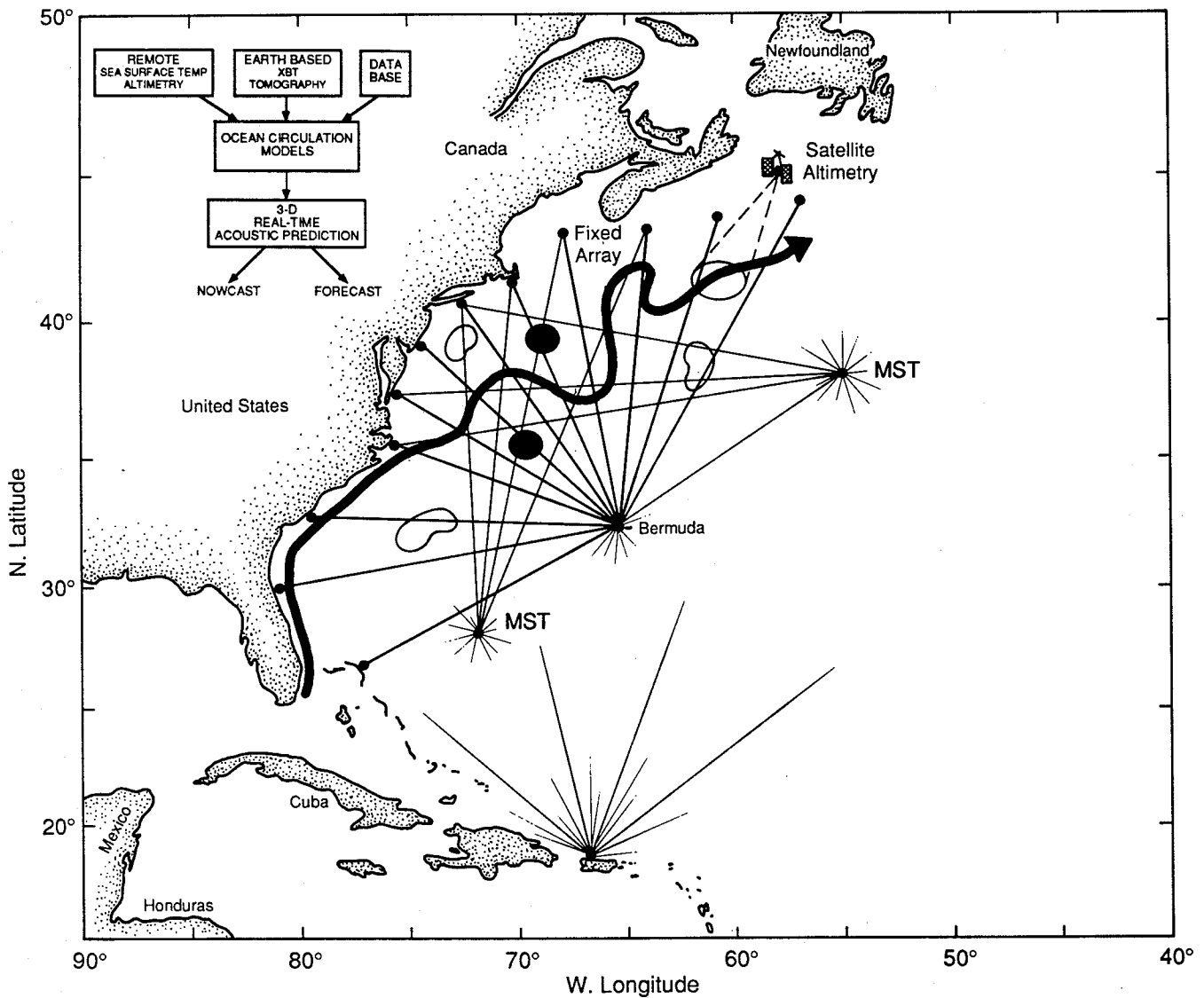


Figure 1. Initial concept of the Applied Tomography Project. All available assets are used to collect acoustic data, which are used with all other possible complementary data to provide ocean nowcasts and forecasts.

The Gulf Stream area was chosen for several reasons. First, the travel time “signal” is very large (about 1 s) compared with the precision of our measurements (about 1 ms) (Spiesberger et al., 1983). Second, it is the only geographical area for which the Fleet Numerical Oceanography Center (FNOC) routinely produces nowcasts. Third, this area is an excellent test bed for an ocean monitoring system because it has been so well studied and characterized. A major part of the project was devoted to establishing the human as well as the data communication links that are needed for the smooth operation of a complex system of this type. Figure 2 shows the framework in which the objectives of the project were met. APL used FNOC temperature fields as initial estimates for the inversion of travel-time data to produce synthetic bathythermographs (BTs). FNOC, running the Operational Thermal Interpolation System (OTIS), incorporated these synthetic temperature profiles. The Naval Oceanographic and Atmospheric Research Laboratory (NOARL) provided ground truth data in the form of six AXBT flights and performed additional analysis. The Operational Oceanography Center (OOC) provided daily ocean-feature maps of the northwest Atlantic.

In the next section we describe the experiment, including instrumentation, signal processing, data processing, and data analysis. Section 3 contains comparisons between the tomographic results and other, independent results. Section 4 is a discussion of the results, followed by conclusions and recommendations in Section 5.

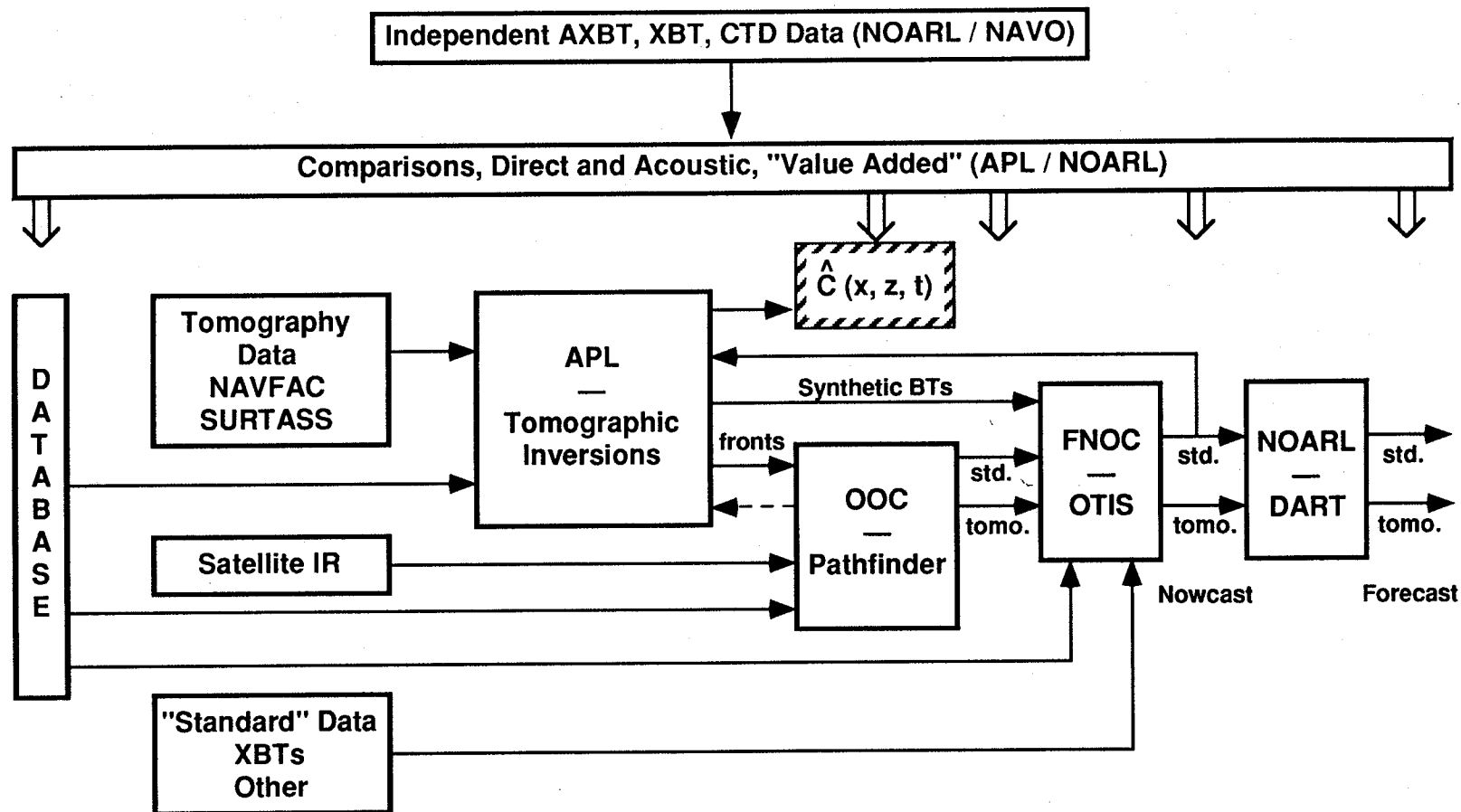


Figure 2. Data flow and analysis plan for ATE90.

2. EXPERIMENT

The experiment consisted of instrumenting acoustic arrays at Navy facilities in various locations, installing two acoustic sources off Bermuda, monitoring the transmissions to determine acoustic travel times, performing inversions to obtain estimates of the sound speed (temperature) structure, and integrating these results into a standard FNOC product.

Bermuda was chosen because it has steep slopes, permitting downward-going energy to enter the sound channel without being reflected from the bottom. The steepest acoustic rays of interest for long-range propagation are generally 13° , so any slope steeper than this will not interfere. There was concern about bottom interaction because of experience with the Kaneohe source in Hawaii (J. Spiesberger, personal communication). P. Haeger at NAVOCEANO was kind enough to make acoustic predictions which indicated that bottom interaction would not be a problem at Bermuda.

There were other reasons for wanting the sources on or near the bottom. If the source is on a single-point mooring, moving in response to currents, the measured travel times will be affected by distance changes resulting from this motion; by placing the source on the bottom, this problem is eliminated. Also, the clocks in the electronics controlling the sources drift over time: roughly 1 ms per day is typical. Nearby receivers available at Bermuda were used to measure this drift. Accurate accounting for this drift in real time would not have been possible if this short-range signal had been contaminated with mooring motion. Furthermore, we wanted to come close to the situation we would have if the sources were eventually cabled from shore for long-term (10 year) duty.

Planning began in January 1990; the official start was in March. By July, five racks of electronics had been built and installed.

2.1 Instrumentation

2.1.1 Sources

Two Hydroacoustics HLF-5 acoustic sources were deployed off Bermuda. The acoustic paths from each source to the receivers were virtually identical; two sources were used to provide redundancy. They were installed in protective cages, each containing an electronics package (Worcester et al., 1985), three battery cases, and compressed-air bottles for pressure compensation (Figure 3). The transmitted signal was a maximal length shift register sequence with the following parameters:

- center frequency (f_0), 250 Hz
- bandwidth, 83 Hz
- sound pressure level, 193 dB re 1 μ Pa at 1 m
- sequence length, 1023 digits
- digit length, three cycles of 250 Hz, 12 ms
- sequence repetitions, 8
- digital phase modulation angle, 88.20922°
- sequence laws, source 1 = 2033₈, source 2 = 3471₈
- sequence initialization, 1000₈.

Thus each sequence was 12.2760 s in length, and each transmission of eight sequences was 98.208 s long. On deployment, the sources were programmed to transmit every half hour for 12 hours and then switch to one transmission every 4 hours. During two weeks, 16–22 July and 10–16 September, the sources were programmed to transmit once every 40 minutes (36 transmissions per day) while AXBT surveys were conducted and USNS *Bold* was operated north of the Gulf Stream (16–22 July only).

Before the sources were installed, one was suspended from the deployment vessel, the OCP *Seacon*, in deep water (4000 m) about 20 km northwest of Bermuda to provide a test signal free of any bottom interaction effects. There was no significant difference between the signals received from this deep-water location and those eventually received from the locations near or on the bottom.

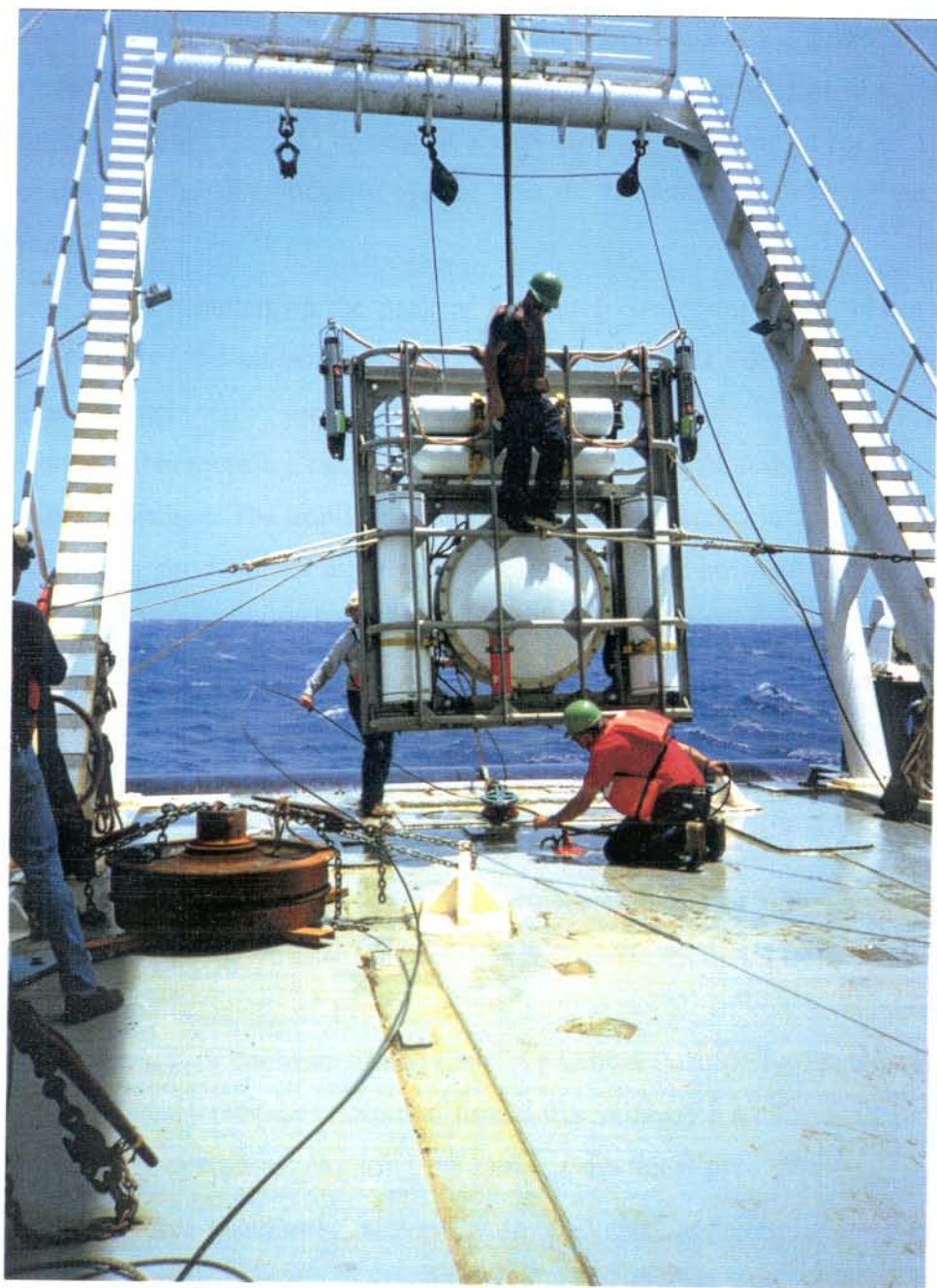


Figure 3. Source instrument package being deployed from OCP Seacon. The HLF-5 acoustic source is in the center surrounded by an electronics case, battery cases, compressed air bottles for pressure compensation, and acoustic releases. The releases are mounted on the side to minimize the distance from the source to the bottom. The instrument package was buoyed up with a syntactic foam float (not shown).



Source 1 was installed on the northwest slope of Bermuda at a depth of 969 m, 2 m off the bottom. Figure 4 is a photograph of the bottom at the installation site, showing a smooth surface that appeared to consist of a thin layer of sediment on rock. The slope was approximately 16° , significantly greater than the launch angle (13°) of the steepest ray of interest.

Source 2 was installed on the peak of Bowditch Seamount about 40 km north of Bermuda. The top of the seamount is very rugged, with ravines 100 to 200 m deep. Figure 5 is a photograph of the site, showing a sharp void off to the right. The source was deployed on a 100 m mooring, but ended up at a depth of 975 m, only 25 m off the nominal top of the seamount. The implication is that the anchor settled in a ravine. Although this seamount is a good site for a permanent source from the point of view of providing good acoustic paths to the receivers, the problems with laying a cable over such rough terrain are not insignificant.

Source 2 failed on 18 July after 150 transmissions. The cause of the failure was a leak in a pressure relief valve. Since the data from source 2 were virtually identical to those from source 1, in this report we examine only data from source 1.

Accurate relative positioning was necessary for bathymetry surveys in connection with accurate source deployments. A Mini-Ranger system set up on Bermuda provided a relative positioning accuracy of 1 m at the NW site; at the Bowditch Seamount site, the Mini-Ranger signal was intermittent and the Navy Global Positioning System (GPS) was used. It would be very useful to have real-time differential GPS and/or dedicated P-code receivers for future operations requiring the same navigational precision.

Following source installation, surveys were conducted to determine absolute source location. A GPS station at the Bermuda Naval Facility was used as a reference for differential GPS ship navigation. Estimates of the locations in WGS84 coordinates are

| | |
|---------------|--|
| GPS reference | $32^\circ 15.8536' \text{N}, -64^\circ 52.6740' \text{W}$ |
| Source 1 (10) | $32^\circ 31.1585' \text{N}, -64^\circ 52.8573' \text{W}$, 969 m depth |
| Source 2 (11) | $32^\circ 44.6085' \text{N}, -64^\circ 33.8703' \text{W}$, 975 m depth. |



Figure 4. A photograph of the bottom at the location of source 1. The camera is about 6 m above the bottom; there is a scuba bottle on the trigger line. The bottom is quite smooth, with a few centimeters of loose sediment.



Figure 5. A photograph of the bottom on Bowditch Seamount. Note the "black hole" in the upper right where the bottom falls off rapidly.

The estimated horizontal error in the source positions is approximately 10 m. For data-analysis purposes, sources 1 and 2 were given the designations 10 and 11, respectively. These designations are indicated in parentheses.

2.1.2 Receivers

The Applied Tomography receivers are based on 386-AT computers. These computers are appropriate for this specific experiment, and they are adequate to handle receptions from a larger number of fixed or moored sources, thereby providing future capacity. Indeed, they will be used for the six sources to be deployed south of Bermuda in 1991–1992 as part of the Acoustic Mid-Ocean Dynamics Experiment, AMODE. If moving sources are used, the receiver hardware can be easily upgraded to 486 systems to handle the increased computational burden of correcting for Doppler shifts and more frequent transmissions.

At each station, a computer dedicated to each specific array (slaves) and one control/communications computer (the master) were installed (see Figures 6 and 7). The slave computers perform digital-beamforming operations, replica-correlation signal processing, and storage of multipath signal peak data. The slaves are connected via a local area network which in turn is connected to a communications computer at APL via STU-III secure telephones/modems. The computer at APL can read the disks of the remote computers and can display the screens for each. This permits real-time remote programming of the computers at the stations, which has proven extremely useful in correcting various system bugs.

The receiving hardware used on USNS *Bold* was intended as a developmental system and was almost identical to the equipment at the land stations, lacking only a real-time data link.

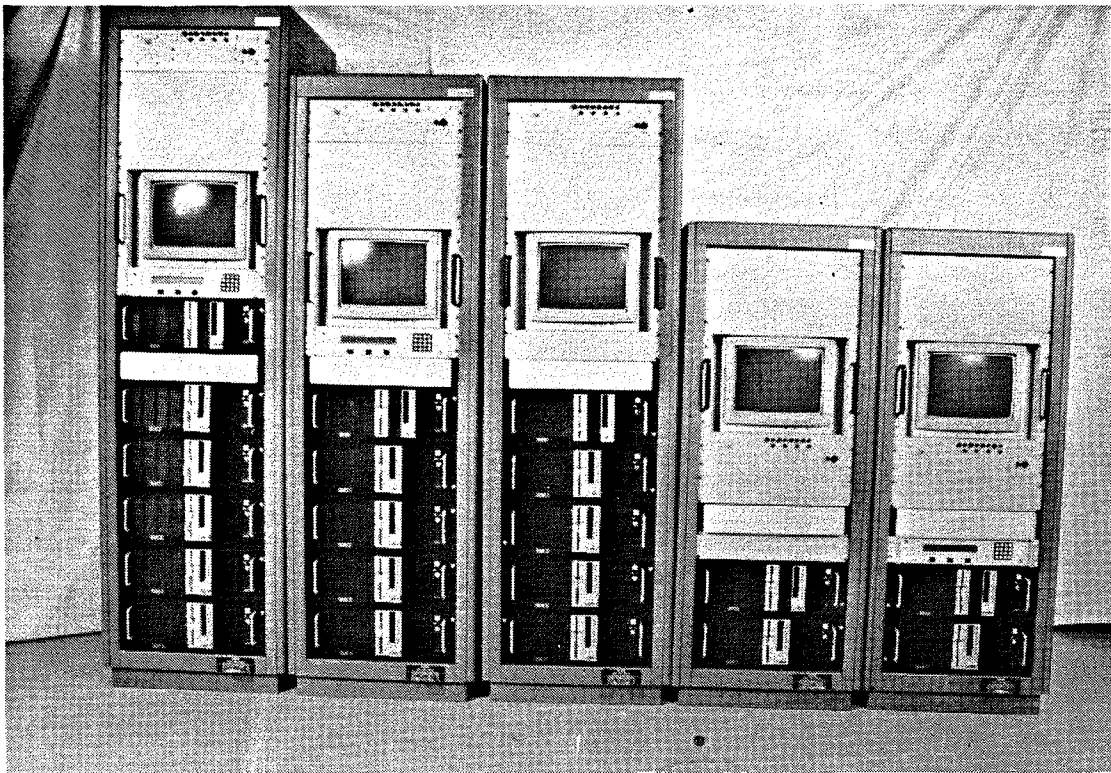


Figure 6. The five equipment racks installed at the Navy facilities.

Figure 8 shows the data-acquisition system. Accurate timing is provided by Kinemetrics GPS receivers that have disciplined rubidium frequency standards. Three channels of the analog-to-digital (a/d) system are devoted to timing signals.

2.2 Signal Processing

A signal-processing flow chart is shown in Figure 9. Figure 9a shows a high-level overview of the processing software structure. Figure 9b is a block diagram of the more important individual steps. The digitizing rate is 2 kHz, eight times the 250 Hz carrier frequency. If the source or receiver is moving (as in the case of the deep-water test with a ship-suspended source and the Surveillance Towed Array Sonar Segment (SURTASS) receptions), the output from a single hydrophone is used to determine the Doppler shift.

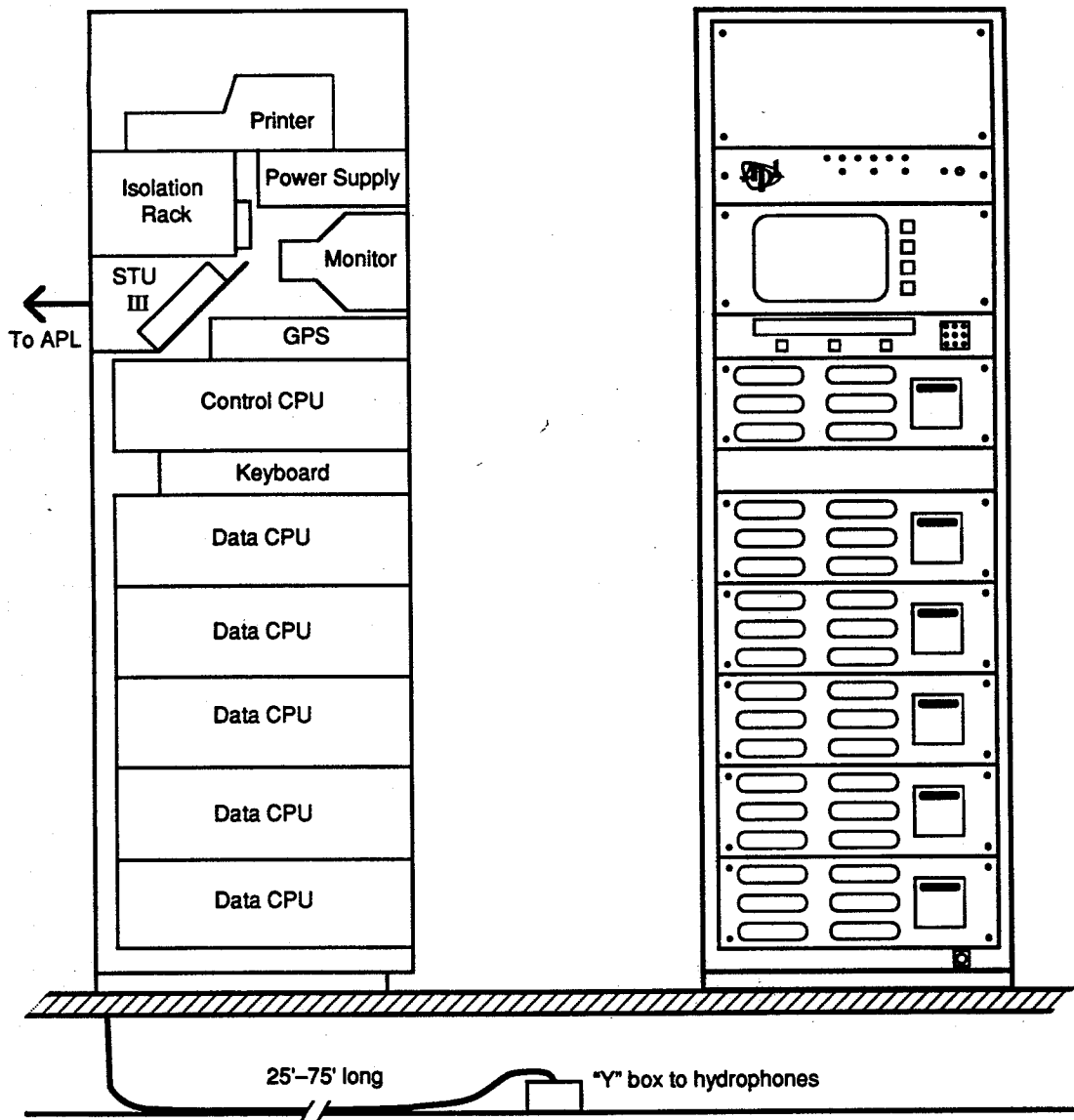


Figure 7. A typical equipment rack installed at a Navy facility. The power supply at the top drives the signal-conditioning electronics. The CRT monitor below it is usually connected to the master (control/communication) computer (the top computer). Below the master are the slave (data) computers which actually acquire and process the data from the hydrophone arrays. The Kinemetrics GPS time standard with disciplined rubidium standard is just below the CRT. The master and slave computers are linked together via a local area network, which, in turn, is linked to an APL computer via STU-III secure telephones/modems.

ATE90 FIELD SYSTEM CONFIGURATION

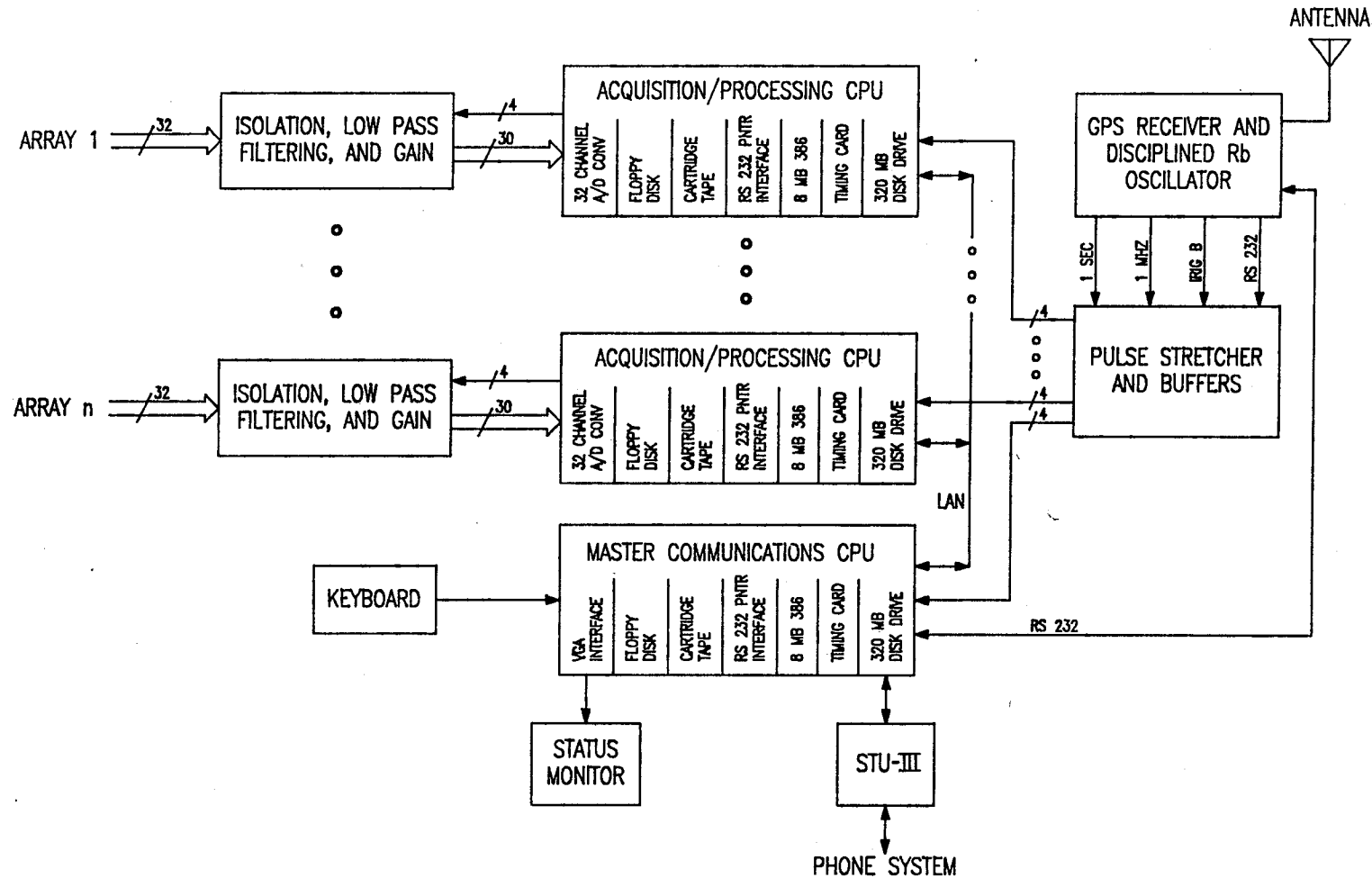


Figure 8. The data-acquisition system, including the signal-conditioning system, the analog-to-digital conversion system, the timing system, and the signal-processing computer.

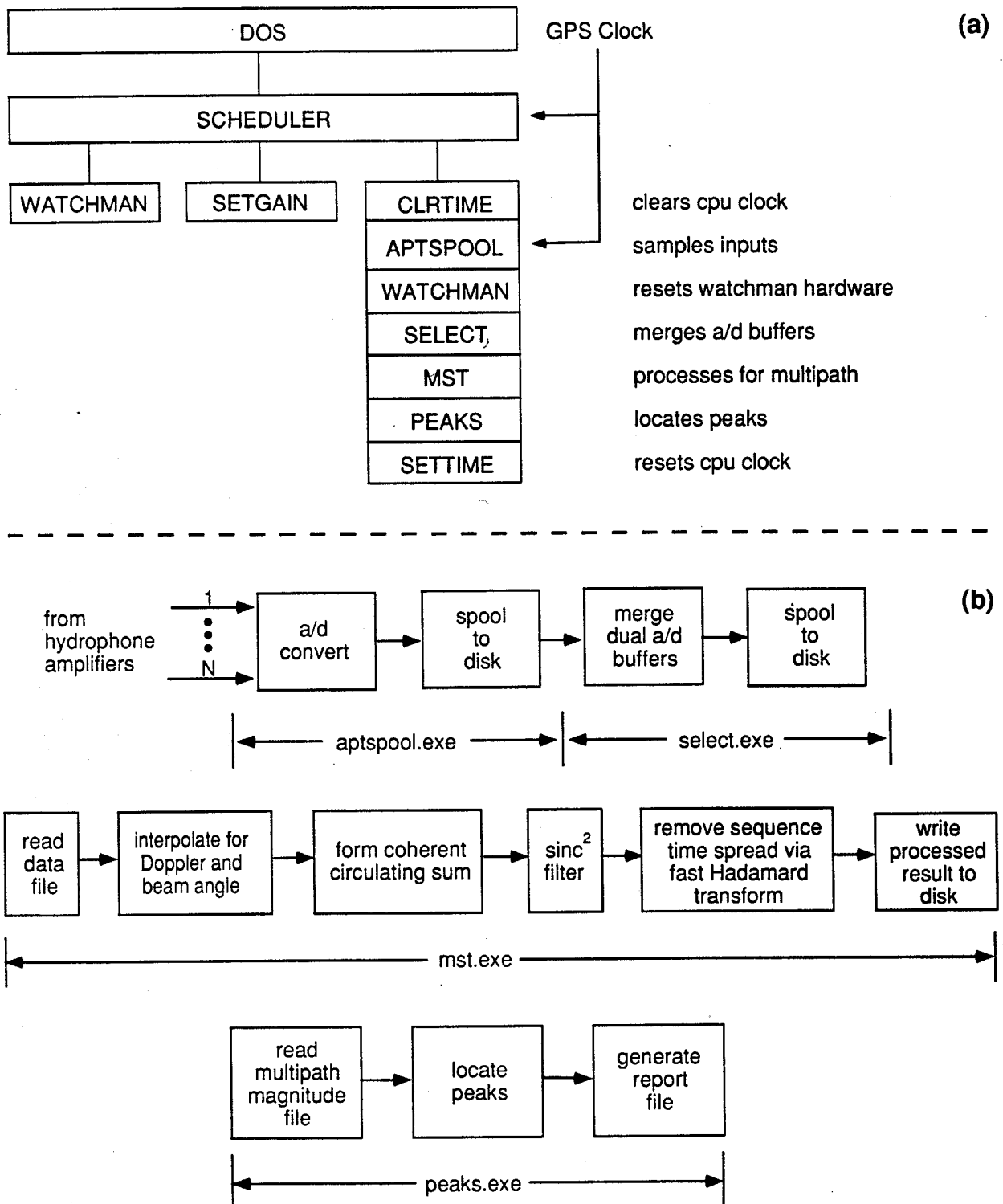


Figure 9. Signal processing flow chart. (a) high level overview; (b) details of the most important signal-processing elements.

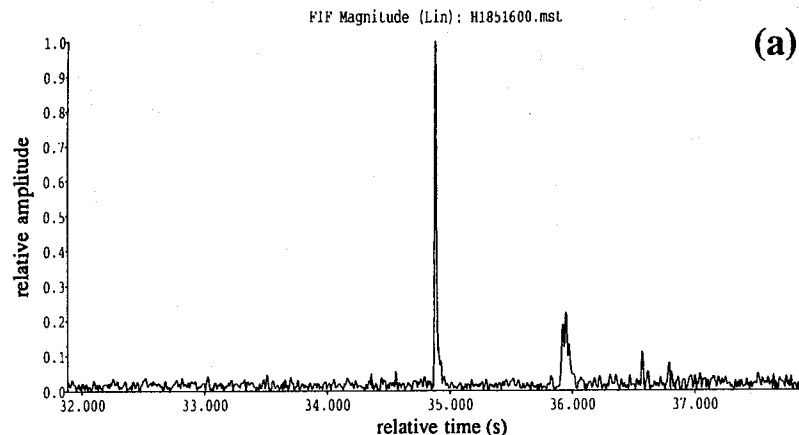
These data are processed over a range of trial Doppler shifts until the output of the replica cross-correlator is maximized. This determines the Doppler shift which is applied to all other hydrophone outputs. Hydrophone samples are linearly interpolated to correct for this Doppler shift. The corrected signal is complex demodulated (using a demodulation frequency of $f_0 + f_{\text{Doppler}}$) and then circularly averaged over seven of the eight sequences sent. These steps are performed for each hydrophone signal, and a cumulative sum is formed. A low-pass filter is then applied; it consists of a sliding-block average over three cycles of the carrier, which is equivalent to one digit, or 12 ms. The frequency response of this process is a sinc function. The data are passed through twice to get a sinc^2 response (this has a null at $-2f_0$). At this point, the sequence is removed by means of replica cross correlation, using the Hadamard transform. The complex correlates are converted to amplitude and phase. Peak arrival times, signal-to-noise ratios, and azimuthal arrival angles are found and saved. This file is then remotely retrieved by APL for subsequent analysis.

We have adopted a four-digit path labeling scheme: the first two digits designate the source, and the second two digits designate the receiver. The following table gives the code for each instrument and its rough location.

| | | |
|-------------|---|-------------------------------------|
| source 10 | = | source 1 on the NW slope of Bermuda |
| source 11 | = | source 2 on Bowditch Seamount |
| receiver 01 | = | far to the northeast |
| receiver 06 | = | far to the north |
| receiver 08 | = | to the west |
| receiver 11 | = | far to the west |
| receiver 15 | = | to the north. |

Thus, path 1006 is the path from source 10 to receiver 06.

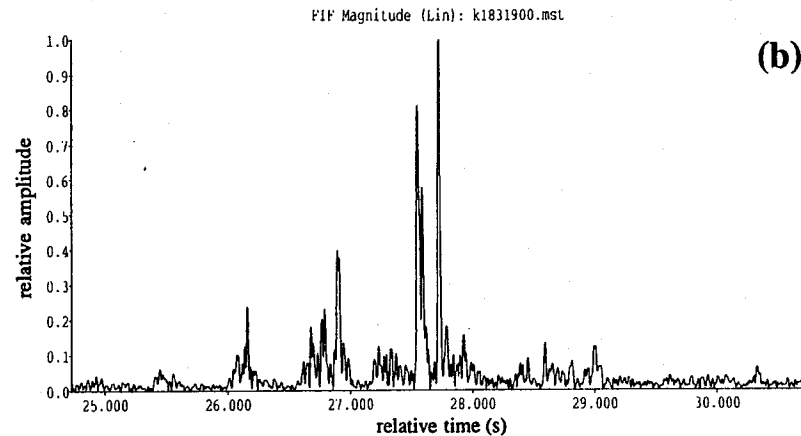
Typical arrival patterns at the various receivers from source 10 are shown in Figures 10a–10d. The signal-to-noise ratio (SNR) on receiver 08 was very strong



yr day 185:16:00:30
Wed Jul 04 16:00:02 1990
source: 10 receiver: 8

law:2033
angle:88.209000
periods:5
cyc/dig:3
sam/cyc:4

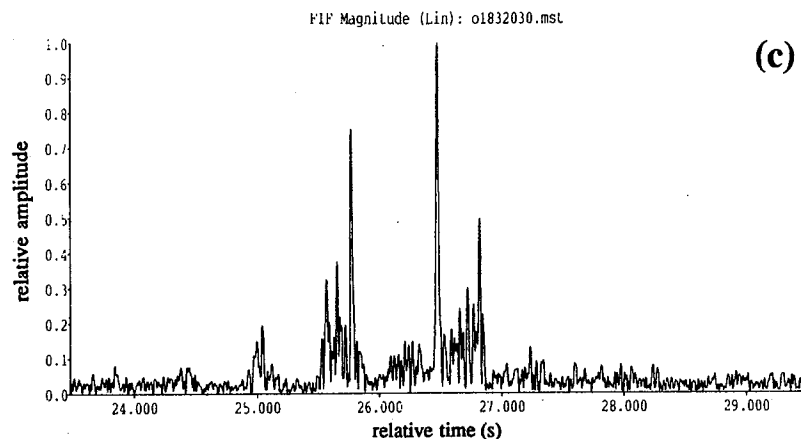
plot span: 6.0000 sec
beam angle: 44.1 degrees
doppler: 0.000 knots
max snr: 35.7 dB
r max:983192
at loc:11020
median:16221
plot max:983192
skipped scans:12276



yr day 183:19:00:30
Mon Jul 02 19:00:02 1990
source: 10 receiver: 11

law:2033
angle:88.209030
periods:5
cyc/dig:3
sam/cyc:4

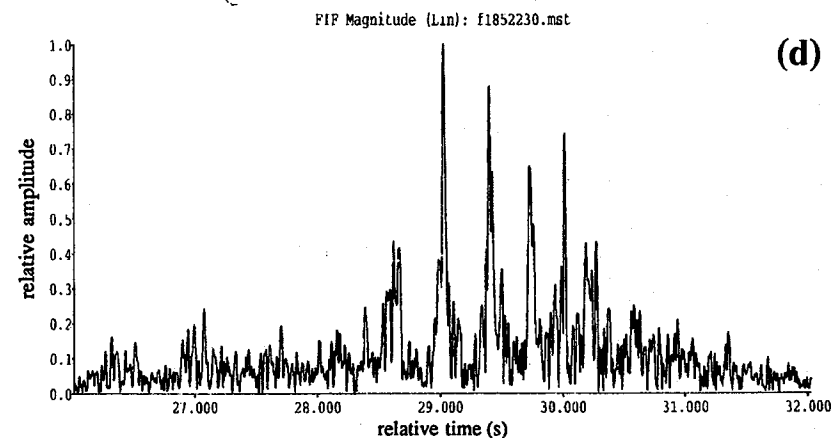
plot span: 6.0000 sec
beam angle:108.2 degrees
doppler: 0.450 knots
max snr: 36.6 dB
r max:620959
at loc:1865
median:9236
plot max:620959
skipped scans:12276



yr day 183:20:30:30
Mon Jul 02 20:30:02 1990
source: 10 receiver: 15

law:2033
angle:88.209030
periods:5
cyc/dig:3
sam/cyc:4

plot span: 6.0000 sec
beam angle:268.0 degrees
doppler: 0.200 knots
max snr: 32.0 dB
r max:232542
at loc:2615
median:5841
plot max:232542
skipped scans:12276



yr day 185:22:30:30
Wed Jul 04 22:30:02 1990
source: 10 receiver: 6

law:2033
angle:88.209000
periods:5
cyc/dig:3
sam/cyc:4

plot span: 6.0000 sec
beam angle:124.5 degrees
doppler: 0.000 knots
max snr: 26.3 dB
r max:184054
at loc:5163
median:8958
plot max:184054
skipped scans:12276

Figure 10. Typical relative arrival patterns measured at the various arrays. (a) reception at 08, nearby; (b) reception at 11, to the west; (c) reception at 15, to the north; (d) reception at 06, far to the north.

(Figure 10a), and was used to monitor clock drift in the source. (It is assumed that over short source/receiver paths the ocean does not change enough to contaminate clock measurements with time alternations due to propagation changes.) The SNR at the other receivers varied from 20–25 dB for the most distant receiver to 25–30 dB for the medium-range receivers, roughly in agreement with predicted levels. Only a few peaks are present in the 1011 and 1015 arrival patterns because they are deep receivers. The 1006 path has more arrivals because the receiver is closer to the sound channel axis. The amplitude of the arrivals via individual rays varied significantly from transmission to transmission, about 6 dB.

No coherent signal has been obtained on the receiver far to the northeast, path 1001. Arriving energy is incoherent across the array. Thus we get no coherent array gain, and the SNR is therefore too low to reveal persistent peaks. This lack of coherence is thus far unexplained and is a topic of investigation.

2.3 Data Processing

One needs to go from peaks in individual-arrival patterns to time series of ray arrivals. Figure 11a shows the raw peak data for the 1006 path from day 188 through day 273 (9 July through 30 September). There is a distinct pattern; weak early arrivals (corresponding to shallow and deep turning rays), then about six strong clusters, and then additional clusters that merge together. The six strong clusters can be identified with arrivals predicted by tracing rays through ocean sound speed fields derived from FNOC temperature fields. These fields are updated on a daily basis by FNOC to reflect changing environmental conditions. The six ray clusters are tracked using an algorithm that combines pattern recognition and cross-correlation techniques, Figure 11b. The tracked paths are processed to remove outliers and to determine and remove tidal signals and are then filtered; the final filtered paths are shown in Figure 11c. The travel times corresponding to each of these filtered paths are used in the inverse procedures described below. As a last step, these six paths are averaged to obtain one mean travel time for a simplified analysis, Figure 11d. The changes in travel time range from 0.1 s from day to day to 1 s

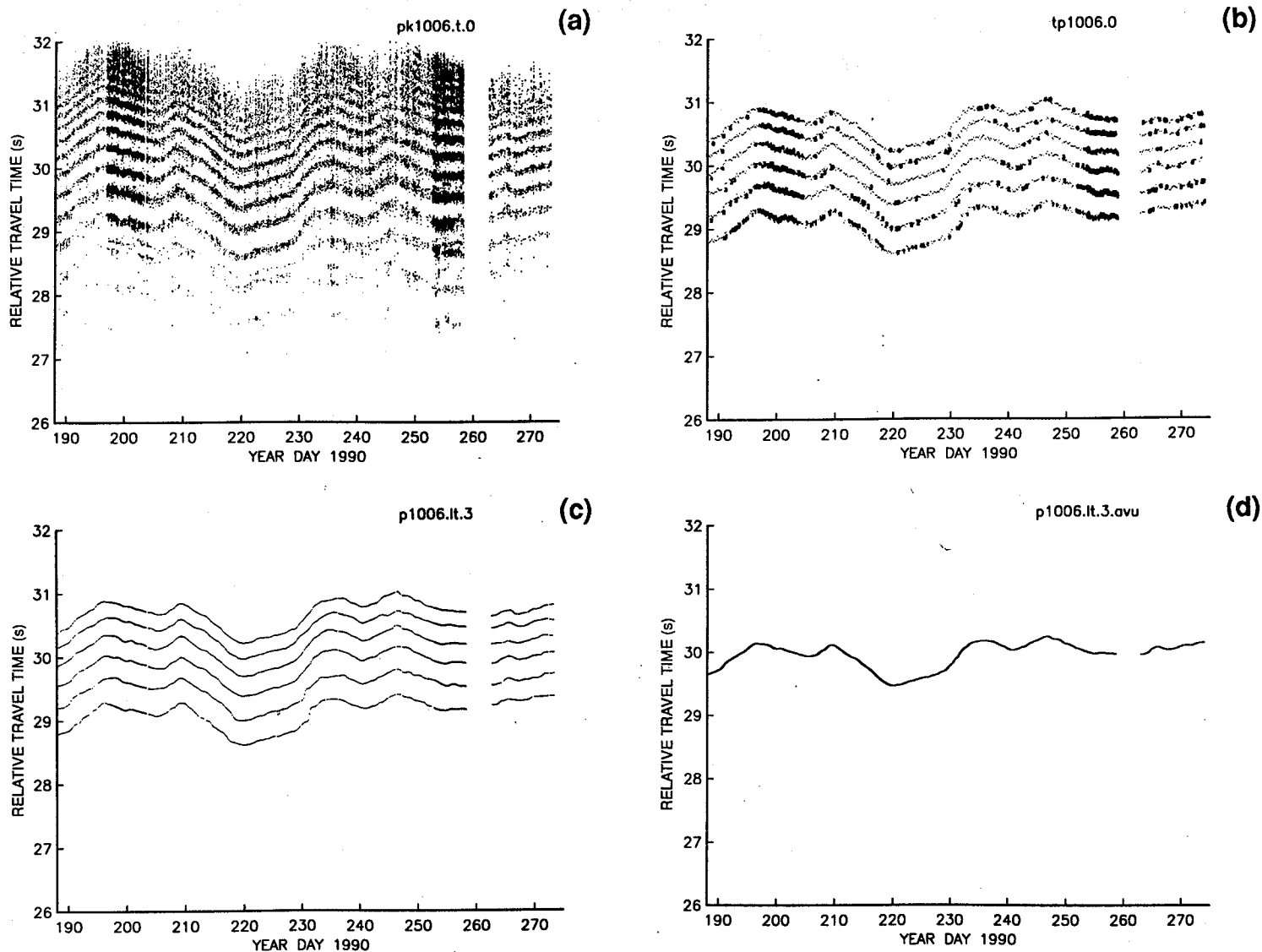


Figure 11. Data processing for path 1006. (a) The "dot plot" for the entire experiment. There were normally six transmissions per day; during the two intensive transmission periods, there were 36 per day. Each "dot" is a line whose length is proportional to the signal-to-noise ratio. (b) The tracked paths. When the tracking algorithm finds a peak, a "dot" is plotted; if no peak is found, the path number is plotted. (c) The result of filtering the tracked paths (after outliers and tides have been removed). (d) The average of the six paths. All times are relative.

over the course of the experiment. These changes are directly attributable to changes in Gulf Stream location and/or the presence of warm- or cold-core rings. The detailed structure within each group is being analyzed.

Similar plots for paths 1015 and 1011 are shown in Figures 12 and 13. Path 1015 also goes through the Gulf Stream, and large changes are evident in the mean travel time. Path 1011 is oriented east-west and lies entirely within the Sargasso Sea. The variation in the mean travel time is much less, about 0.1 s or less. It is interesting that there is a definite tidal signal in the 1011 data not evident in the scale of this figure. The amplitude of the travel-time variation is about 5 ms, which is equivalent to a tidal velocity of 10 mm/s. If the phase is locked to astronomical forcing, this variation most likely implies a barotropic tide; if not, it implies a baroclinic tidal perturbation of the sound speed.

The tracked and filtered paths need to be identified with predicted ray arrivals. The sound speed field is obtained from temperature and salinity data provided by FNOG along the same paths. The field for path 1006 on day 199 (18 July 1990) is shown in Figure 14, and the ray paths are shown in Figure 15. The presence of the Gulf Stream is evident. The predicted arrival pattern and the measured travel times for the same day are shown in Figure 16. The agreement is good, but unfortunately each tracked path does not correspond to a single ray but rather to a cluster of several rays. This was not predicted by (obviously oversimplified) simulations nor by the interpretation of previous data (Spiesberger et al., 1983). The problem is possibly exacerbated by the presence of higher-than-expected internal-wave noise and/or small-scale (<10 km) structure in the sound speed field. For these ranges, we expect an rms variation of approximately 10 ms in the travel times because of internal waves. In the inversion process, we assign the travel time measured for each ray cluster to all the rays associated with the cluster, with an error related to the width of the cluster; the rms error varied from 40 ms for the earlier arrivals to 30 ms for the later arrivals. This is considerably more than the expected error of about 5 ms for the daily-averaged travel time for a single ray.

Inspection of the travel time data-data covariance matrix, weighted by the data error, reveals that there is essentially only one independent datum; i.e., the travel times of

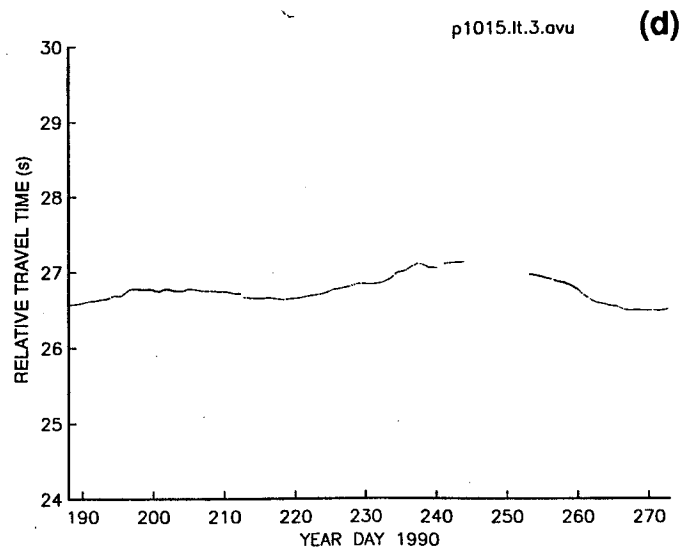
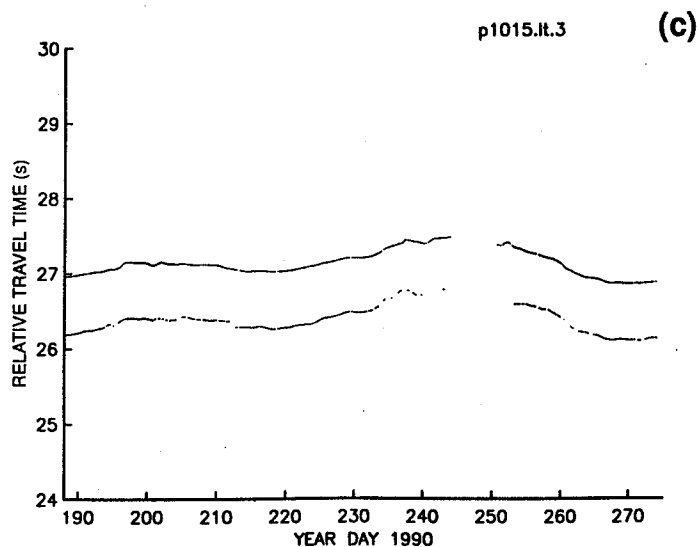
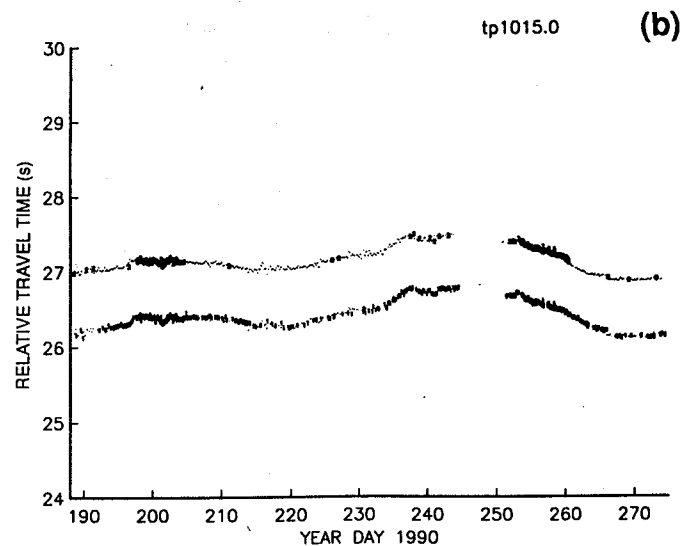
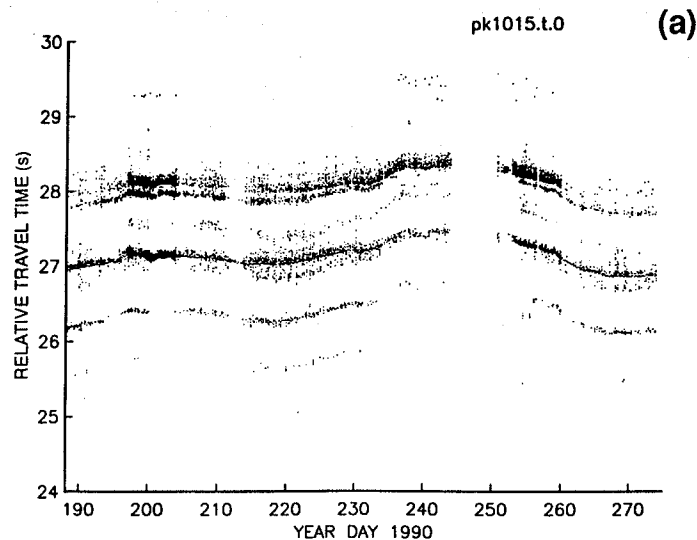


Figure 12. Data processing for path 1015. (a)–(d) are the same as in Figure 11. All times are relative.

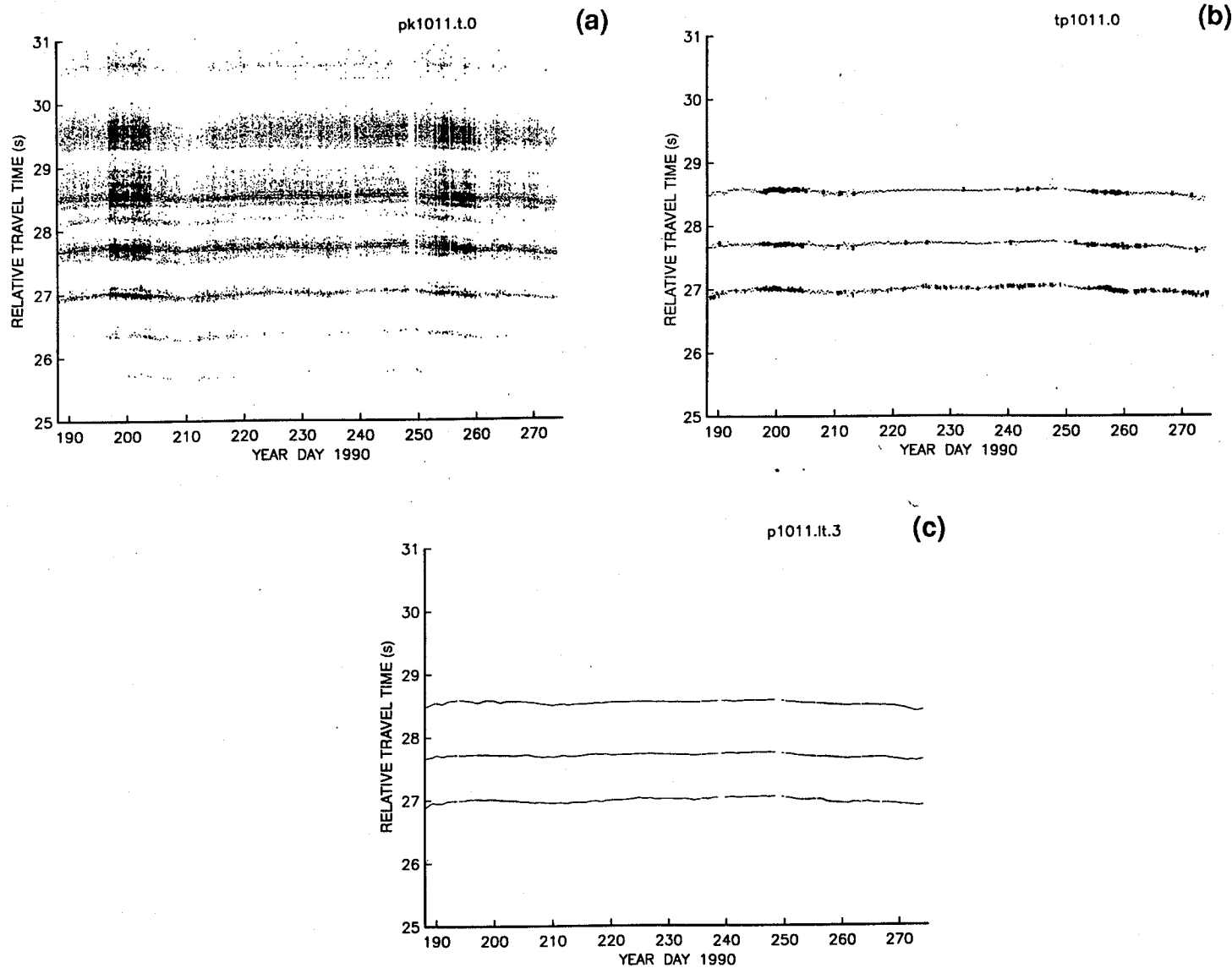


Figure 13. Data processing for path 1011. (a)–(c) are the same as in Figure 11. All times are relative.

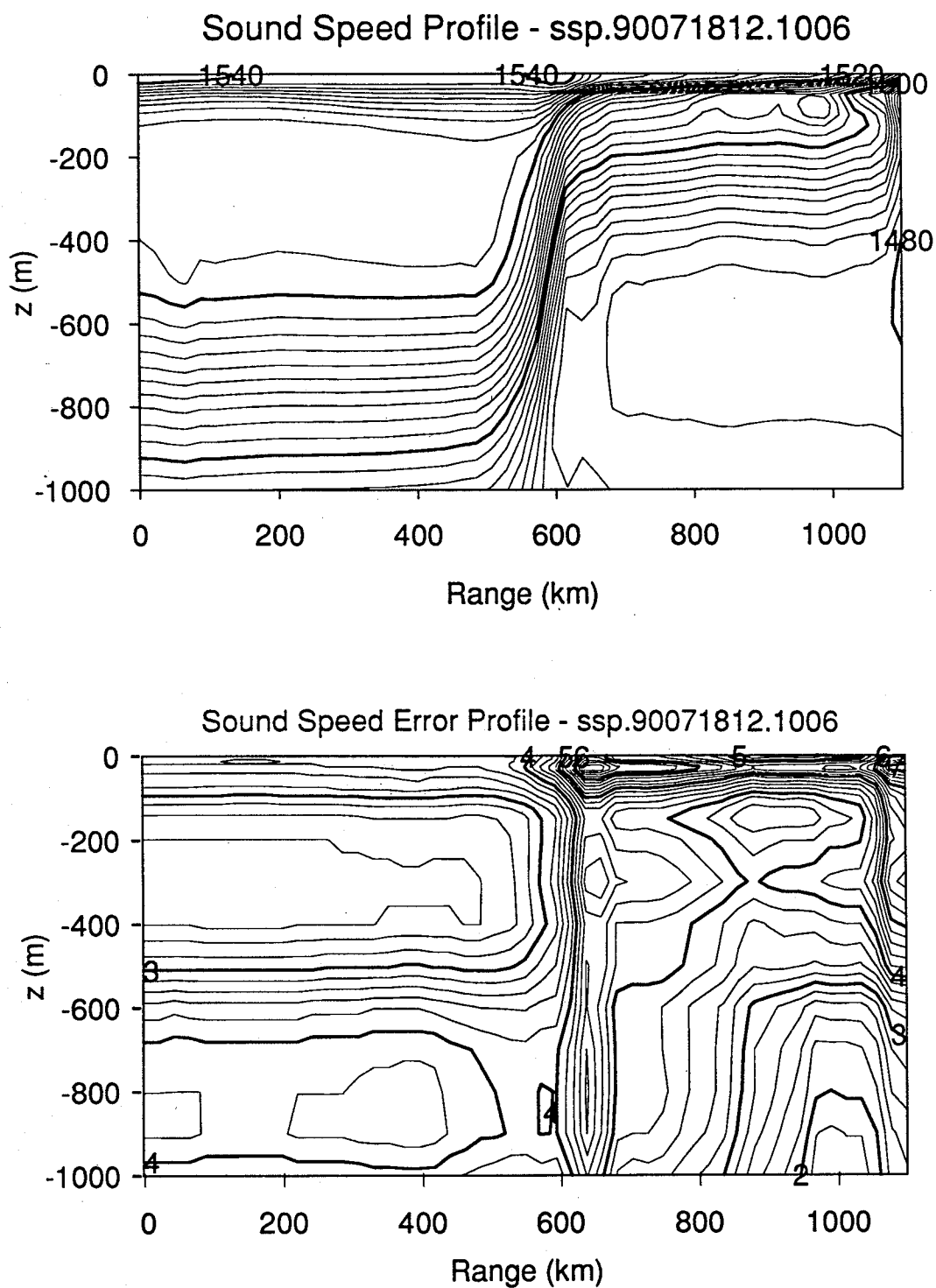


Figure 14. Sound speed field (top) and error field (bottom) for day 199 (18 July 1990) along path 1006, calculated from the OTIS temperature and salinity sections.

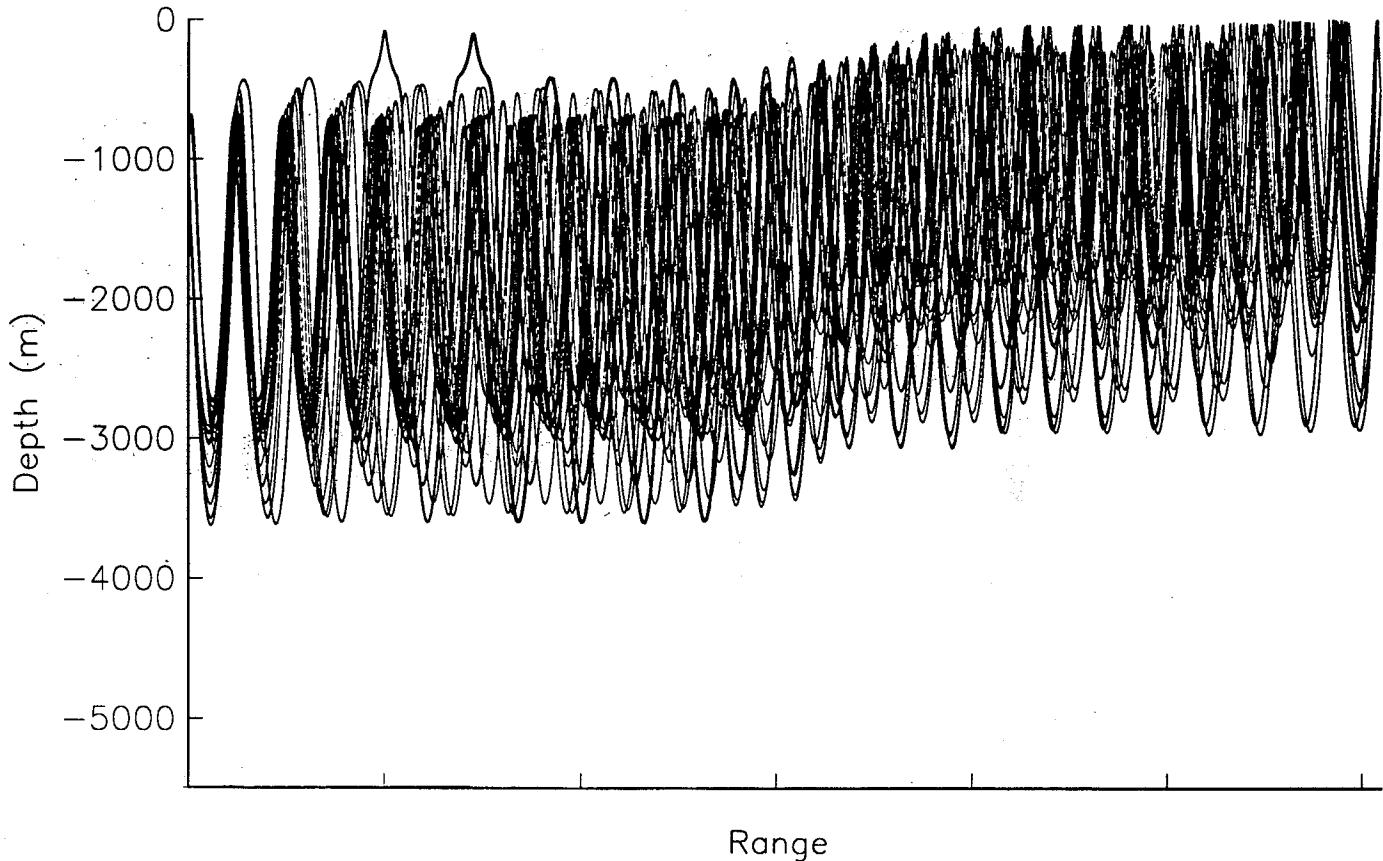


Figure 15. A section of the ray paths through the sound speed section in Figure 14.

all six paths are highly correlated (as is obvious in Figure 11a). Although all six paths have been used in the subsequent inversion procedure, one should keep in mind that they are not independent.

In Figure 17, the predicted ray arrivals are compared with the measured ray arrivals. The same pattern exists in the predictions as in the measurements, although the predicted pattern is not so smooth with time. This figure is the most direct comparison between the measured data and predictions based on operational Navy products.

2.4 Data Analysis

There are various levels of sophistication one can apply to analyzing these data. One can simply correlate a single mean travel time with the Gulf Stream front position

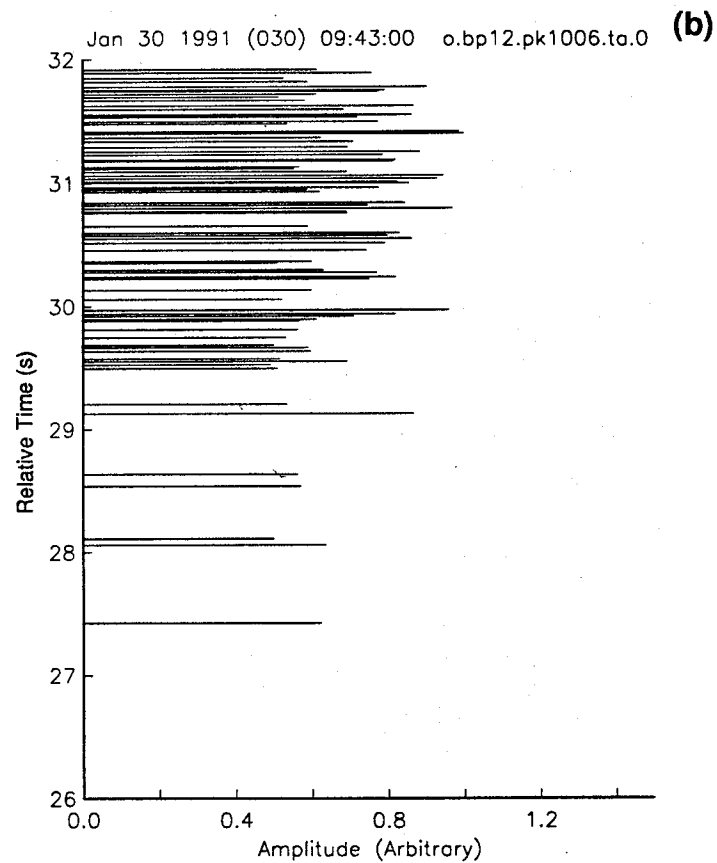
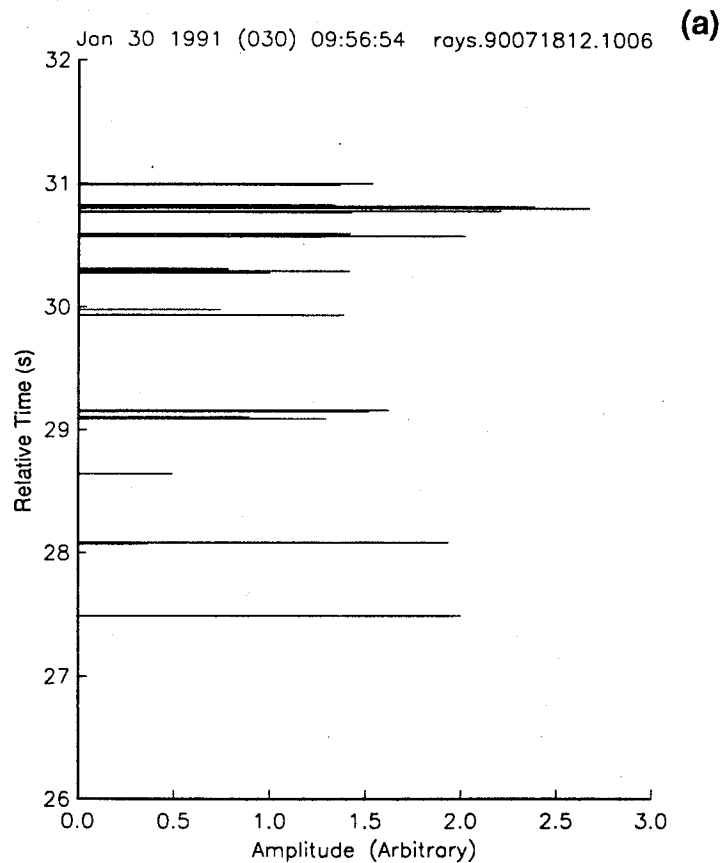


Figure 16. (a) predicted arrival times and (b) measured arrival pattern for path 1006 on day 199. All times are relative.

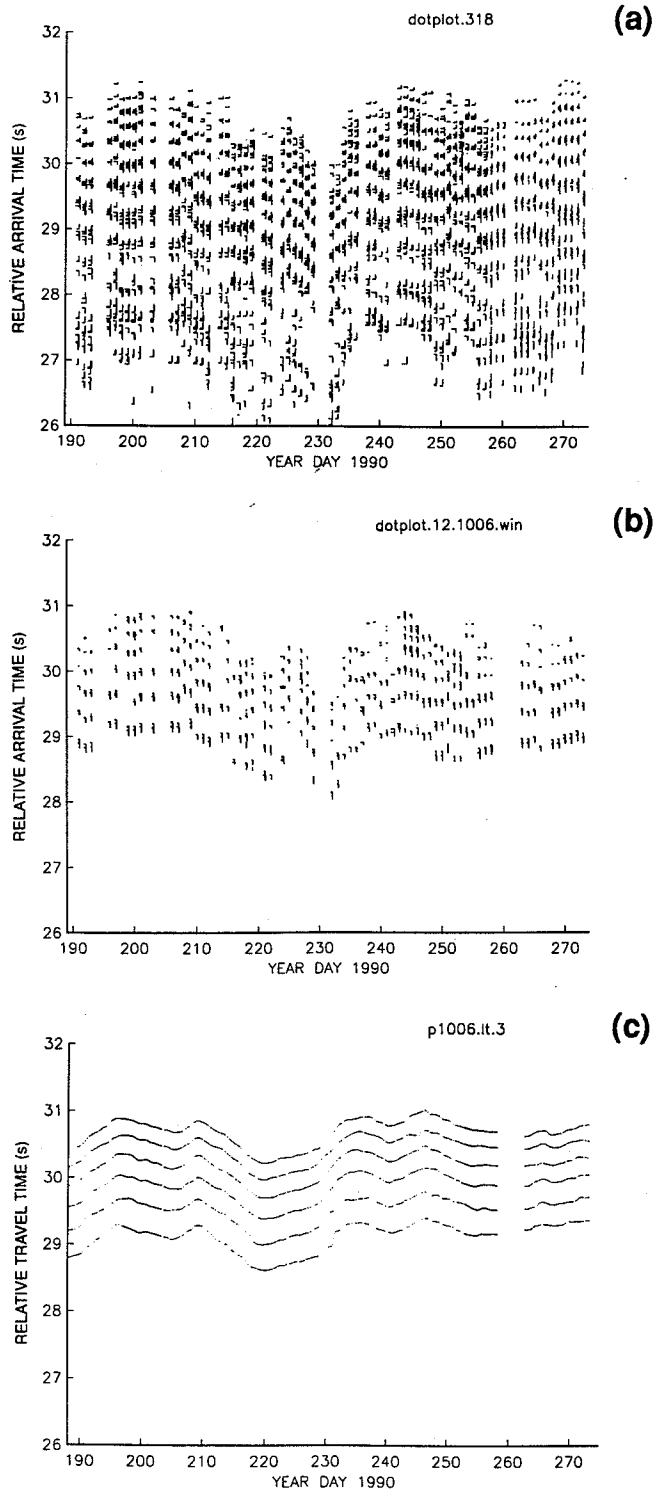


Figure 17. Predicted dot plot for path 1006. (a) All rays. The short vertical lines are proportional to the predicted arrival angle at the receiver. (b) Only the predicted rays in the measurement window. (c) The filtered tracked paths (same as Figure 11d). All times are relative.

(as is done with an inverted echosounder) or construct a simple inverse procedure to solve for multiple front positions when there are multiple fronts along the path. These simpler approaches will be discussed in the next section. Here we discuss the use of the more general geophysical inverse and how we have applied it to this problem.

2.4.1 General Ideas

In geophysical problems it is not possible to fully specify fields, such as ocean sound speed, that are continuous functions of position and time. Exact representation of a continuous function requires an infinite set of numbers with no errors. We are, however, limited to a finite set of numbers, with errors, which provides an approximate representation of the field. The set could be the actual values at a finite number of grid points, or it could be the coefficients of a finite number of functions. We choose to represent a vertical section of the sound speed field $C(x, z)$ as the sum of a reference section C_0 (derived from OTIS temperature and salinity) and a perturbation sound speed δC .

$$C(x, z) = C_0(x, z) + \delta C(x, z),$$

where x is the horizontal distance and z is the depth. This allows us to linearize an inherently nonlinear problem. Then we represent the perturbation as a sum of sines and cosines in the horizontal multiplied by empirical orthogonal functions (EOFs) in the vertical,

$$\delta C(x, z) = \sum_{ij} \left[a_i \cos \frac{2\pi i x}{L} + b_i \sin \frac{2\pi i x}{L} \right] Z_j(z),$$

where the Z functions are the EOFs (Figure 18). Time dependence is implicit, and L is several correlation length scales greater than the actual source/receiver range. The goal is to use the acoustic travel times (and eventually any other available data) to determine the coefficients a_i and b_i or some other “model parameters” and the unknown $Z_j(z)$. The OTIS output supplied by FNOC is used as the reference field C_0 . We note that representing the ocean in Fourier space is somewhat arbitrary; one could just as well use functions in physical space, such as boxes or pixels, to represent the ocean.

In geophysical situations, there is always a paucity of data; in fact, there are never enough data to determine a field uniquely. One must always use not only the information in the data, but *a priori* information that one has acquired from other sources, typically historical databases or some knowledge of the physics. For instance, we are quite sure that the ocean temperature at some point has an average value and some limits that will not be exceeded. We quantify this knowledge by assigning a mean and an rms value. A further step can be taken by saying that the temperature perturbations are Gaussian distributed; i.e., the probability of the temperature taking on a certain value has a Gaussian distribution. Furthermore, the temperature at one point is highly correlated with the temperature at a neighboring point and less correlated with a point farther away. This knowledge is quantified in the spatial covariance function.

The geophysical inverse is based on the foregoing assumptions, namely that the model perturbations are Gaussian distributed and that the spatial structure can be described by a covariance function. One last assumption is that the data measurement errors are also Gaussian distributed. These assumptions are a direct consequence of the linearization and lead directly to a linear least-squares solution for the model parameters. One determines the operator that converts the measurements to model parameters while minimizing the difference between the true model parameters and the estimated ones.

Thus, for a linear inverse problem the data are related to the model parameter vector \mathbf{m} (which contains the a 's and b 's) by

$$\mathbf{d} = \mathbf{G}\mathbf{m} + \mathbf{n},$$

where \mathbf{G} is the forward problem matrix that converts the model vector \mathbf{m} (perturbation sound speed) to the data (perturbation travel time), and \mathbf{n} is the data error; then the desired inverse operator is (Aki and Richards, 1980; Menke, 1989)

$$\mathbf{G}^{-g} = \mathbf{W}\mathbf{G}^T(\mathbf{E} + \mathbf{G}\mathbf{W}\mathbf{G}^T)^{-1}$$

and

$$\hat{\mathbf{m}} = \mathbf{G}^{-g}\mathbf{d},$$

where \mathbf{W} is the *a priori* covariance matrix, \mathbf{E} is the data error covariance matrix, and $\hat{\mathbf{m}}$ is the estimated model vector.

EMPIRICAL ORTHOGONAL FUNCTIONS

$$T(z) = T_0(z) + \sum_{i=1}^3 a_i Z_i^T(z)$$

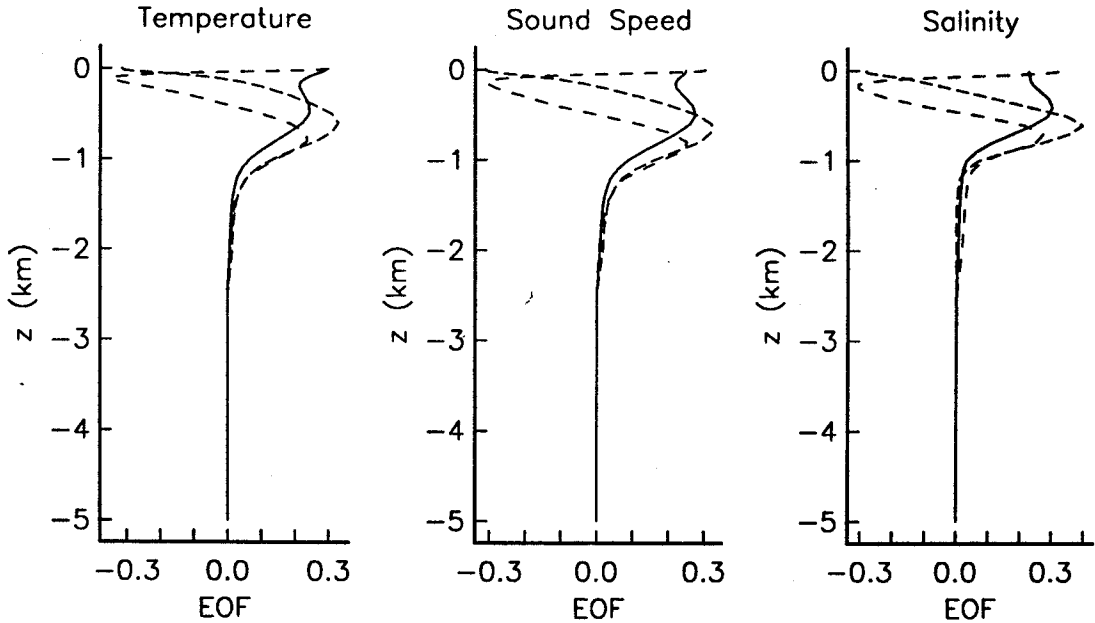


Figure 18. Empirical orthogonal functions used in the analysis (supplied by M. Carnes, NOARL). These were generated from all the MOODS data in the general Gulf Stream area, excluding the shelf water. Note the similarity between the temperature and sound speed functions.

A very important product of the least-squares inversion is an estimate of the output model errors:

$$E = (I - GG^T)W.$$

The ability to quantify the estimated errors rigorously cannot be overemphasized. This error covariance matrix embodies a large amount of information not directly contained in the model parameters. For the tomography case, it is this matrix that carries a significant portion of the information about the spatial averaging nature of the acoustic measurements. The ability to calculate a full error covariance function enables one to run a full Kalman filter and/or to interface with other data assimilation schemes without losing information.

The role of the *a priori* covariance is to tell the inversion process where most of the uncertainty in the present model is. The inversion will distribute the information in the data to the model parameters with the most uncertainty. For instance, when there is only a single front in the slice, the only uncertainty is in the front location, so changes in travel time would be directed to changing the front location. If rings are present, the situation becomes more difficult, and one relies even more heavily on the *a priori* information to determine how the information content of the data should be distributed.

2.4.2 Steps in the Analysis

The actual steps in our analysis procedure are outlined in Figure 19, with example output in Figures 20–30. We will use the section along path 1006 on day 199 as an example (an AXBT survey was conducted the same day). We initially convert the OTIS temperature, salinity, and temperature error fields obtained from FNOG (Figure 20) to sound speed and sound speed error using the Chen and Millero (1977) equation (Figure 21). Because our model is based on EOFs in the vertical, we need to determine EOF amplitude errors for each profile as one step in constructing the *a priori* error covariance. We do this by fitting the sound speed error variance profiles to the square of the EOF functions. This would be strictly valid if the actual error covariance matrix were diagonal. As expected, the errors reach a peak near the Gulf Stream and the slope/shelf front (Figure 22). The next step is to increase the errors to account for the way OTIS handles its errors. The Gulf Stream frontal analysis produced by OOC is based on IR satellite photographs. In regions obscured by cloud cover, the OOC analysts estimate the front and ring locations based on past photographs and their own experience. Because of this subjectivity, the Navy refers to this frontal analysis as a “bogus.” The bogus frontal analysis from OOC plays a dominant role in determining the OTIS fields; often, these are the only data going into OTIS. When OTIS assimilates the bogus analysis, it assumes that it is perfect and has no error, and that there is no lag in time. In practice, there is a 24 to 48 hour delay between the time stamp of the IR satellite images used in the OOC

analyses and the OTIS analysis time. We presently increase the EOF amplitude errors by an amount related to the estimated time delay:

$$\text{error}_{\text{new}} = e_0 - [e_0 - e(t)] \times \exp[-(dt/\tau)^2],$$

where e_0 is the error in the absence of any information (the EOF eigenvalues, from M. Carnes), $e(t)$ is the error we get from the profile fit, dt is the time delay (24 or 48 hours, depending on the day of the week), and τ is a time constant that FNOC supplies with each profile. The time constant τ is related to the water mass type and distance from the closest front. At this point, we introduce the one (and only) set of tuning parameters. In our opinion the higher two modes received too much weight (the end effect was to perturb the Sargasso Sea too much). The variances were therefore decreased by multiplying by a factor of 0.7. The sound speed EOF amplitude errors before and after these changes are shown in Figures 22 and 23, respectively; the corresponding error sections are shown in Figure 24. This method of increasing the errors could be improved upon. A more quantitative way would be based on local horizontal gradients and estimates of velocity.

Now we have an estimate of the initial error variance of each EOF amplitude as a function of range along the section. The next step is to incorporate information about the horizontal correlation length scales. FNOC also provides us with estimates of the local correlation length scale, again based on water mass type and distance from the closest front. This information is used to fill in the off-diagonal terms of the *a priori* error covariance matrix using a Gaussian function, Figure 25. In the Sargasso Sea region, correlation lengths are large, producing relatively large off-diagonal terms in the covariance matrix; near the Gulf Stream, correlation lengths are small, producing smaller off-diagonal terms and a peaked covariance.

Although filling in the off-diagonal terms of the covariance matrix in this way is a step in the right direction, it makes the assumption that the correlation function is Gaussian. Near a front, this is definitely not the case because there are correlations between points on one side of a front and the other. The nature of the front has been ignored in handling the errors this way. The present procedure produces more degrees of freedom to solve for than may actually be present.

All the pieces for the inversion are now in place: the travel time data, the data error, the initial reference state, and the *a priori* error covariance. The inverse program produces the model parameters with error covariance which are then converted to sound speed EOF amplitudes and errors (Figure 26a). As expected, most of the estimated perturbation occurs where the *a priori* errors are largest. These, in turn, are converted to temperature EOF amplitudes with errors (Figure 26b, using M. Carnes' regression procedure) and then to sections of sound speed and temperature (both perturbation and total) with errors (Figures 27–29). The depth-averaged perturbations in temperature and sound speed are plotted in Figure 30a. The depth average looks very much like the EOF mode 1 amplitude because it had the most variance associated with it. Also, the sound speed and temperature (T) perturbations look very similar because the approximate T – C relation employed is nearly linear. The depth-averaged sound speed and temperature errors as a function of range before and after the assimilation of the acoustic data are plotted in Figure 30b. Addition of the acoustic data reduces the variance by approximately 20%, with most of the reduction occurring near the front. This entire process of inversion has been highly automated and is completed on a daily basis.

When the experiment started, we intended to use the OTIS tomography output (i.e., OTIS assimilating the tomography synthetic BT sections and the OOC bogus analysis modified with tomography data) from the most recent day as our starting reference field. Before we began inversion of the travel time data, we sent dummy output files to FNOC to set up the communication links. On 8 August, we began travel time inversions sending “real” fields to FNOC and reporting frontal positions to OOC. By 22 August, it was clear that the procedure was not working. There were several reasons, the foremost being that error estimates by OOC and FNOC were not adequate to keep our data assimilation/inversion scheme on track. The problem was exacerbated by misidentifying travel times for 3 days, by a software error in our front-finding program that affected the value reported to the OOC (discovered 4 September), by the OOC not taking into account the offset between our definition of a front (15°C isotherm crossing 200 m) and

theirs (maximum cross-stream IR radiance gradient), and by OTIS retaining the tomography data for 10 days. On 22 August, we switched to using the standard OTIS product as our reference state.

2.5 Other Data

Six AXBT flights were flown in support of the experiment (Boyd and Linzell, 1990a and 1990b). The flights took place during the intensive transmission periods (16–22 July and 10–16 September). The flights in July covered paths 1006 and 1001; in September, paths 1006 and 1015 were covered. Near fronts, the sample interval was as small as 6 km; away from fronts, it was approximately 40 km. A mixture of 400 m and 800 m probes were used.

Infrared AVHRR satellite images were archived by NOARL for the two intensive sampling periods. Some of the images were of high quality (Figure 31). These images are the same ones OOC uses in their bogus analysis (although they use the images unconverted from radiance); during July and August the viewing was unusually good (88%; personal communication, J. Mosler, OOC) whereas in September it was worse. Keep in mind that during the winter there may be no usable images for as long as a month and that, on average (over space and time), 40% of the satellite images are cloud filled.

From 16 July to 22 July the SURTASS (Surveillance Towed Array Sonar Segment) ship USNS *Bold* towed a horizontal array on a northeast course north of the Gulf Stream. This provided almost continuous data coverage along the ship track. Sample arrival patterns are shown in Figure 32.

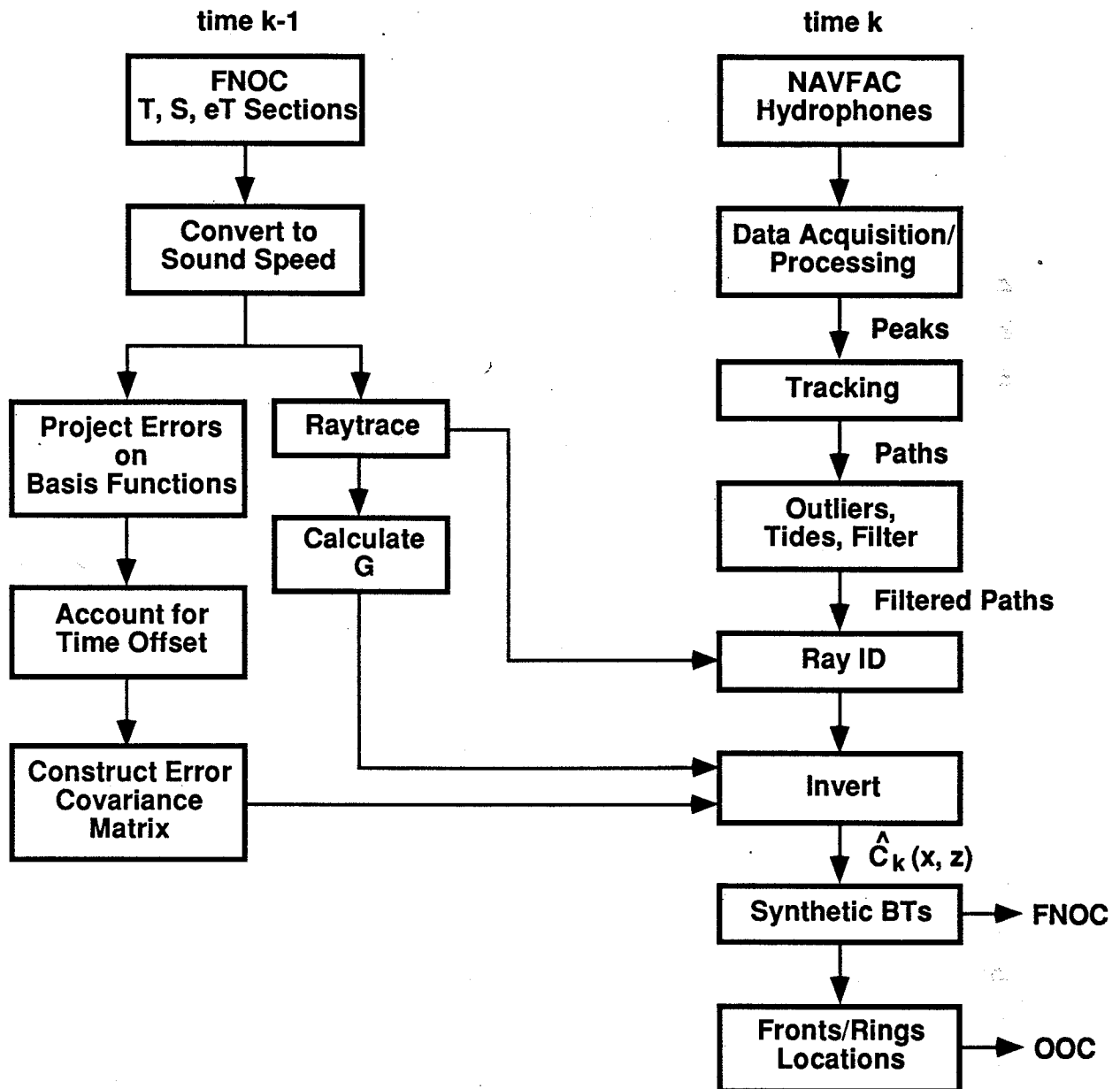


Figure 19. Data analysis flow chart.

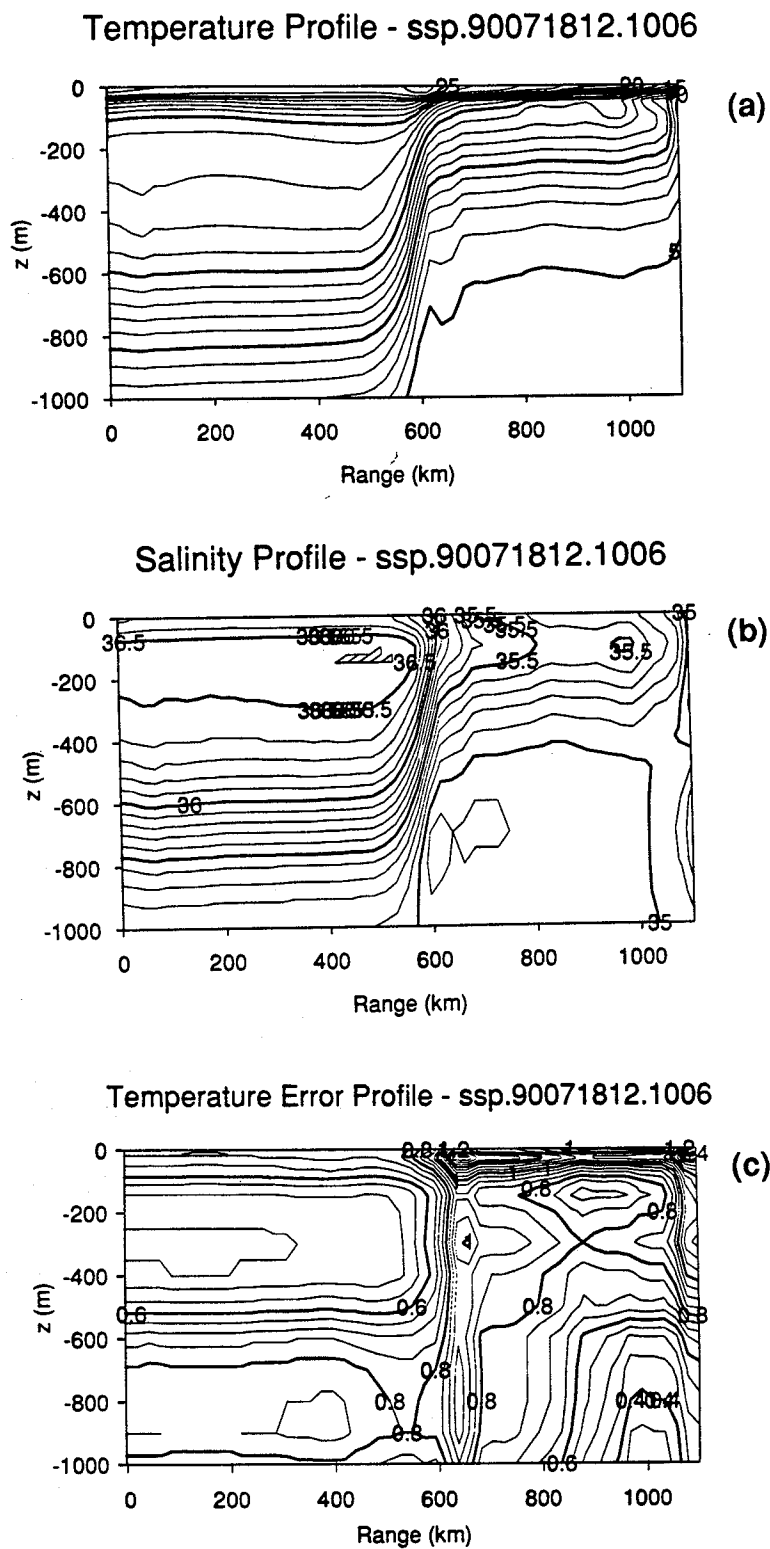


Figure 20. OTIS sections along path 1006 on 18 July 1990. (a) temperature ($^{\circ}\text{C}$), (b) salinity (‰), and (c) rms temperature error ($^{\circ}\text{C}$).

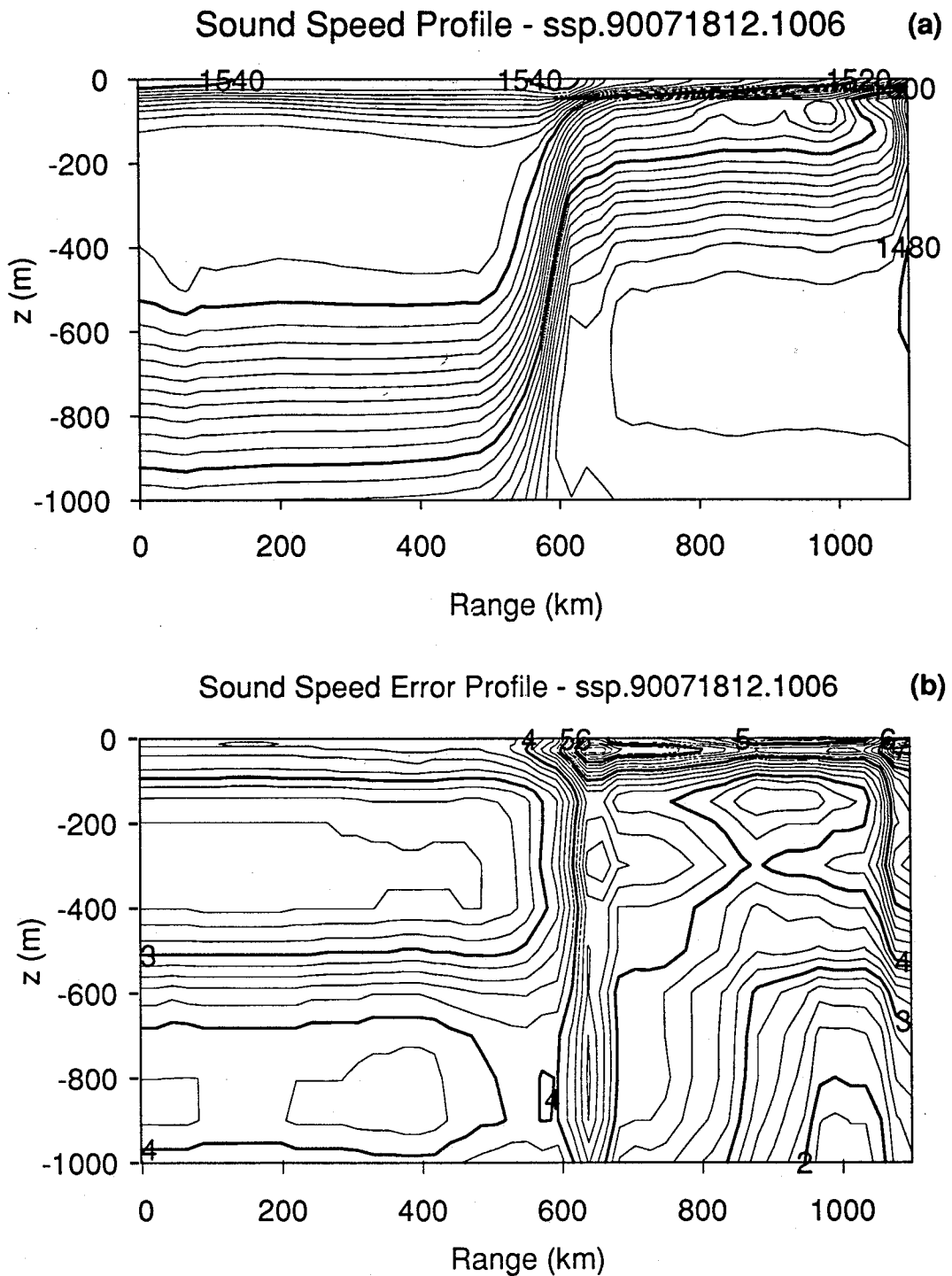


Figure 21. (a) The sound speed field (m/s) derived from the temperature and salinity fields given in the previous figure; (b) rms sound speed error (m/s).

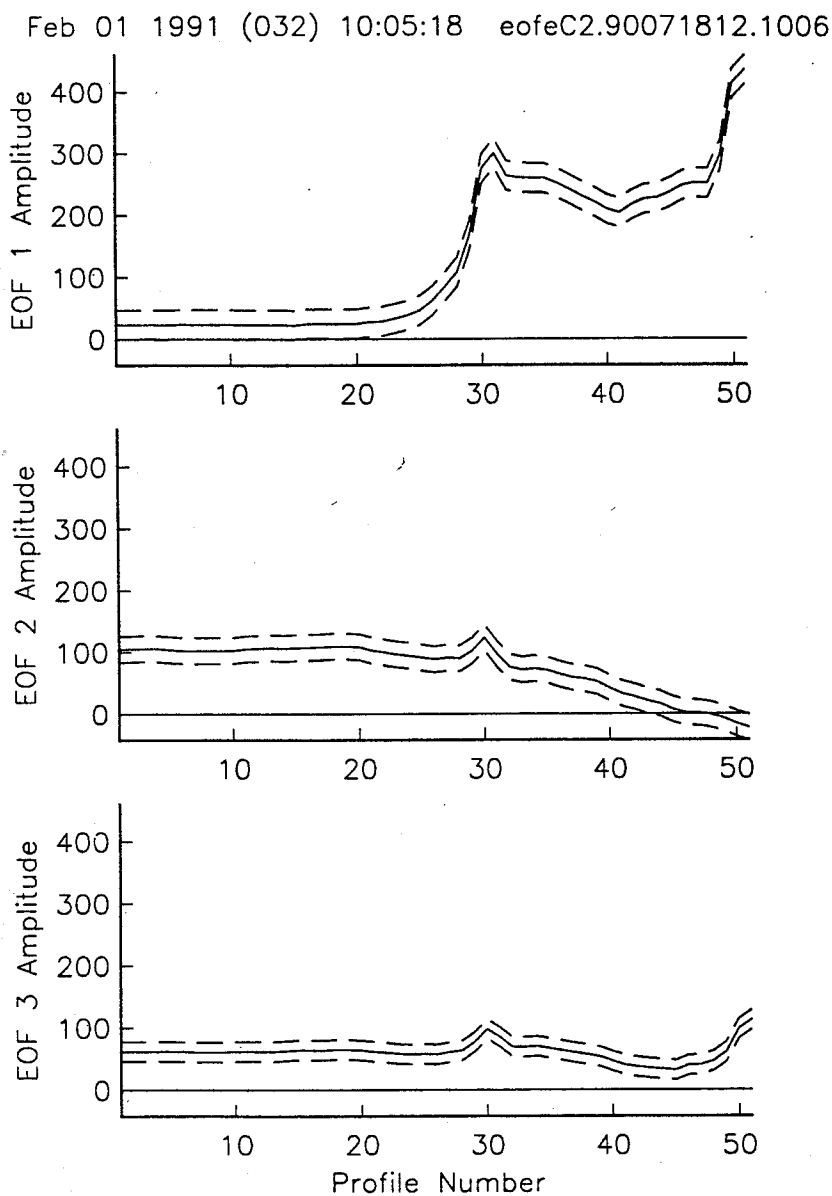


Figure 22. EOF amplitude error variances as a function of range along the 1006 path. This is the result of performing a least-squares fit of the sound speed error variance profiles to the squared EOFs. The abscissa has units of profile number. There are 22 km per profile for a total slice length of 1100 km.

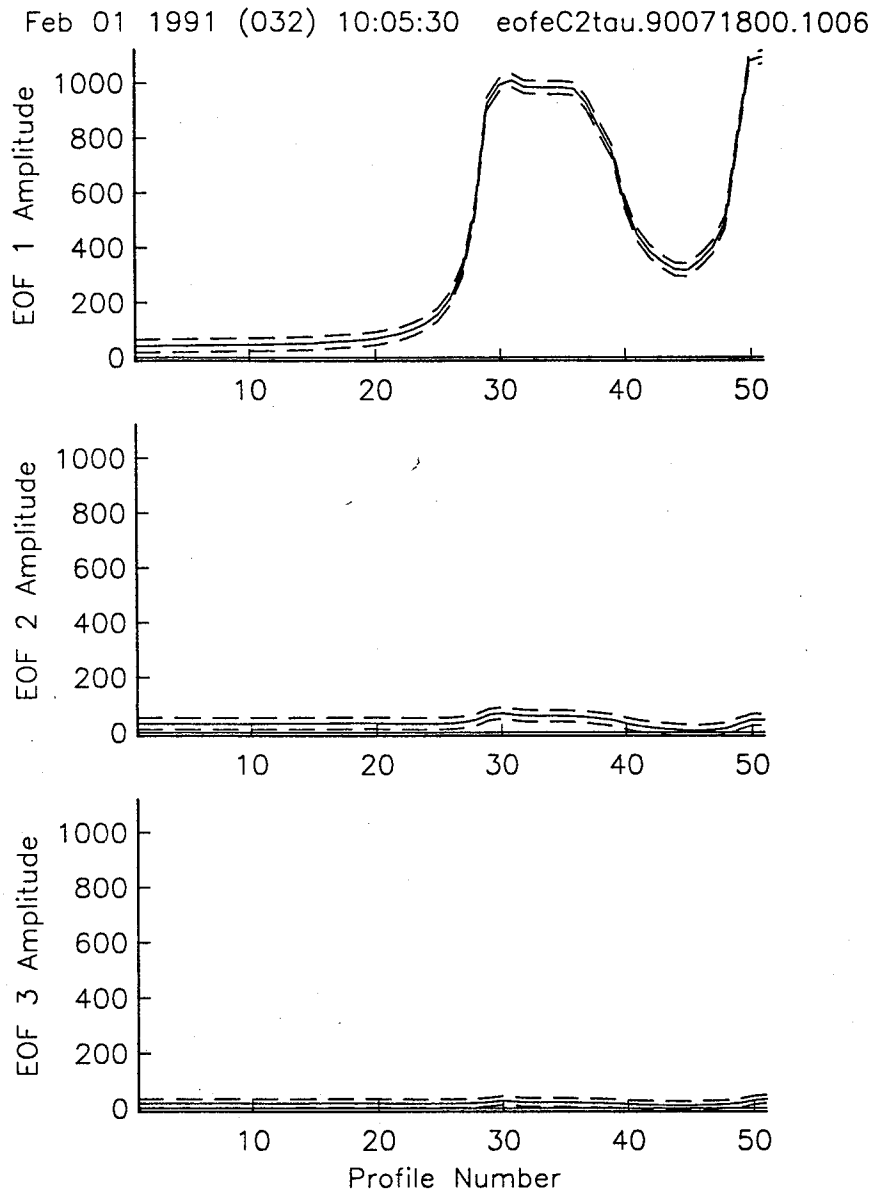


Figure 23. EOF amplitude error variances after being increased to account for time offsets. (Note different scale on ordinate for Figure 22.)

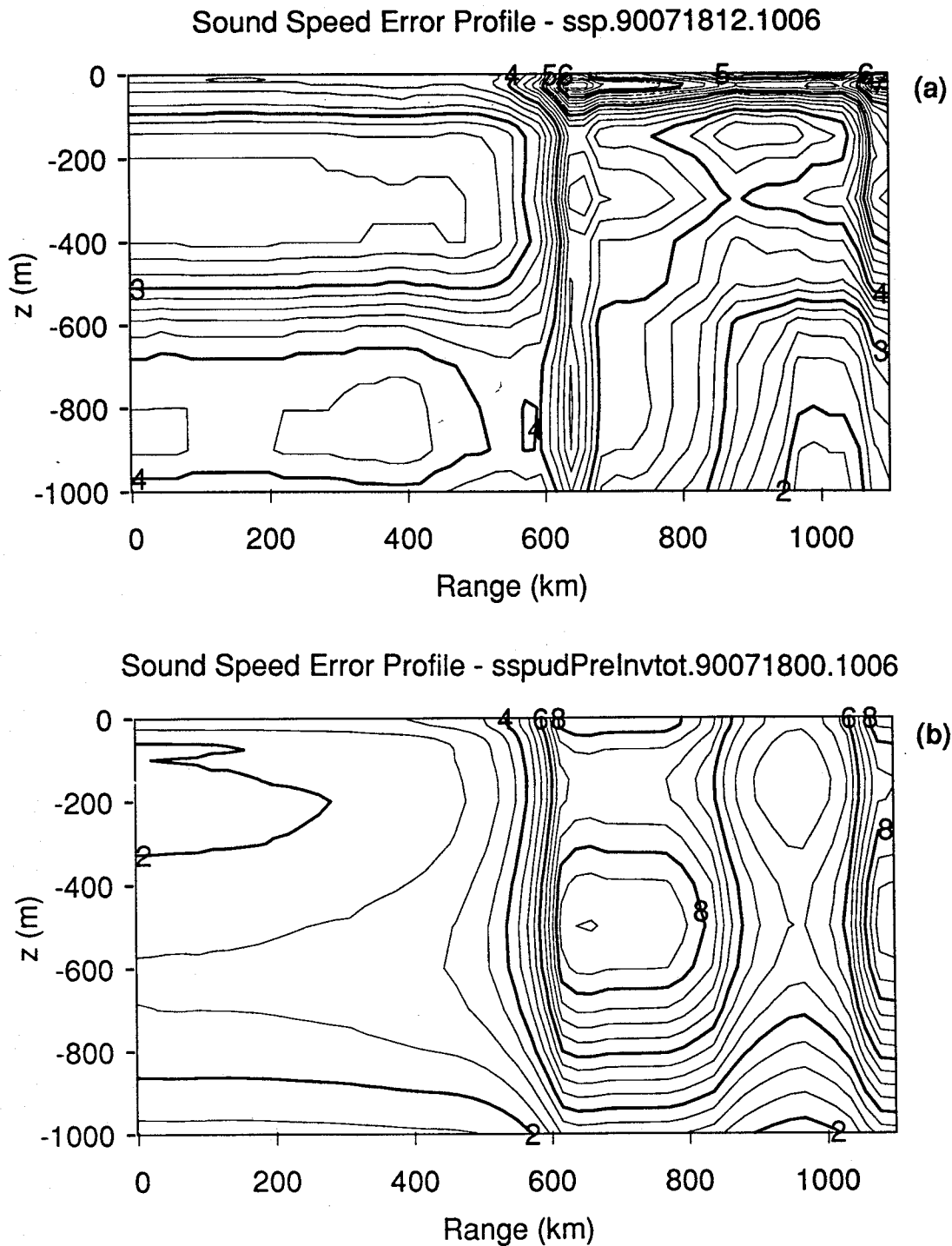


Figure 24. Sound speed error section (a) from OTIS and (b) after increasing the errors.

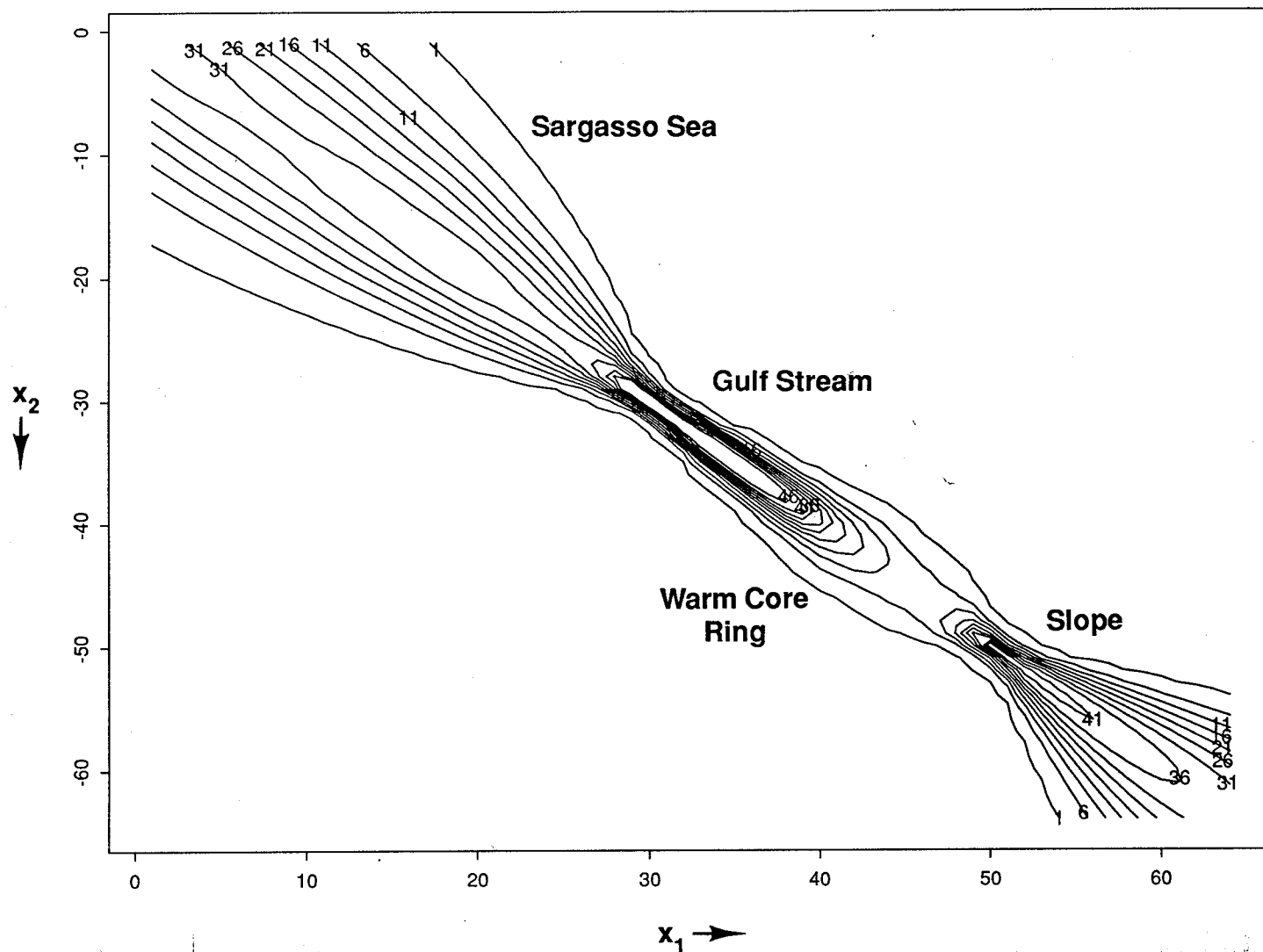
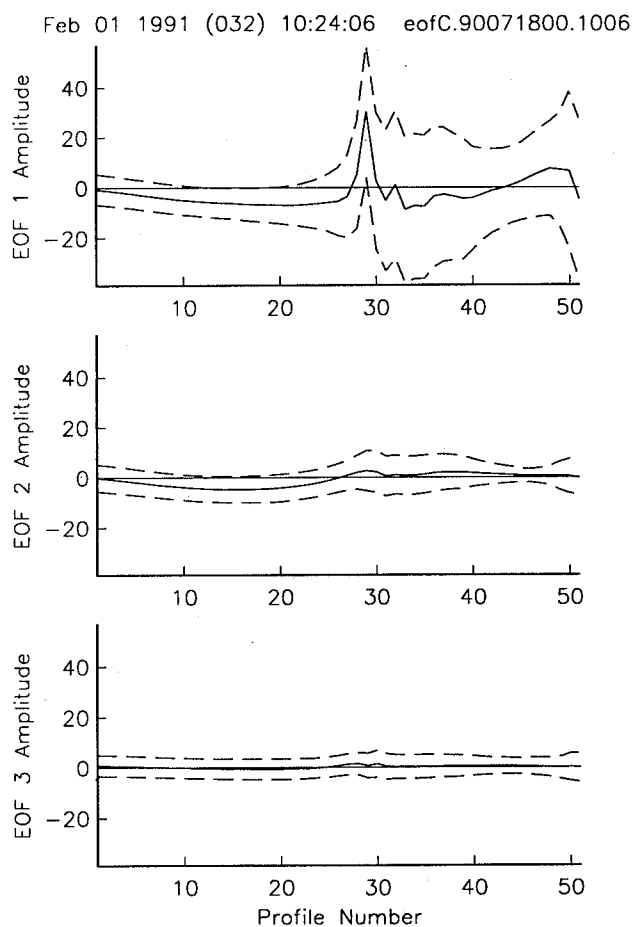
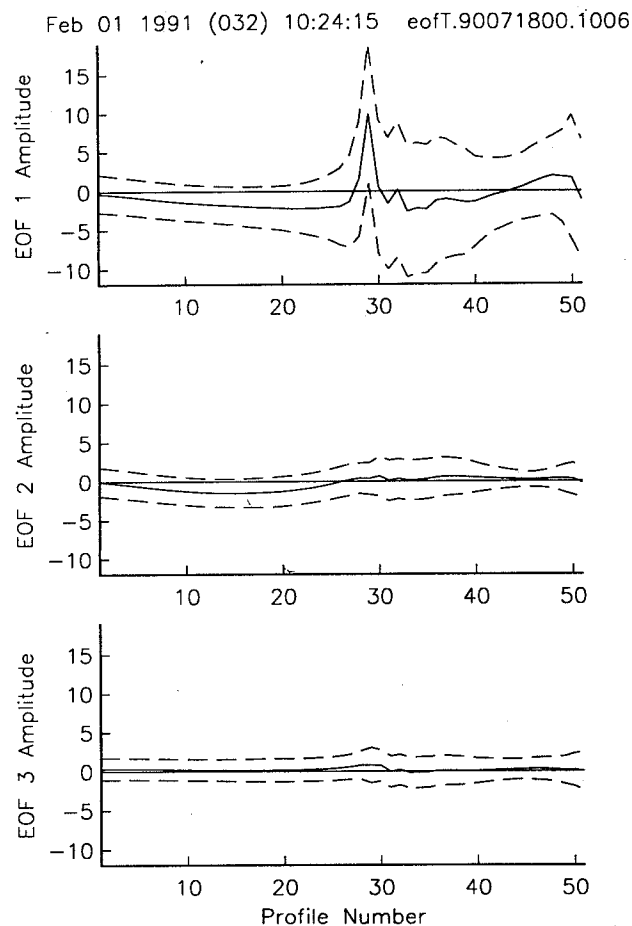


Figure 25. Covariance matrix for EOF 1; x increases from Bermuda. This is an estimate of how the errors at one point are correlated with those at another point along the slice.



(a)



(b)

Figure 26. (a) Sound speed and (b) temperature EOF amplitudes and standard errors as a function of range along path 1006 after assimilating the travel time data.

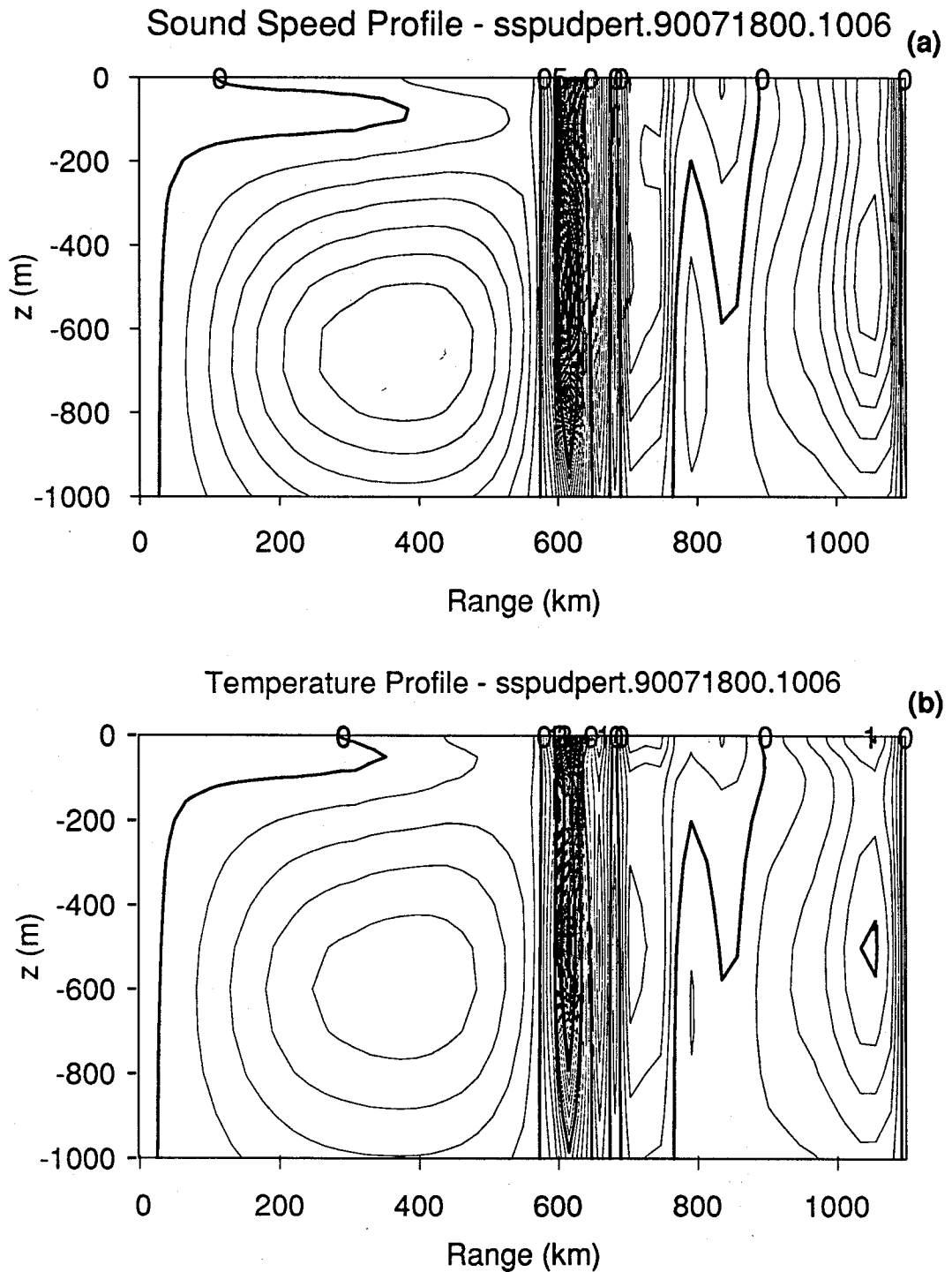


Figure 27. (a) Sound speed and (b) temperature perturbations as a function of range and depth corresponding to the EOF amplitudes in Figure 26.

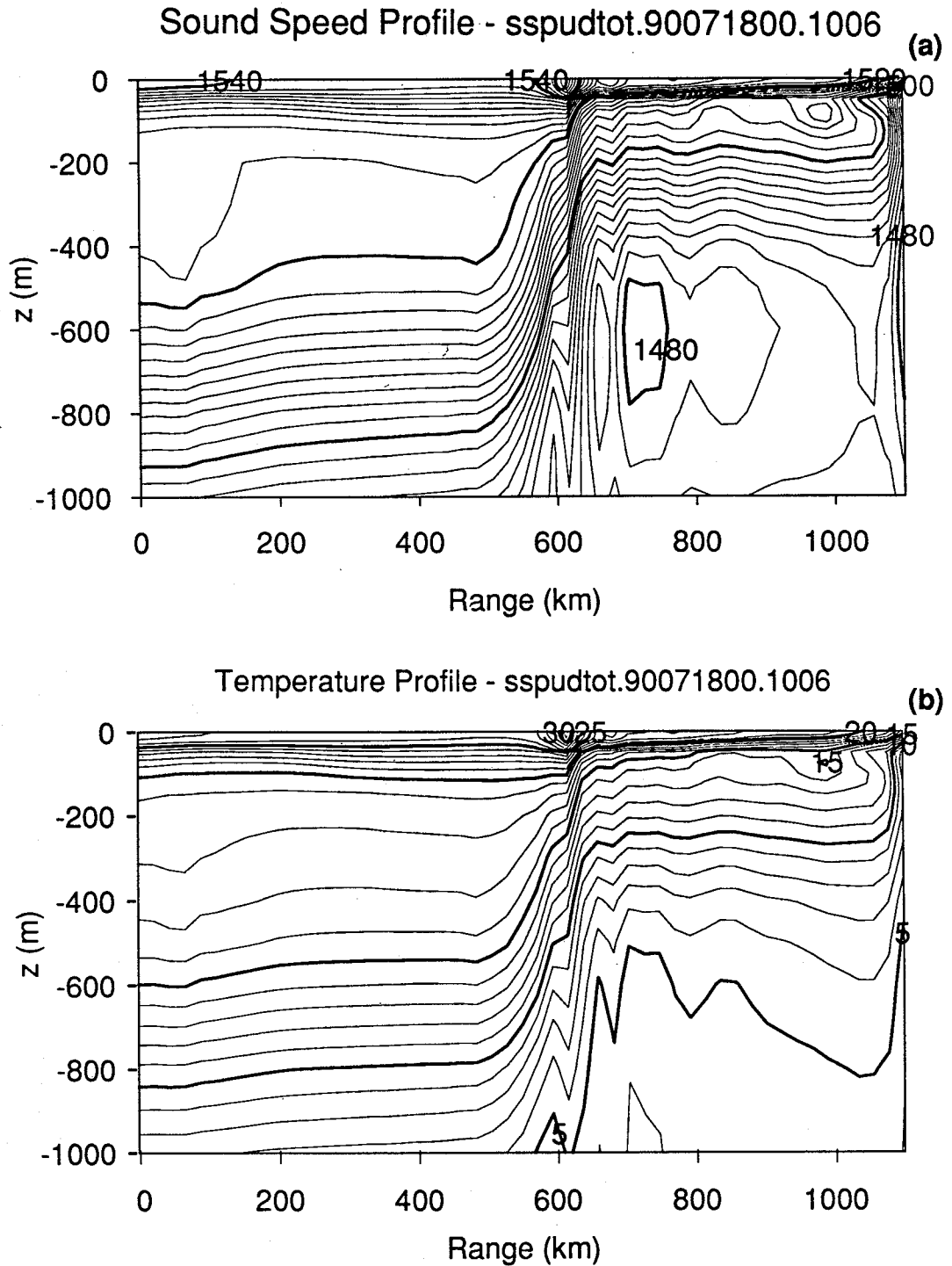
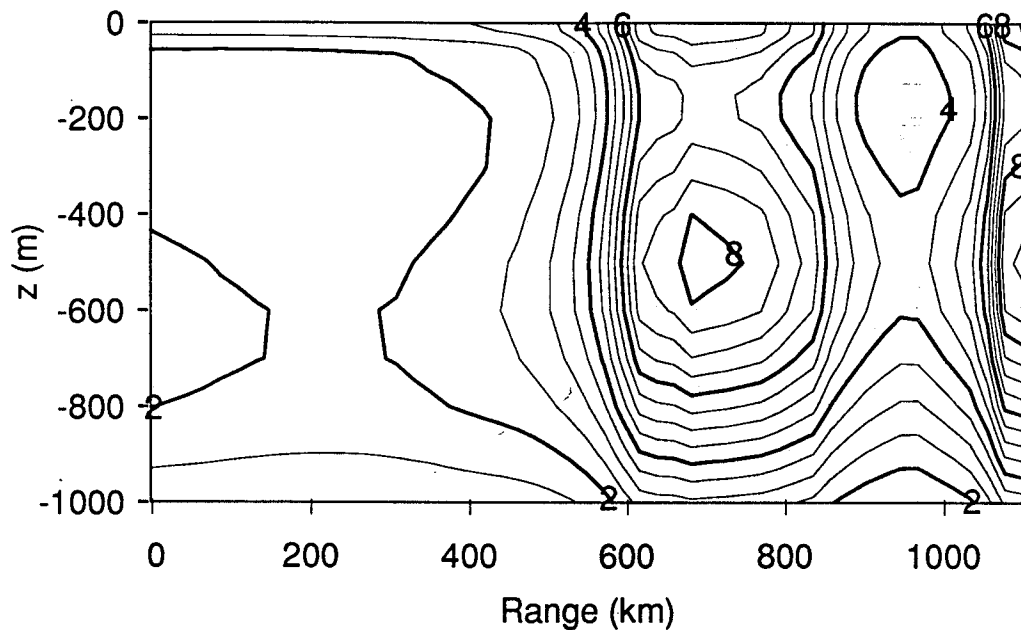


Figure 28. (a) Total sound speed and (b) temperature sections (the perturbations in Figure 27 added to the OTIS reference sections, Figures 21 and 20).

Velocity Error Profile - sspudtot.90071800.1006



Temperature Error Profile - sspudtot.90071800.1006

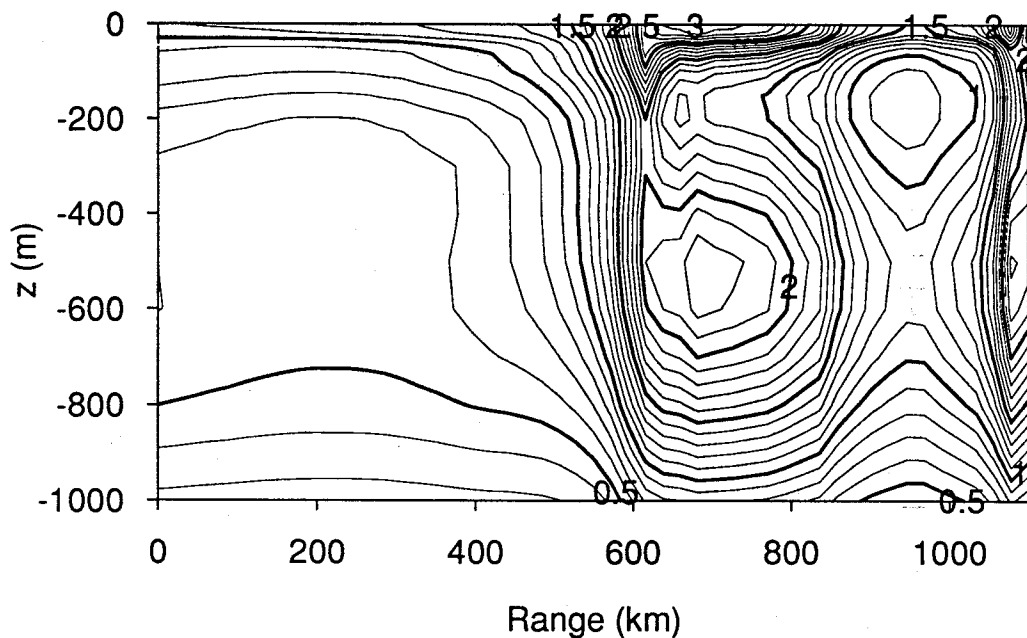
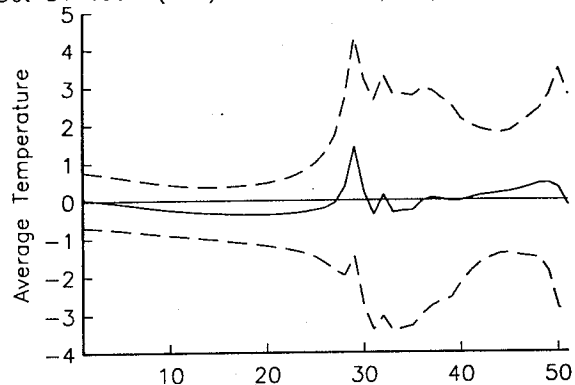
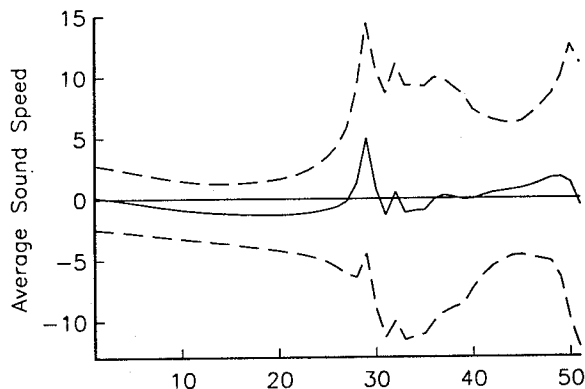


Figure 29. Estimated errors in the sound speed and temperature sections. The sound speed errors can be compared with those in Figure 24b.

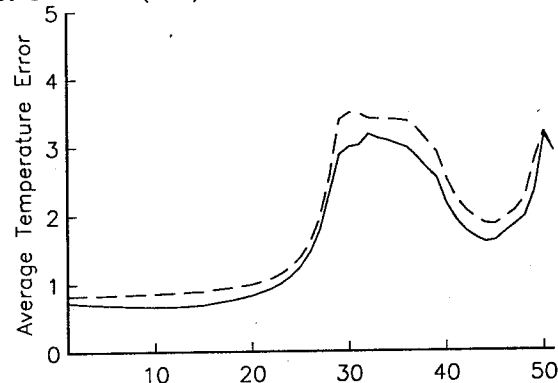
Oct 31 1990 (304) 10:10:15 sspudvpert.90071800.1006



(a)



Oct 31 1990 (304) 10:12:31 sspudvpert.90071800.1006



(b)

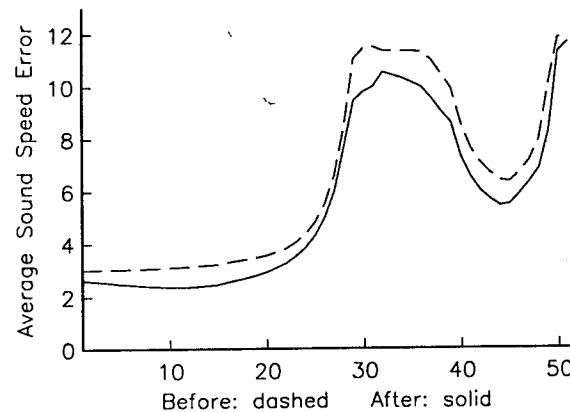


Figure 30. (a) Depth-averaged sound speed (m/s) and temperature perturbations ($^{\circ}\text{C}$). (b) Depth-averaged rms sound speed and temperature error before and after assimilation of the tomography data.

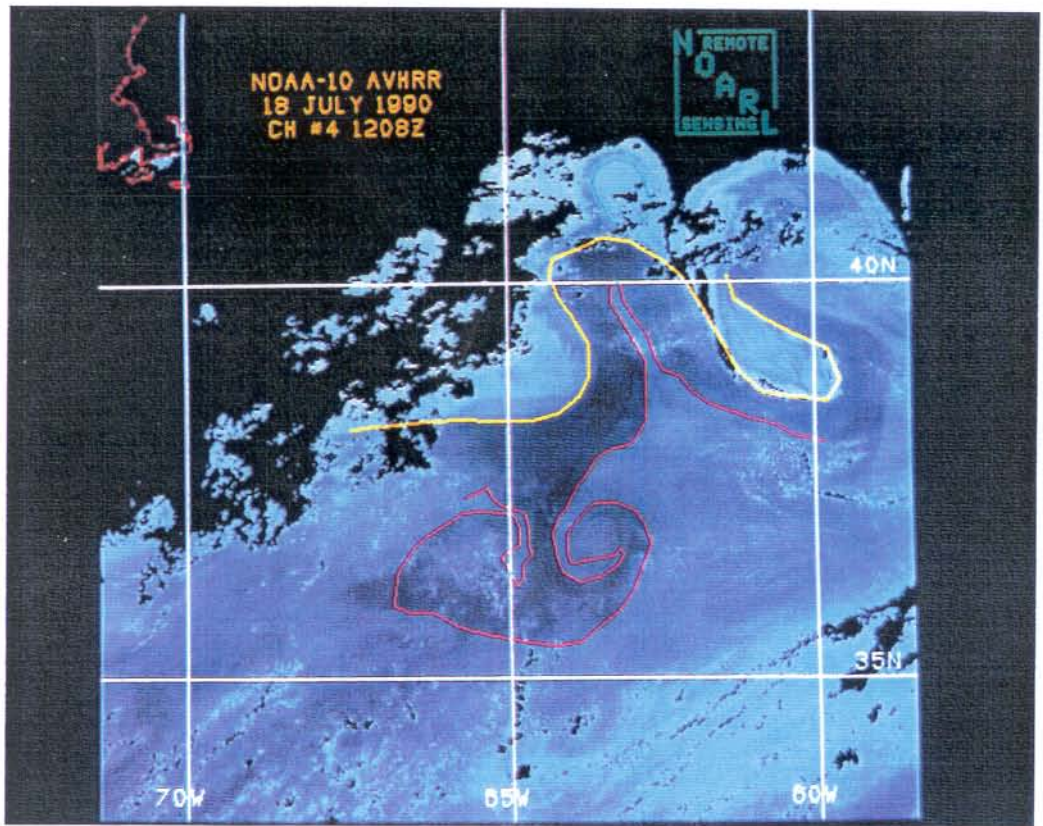
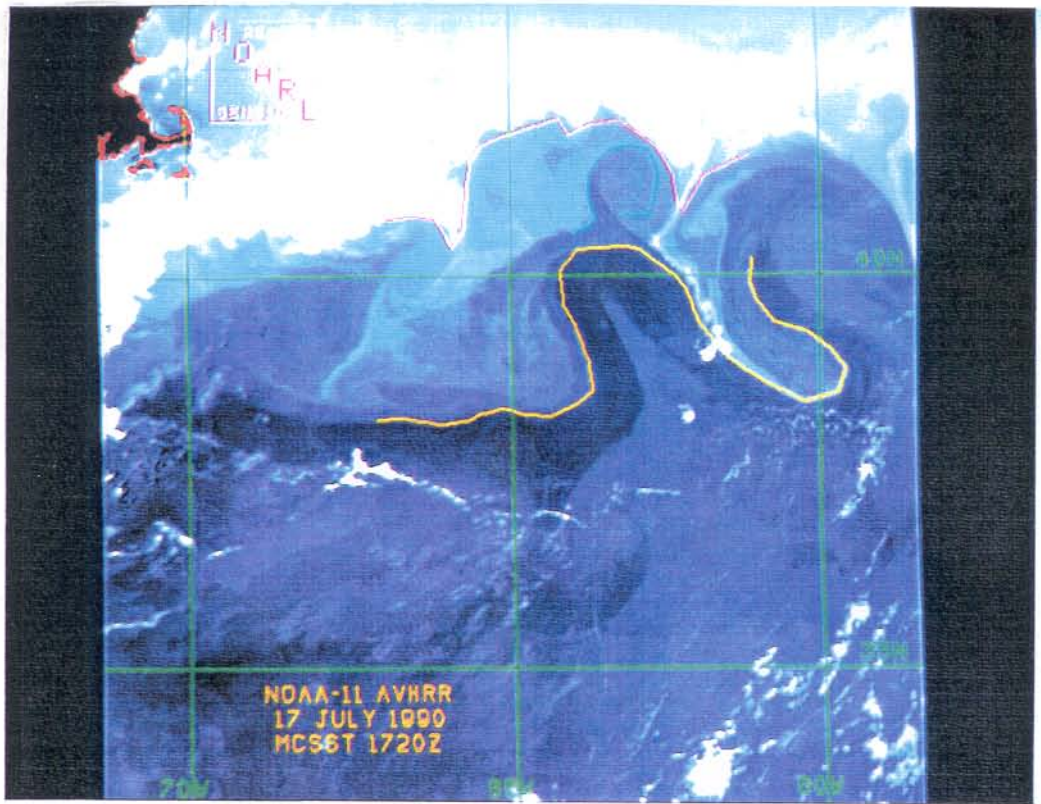


Figure 31. Sea surface temperature in the experimental area, from AVHRR satellite data. Frontal features have been identified by D. Johnson, NOARL. White is 5°C or colder and black is 25°C or warmer.

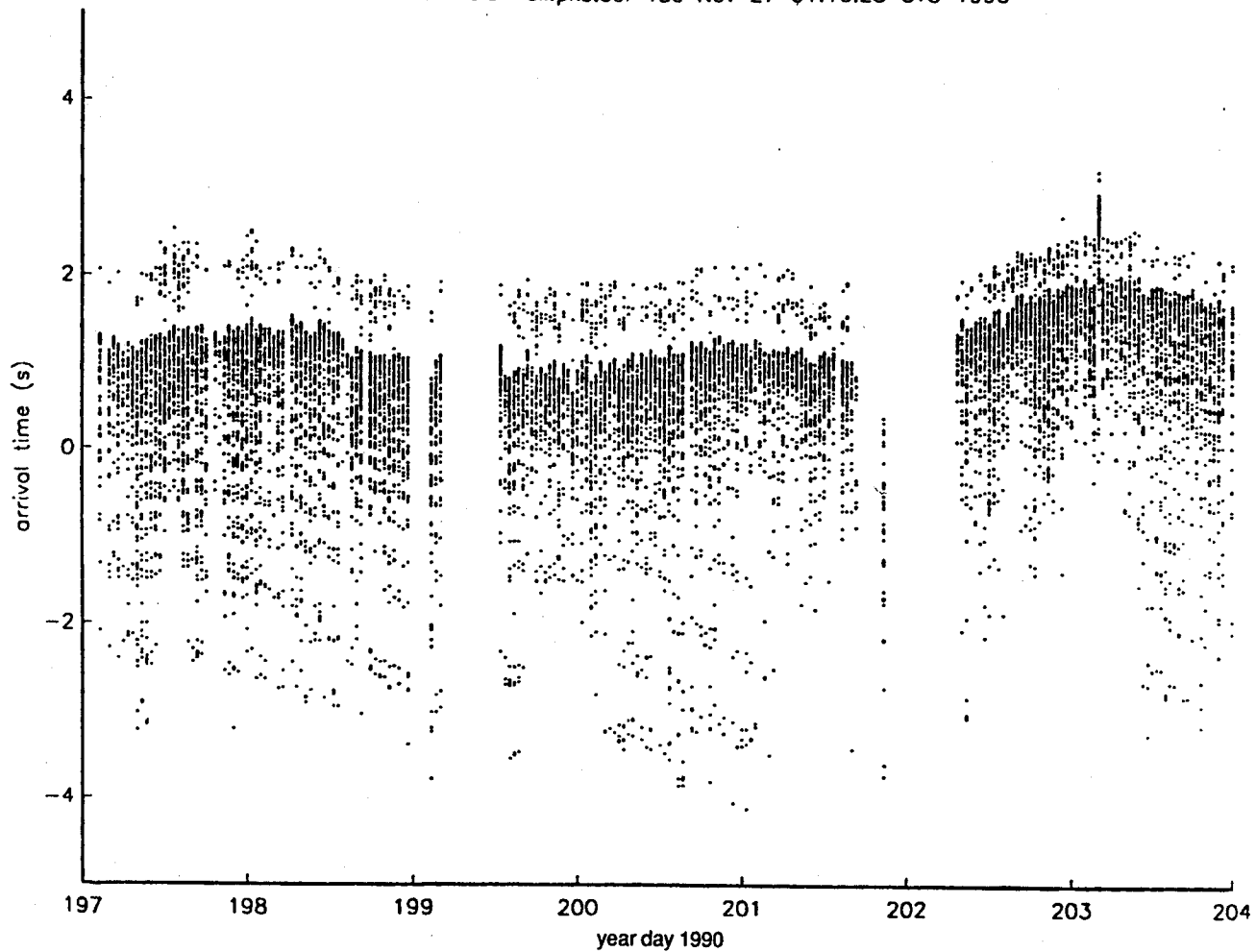


Figure 32. Dot plot of the acoustic arrival patterns measured on the towed array from USNS Bold.



3. RESULTS

3.1 Comparisons with AXBT Data

The AXBT data for path 1006 taken between 1210Z and 1510Z on day 199 (18 July 1990) are plotted in Figure 33a. This plot is the raw data and is contoured only to 300 m to avoid any interpolation effects between the BTs and historical data. The OTIS field to 300 m for 1200Z on the same day is shown in Figure 33b. The OTIS Gulf Stream is much smoother than the “measured” Gulf Stream. This is not unexpected, considering that the OTIS front is constructed from a feature model. The same OTIS field to 1000 m is shown in Figure 33c and the AXBT+OTIS field in Figure 33d. The latter field is obtained by fitting the AXBT data to our model in exactly the same way as we fit the travel time data, using the OTIS field as the reference. This smooths the AXBT data somewhat, but the Gulf Stream is still sharp. The estimated error is 0.5°C. Similar plots for the AXBT data taken between 1230Z and 1510Z on day 203 (22 July 1990) are shown in Figure 34.

The temperature fields shown in Figures 33 and 34 are relatively simple; only the Gulf Stream is present (though there are indications of nearby warm- and cold-core rings). Thus we expect the simple relation between Gulf Stream location and travel time to apply; i.e., for every change of 100 ms in travel time, the position of the Gulf Stream should change by 20 km. (Various equivalent forms of this conversion factor are 5 ms/km, 2.5 ms/n.mi., 10 ms/n.mi., or 100 n.mi./s.) We use the position where the 15°C isotherm crosses 200 m depth to define the location (of the northern wall) of the Gulf Stream. Finding this position in the fitted AXBT fields gives a northward movement of 16.7 km over the 4 days (using the AXBT derived position on day 199 as the reference). The change in the measured mean travel time (over exactly the same time interval) was 88 ms. This is equivalent to a change in position of 17.2 km—or a difference of 0.5 km between the AXBT and acoustically determined Gulf Stream positions!

These relative positions are plotted in Figure 35 along with Gulf Stream positions determined from the acoustic measurements. These show that the general trend over this time period is a northward movement of the Gulf Stream. Also plotted are estimated (standard) error bars for the relative positions. The error in the AXBT-derived front

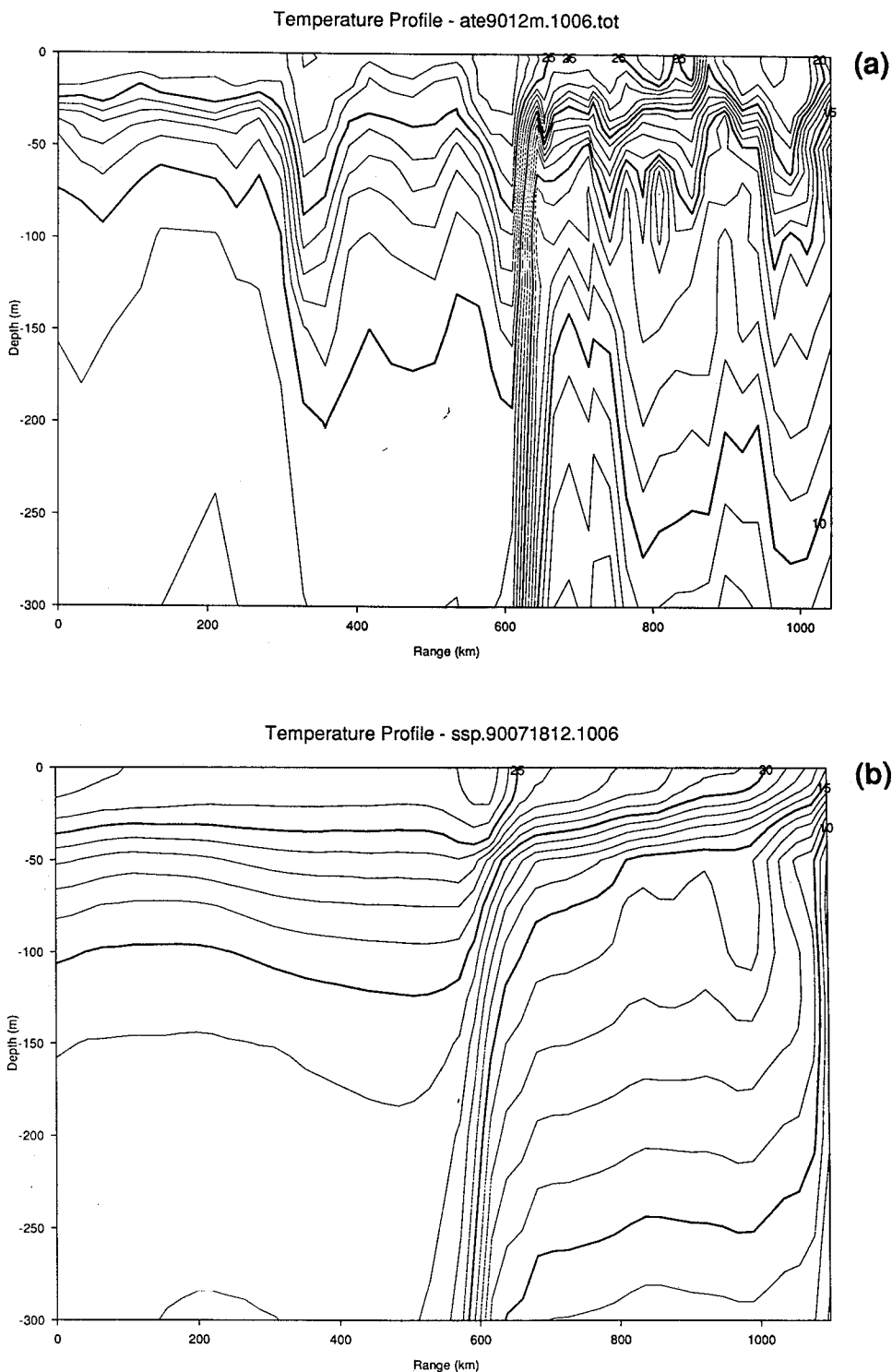


Figure 33. Temperature sections from 18 July along slice 1006. (a) Raw AXBT data (contoured) to 300 m; (b) OTIS data to 300 m; (c) OTIS data to 1000 m; (d) AXBT data combined with OTIS data. (Note: Horizontal scales are slightly different.).

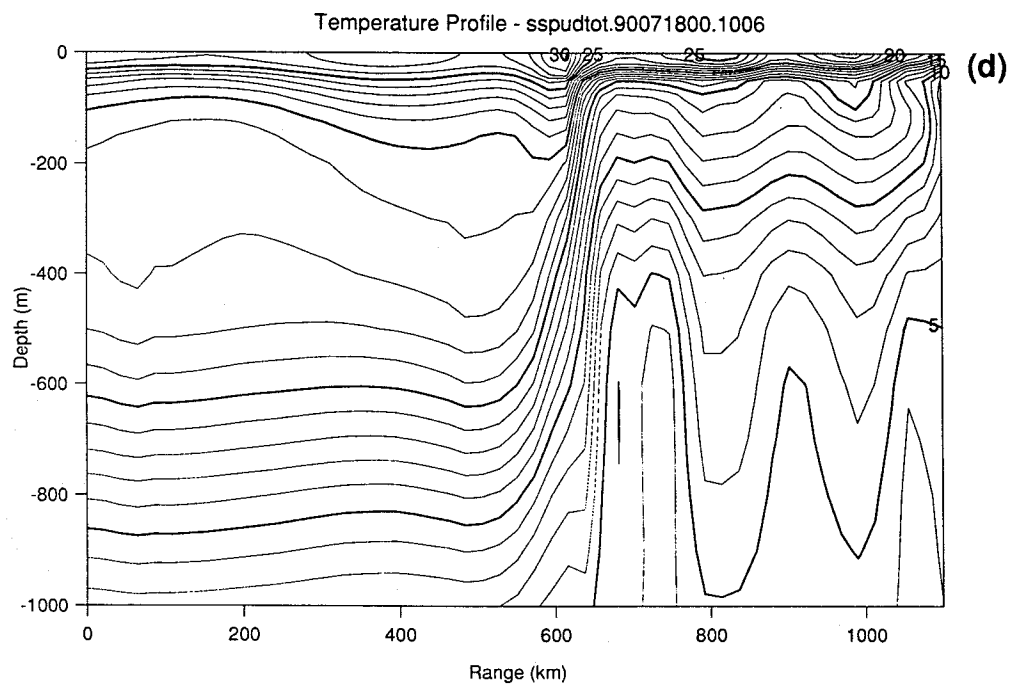
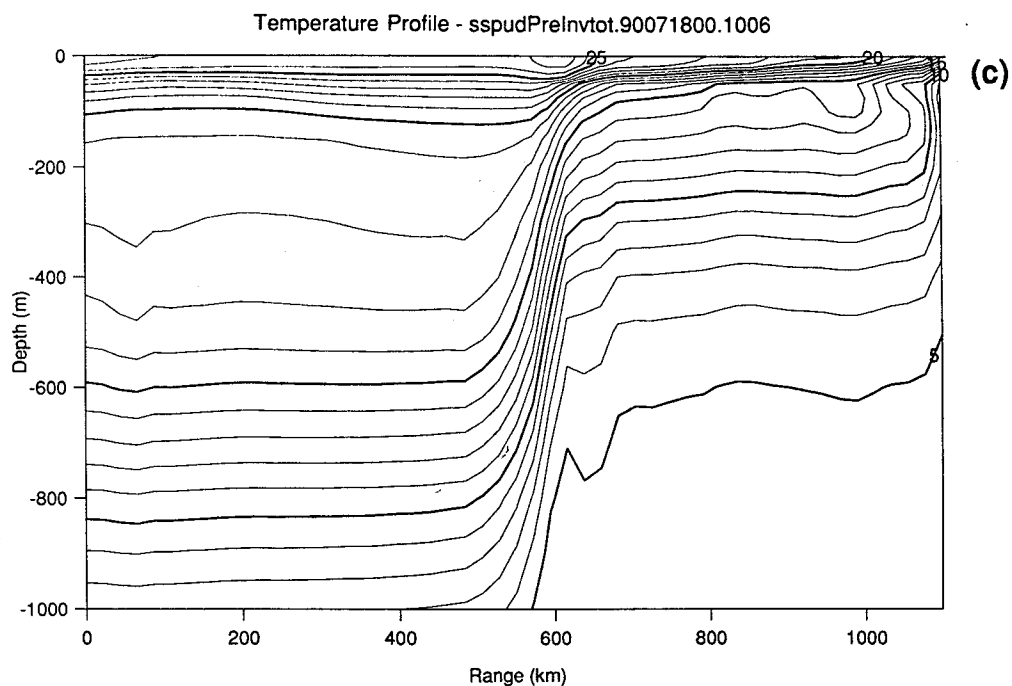


Figure 33. (continued)

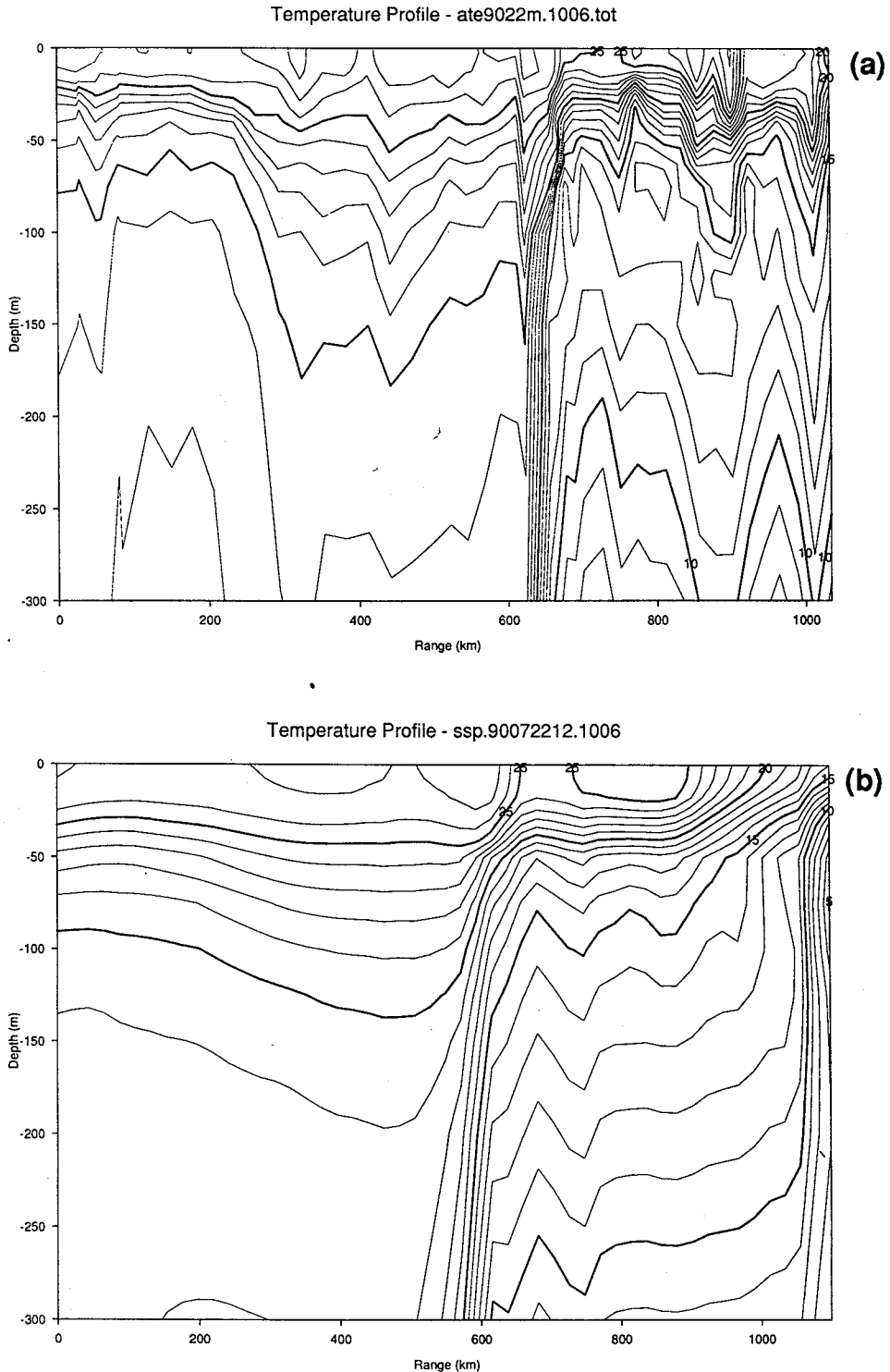


Figure 34. Temperature sections from 22 July along slice 1006. (a) Raw AXBT data to 300 m; (b) OTIS data to 300 m; (c) OTIS data to 1000 m; (d) AXBT data combined with OTIS data. (Note: Horizontal scales are slightly different.).

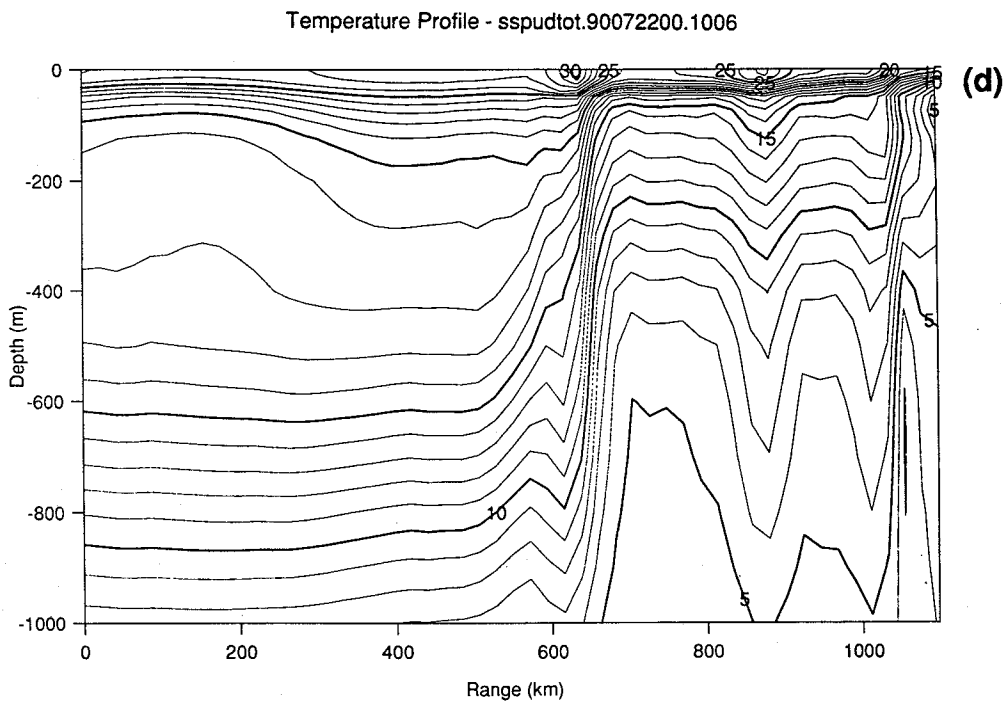
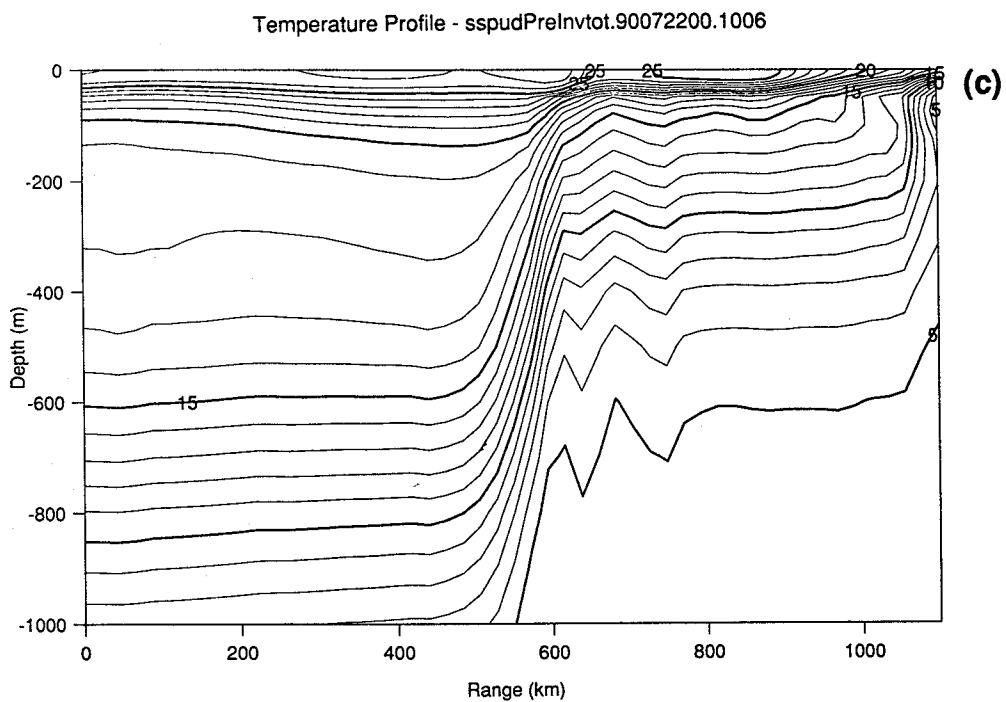


Figure 34. (continued)

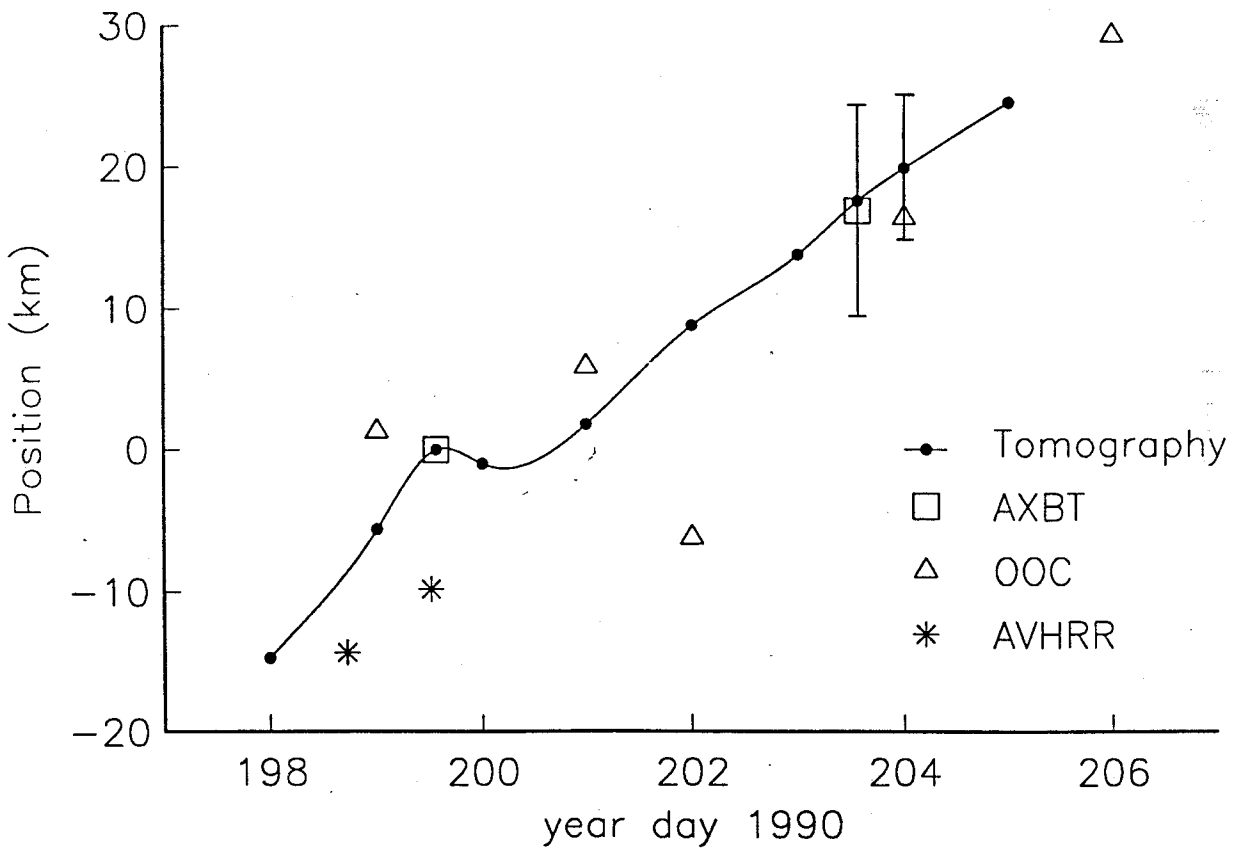


Figure 35. Relative Gulf Stream position from day 198 to day 205 (17 July to 24 July).

positions is about 5 km (based on the temperature error fields); the error in the relative position is then this error times $2^{1/2}$, or 7.4 km. The error bar for the acoustically determined change in relative position is $e/6^{1/2} \times 2^{1/2}$, where e (about 40 ms) is the estimated measurement error for an individual ray. The resulting relative error is about 25.0 ms, which is equivalent to 5.0 km. This does not take into account any other possible ocean changes. The AXBT and acoustic relative frontal positions agree within the error bars, with the acoustic error bars being less than the AXBT ones. This extremely simple relation between travel time and frontal location should hold whenever only a simple Gulf Stream is present.

Estimates of the position of the north wall of the Gulf Stream determined from IR satellite images are also shown in Figure 35. The two AVHRR points were derived from

a subjective frontal position analysis made by D. Johnson of NOARL. He traced out the front where he saw a maximum gradient in sea surface temperature (see Figure 31); then the frontal location along the tomography slice was determined by solving for the intersection of the geodesic defining the slice and the curve defining the front. Images from 1720Z 17 July, 1208Z 18 July, and 22 July were processed; the image for 22 July was not usable because of cloud cover, so points for only the first two days are plotted. They lie about 10 km south of the tomography points, and the trend is in the same direction, i.e., northward movement. Frontal positions were also obtained using data from the OOC PC Image Communication System. These data represent the OOC's composite analysis of many IR images (in units of radiance); the ones used by NOARL would be a subset of the ones used by OOC. The OOC frontal position estimates fall near the AXBT points and the tomography points. The time stamp for the OOC data is only good to within an integer day, which may produce some extra scatter. There is a small inconsistency in Figure 35. Typically the surface expression of a front, defined as the location of the maximum cross-stream gradient, is about 20 km north of the position defined by the 15° isotherm crossing 200 m. Thus one would expect the OOC and AVHRR positions to lie north of the AXBT and tomography positions.

The various steps involved in inverting the travel times for 18 July were shown in Figures 20–30. The results for 22 July are shown in Figure 36, and the difference between the tomography results for the 2 days is shown in Figure 37 (day 203–day 199). This difference shows the warming associated with the decreasing travel time; however, the travel time inversion distributes the warming over a larger portion of the slice rather than simply moving the front. This is because the errors supplied by OTIS have many (uncorrelated) degrees of freedom along the slice, not just one associated with the Gulf Stream moving back and forth. In fact, if one really believes there are distinct fronts, then errors on each side of the front should be correlated.

Simple comparisons are not possible for the AXBT data taken on 11 and 14 September because of the extremely contorted Gulf Stream and the warm-core ring that was present. Furthermore, NOARL found no IR images good enough to process; there were

always too many clouds. For each day, the set of AXBT measurements was regridded to match the tomography section grid using conventional optimal interpolation. The interpolation/regridding method is based on standard objective analysis. Vertical plots of the resulting AXBT, standard OTIS, and tomographic temperature sections are shown in Figure 38 for 11 September and in Figure 39 for 14 September. There is a clear difference between conventional optimal interpolation, which uses a fixed-length scale and GDEM climatology, and the OTIS product, which is tailored to the region and uses additional *a priori* information such as feature models, etc. The OTIS and tomography sections show few major differences, but both differ considerably in some regions from the AXBT temperature sections. The center of the warm-core ring in the OTIS section is about 70 km south of the center in the AXBT section, and the radius in the OTIS section is about half that in the AXBT section (65 km vs 110 km) on 11 September. The northern edge of the eddy in the two sections differs by only 10 to 15 km. The incorrect placement of the eddy in the OTIS section is due to inaccuracy of the eddy boundary map prepared by IR imagery. The ocean surface in this region was almost completely obscured by clouds during this period, making an accurate delineation of the eddy boundary nearly impossible.

The warm-core eddy separated from the Gulf Stream on about 7 September and formed an unusual and highly elliptical shape with a major-axis radius of about 160 km and a minor axis radius of about 80 km (see Figure 40). The front and eddy maps show that the ring rotated clockwise between 11 and 14 September, bringing the center, as seen along section 2 (path 1006), closer to the front. This is confirmed in the AXBT section, which shows the eddy center (along section 2) closer to the front, by about 45 km, on 14 September than it was on 11 September. The expression of the ring in this section also weakened during this period, indicating that the ring was moving away toward the west. The OTIS sections show a southward shift of the ring (30 km) between these dates, but a strengthening rather than a weakening of the ring.

In both the OTIS and the tomography sections, the position of the Gulf Stream front (defined as the point where the 15°C isotherm intersects 200 m) on 11 September is about 22 km south of its position in the AXBT section; on 14 September both are about 31 km

south of the AXBT-derived position. Both of these differences are close to the spacing between section profiles (22 km). Much of the difference in the OTIS section can be attributed to inaccuracy in modeling the near-surface warm core of the Gulf Stream. The AXBT section shows downward displacement of isotherms associated with the warm core extending from the surface to over 500 m, whereas the warm core in the OTIS section affects only the upper 100 m and is weak. Addition of a realistic warm-core region to the OTIS fields would steepen the front and move the isotherms northward, more in line with the position shown in the AXBT section. The only major difference between the OTIS and tomography sections is the addition of a sharp upward spike in the isotherms on the northern edge of the Gulf Stream. The AXBT sections show a doming of isotherms in the thermostad zone between the permanent and seasonal thermoclines in the southern half of the Sargasso Water region. Associated with the doming is an increased vertical gradient in the seasonal thermocline. Both features may be due to a large cold-core ring near Bermuda, undetected in IR imagery. Neither the OTIS nor the tomography section distinctly exhibits these features, though both do show a slow increase in the thermocline gradient toward the south; the tomography section also shows a small upward tilt of the isotherms in the southern half of the Sargasso Sea region.

The vertical temperature sections were divided into subregions according to water type and depth interval, and the mean and rms temperature differences among the three types of sections (AXBT, OTIS, OTIS+tomography) were computed for each. The results are shown for the upper two depth intervals (0–100 m and 125–500 m) in Figure 41 for 11 September and in Figure 42 for 14 September. On both dates and in both depth intervals, the rms difference between the AXBT and tomography sections and the AXBT and the OTIS sections is much larger than the difference between the OTIS and tomography sections. On 11 September, the error (compared with the AXBTs) in the upper 100 m for slope water, Sargasso Sea water, and the warm-core ring is substantially smaller in the tomography section than in the OTIS section. The difference in error is less in the deep layer (125 to 500 m). On 14 September, however, the mean errors for the OTIS and tomography sections are equivalent in both depth intervals.

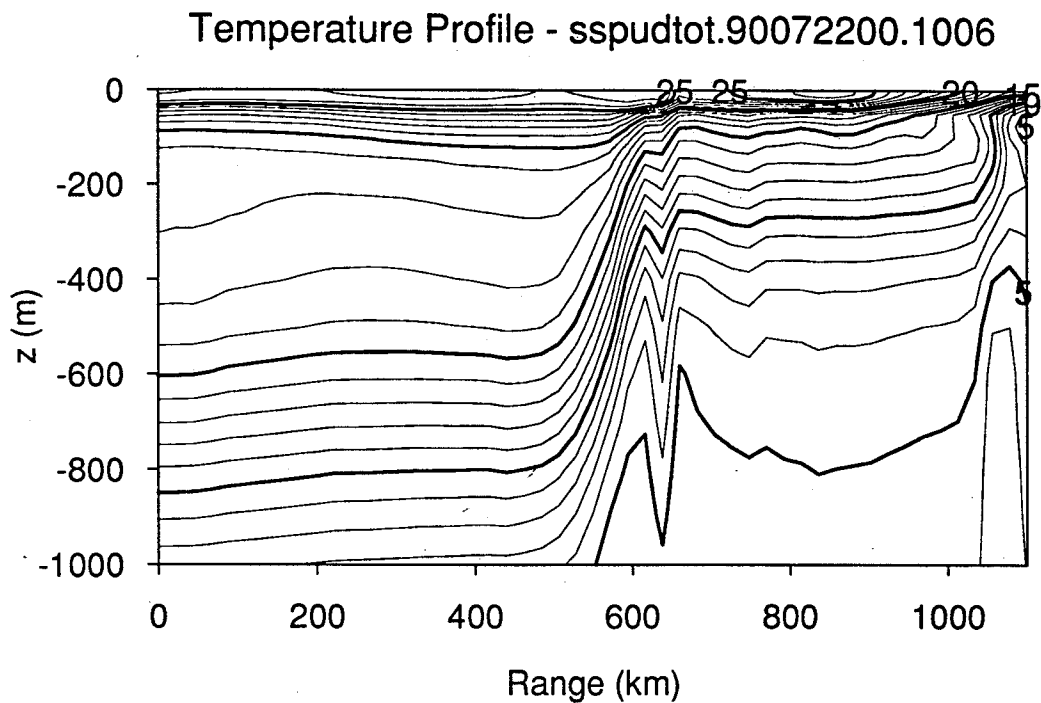


Figure 36. Tomography temperature field for 22 July.

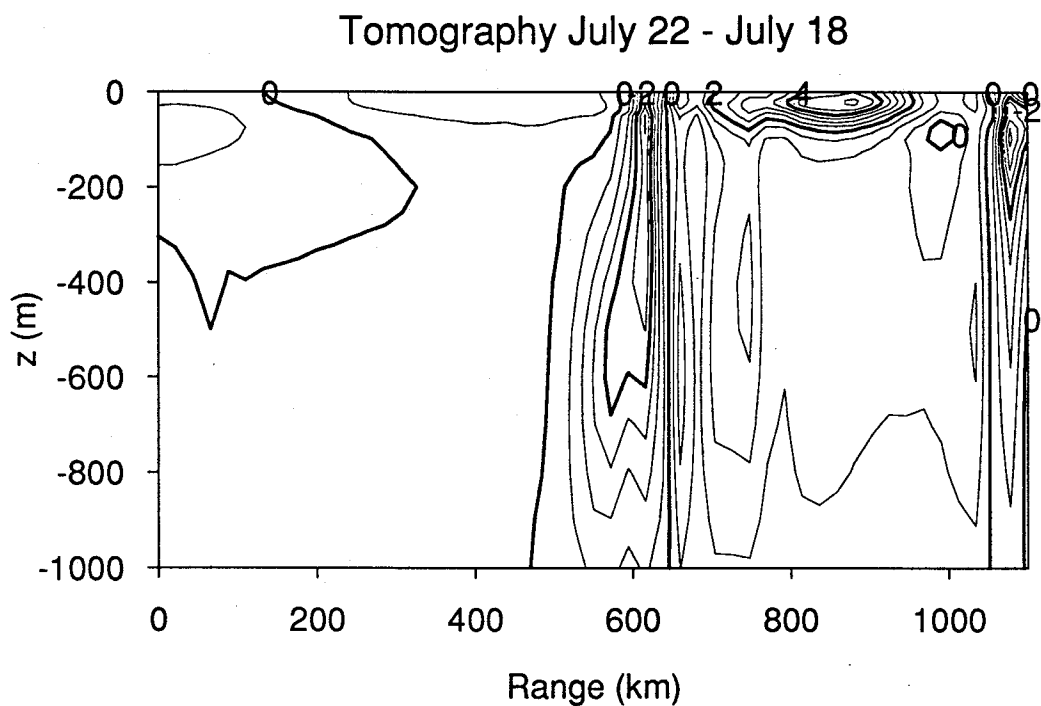


Figure 37. Tomography temperature field for 22 July minus the tomography temperature field for 18 July.

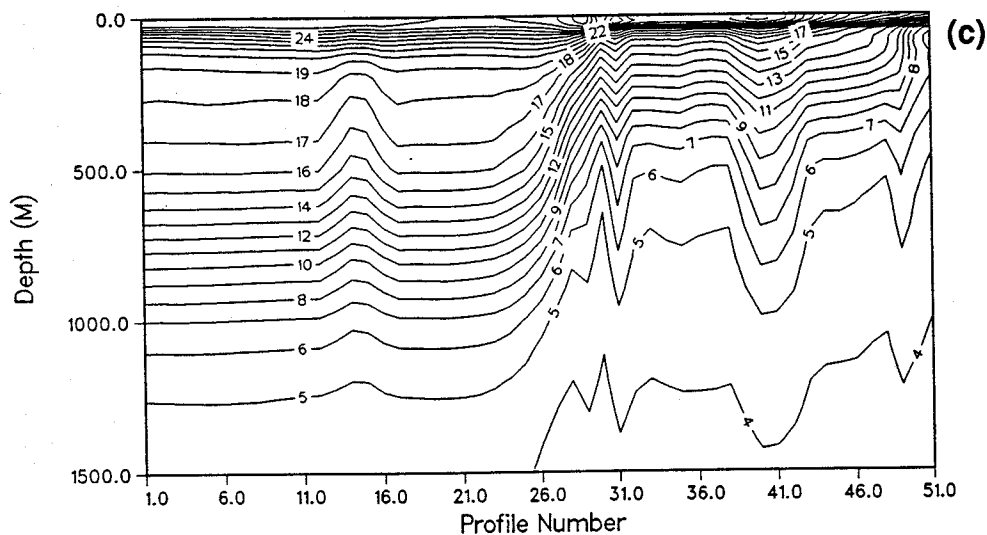
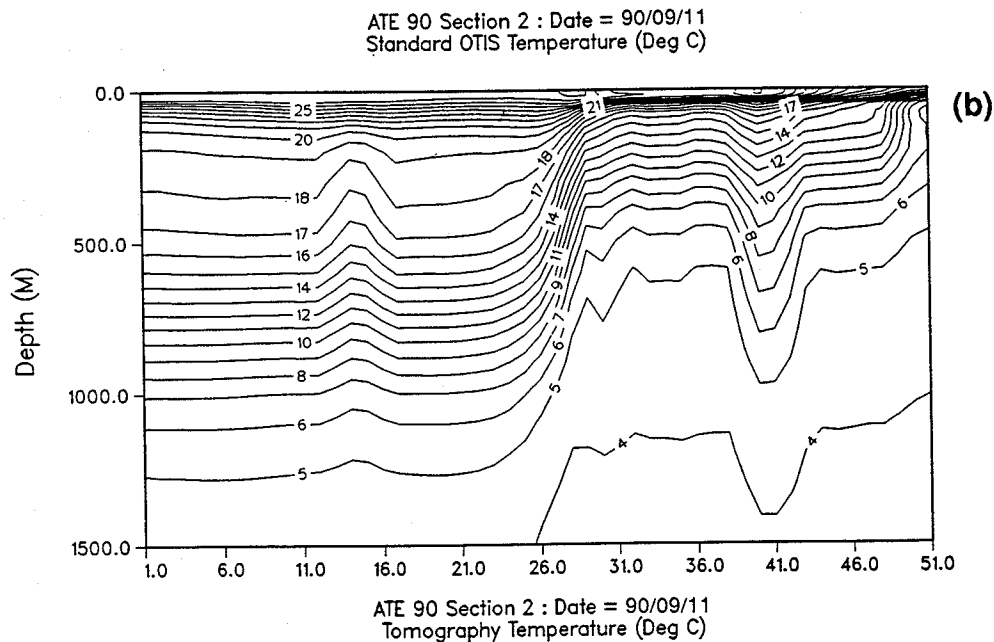
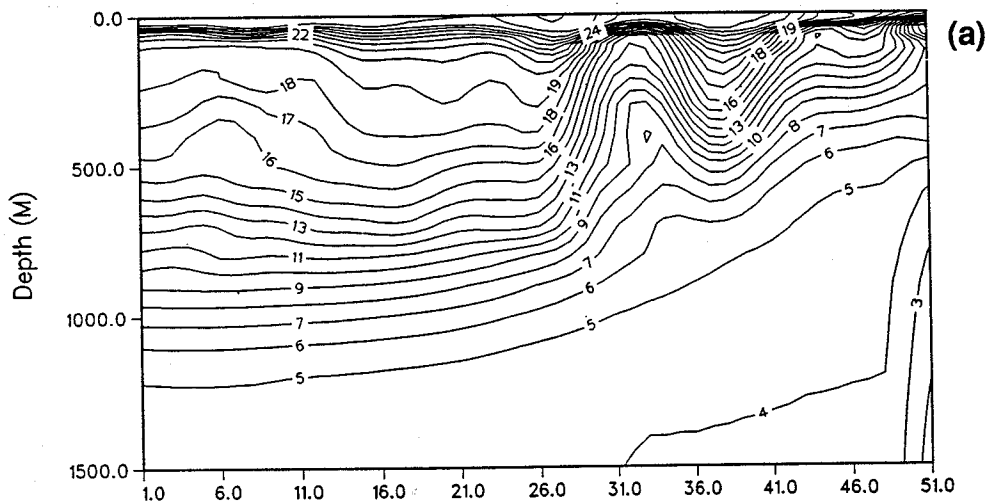


Figure 38. Temperature sections along path 1006 for 11 September. (a) AXBT data (using standard optimal interpolation); (b) OTIS output; (c) tomography output.

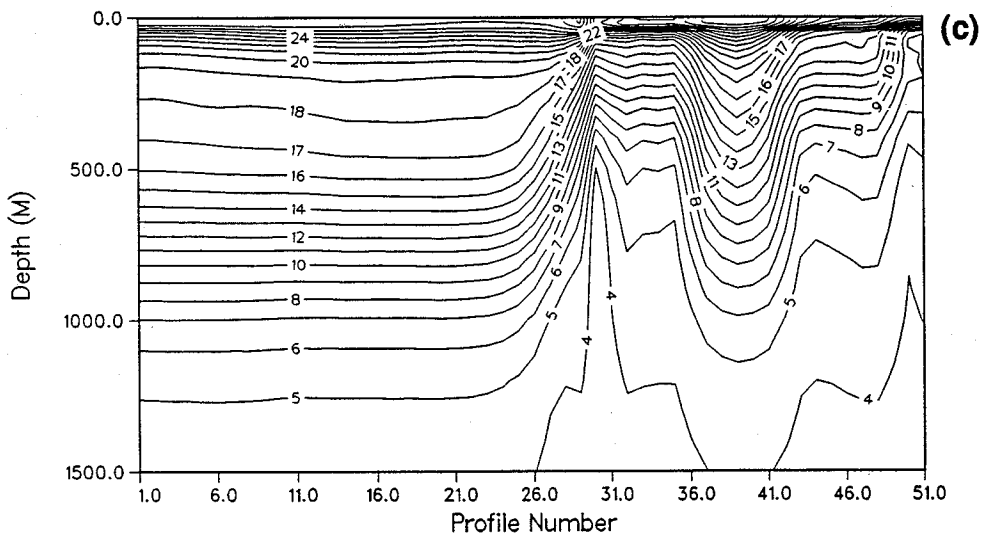
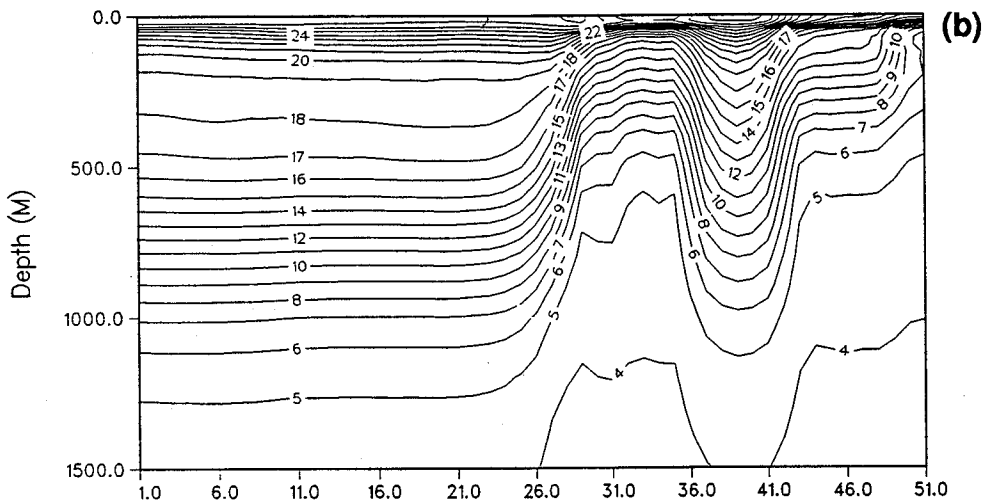
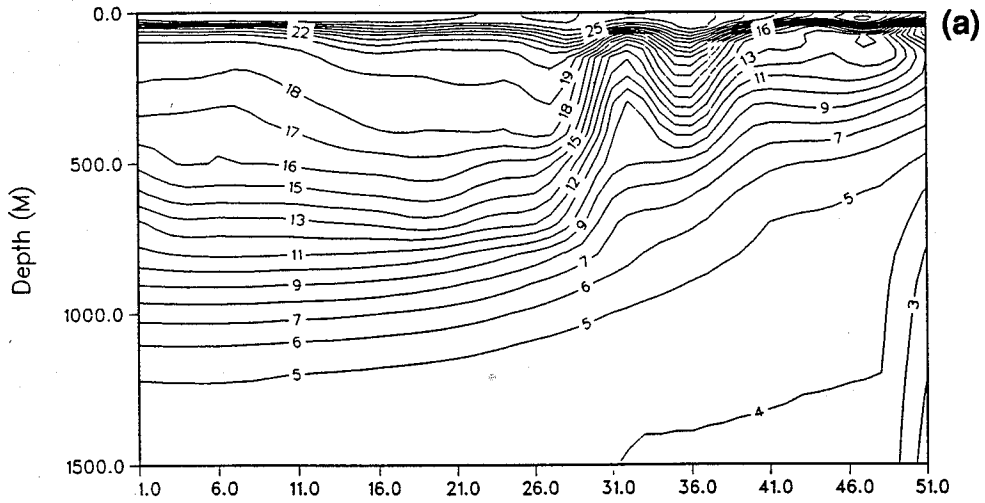
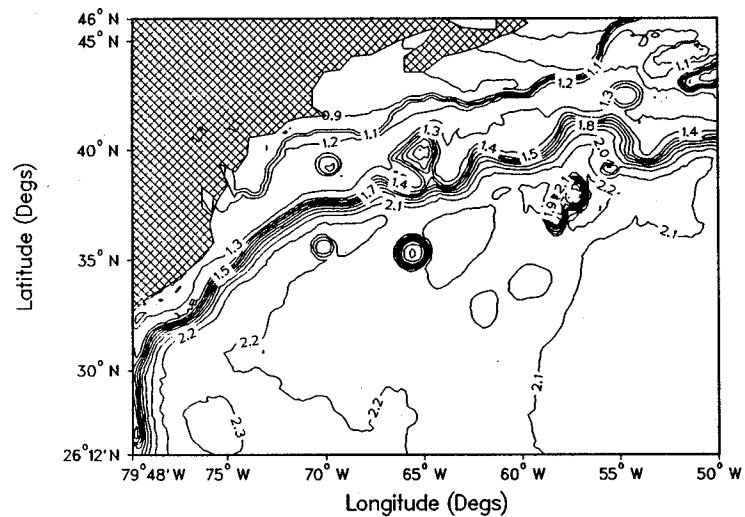


Figure 39. Temperature sections along path 1006 for 14 September. (a) AXBT data (using standard optimal interpolation); (b) OTIS output; (c) tomography output.

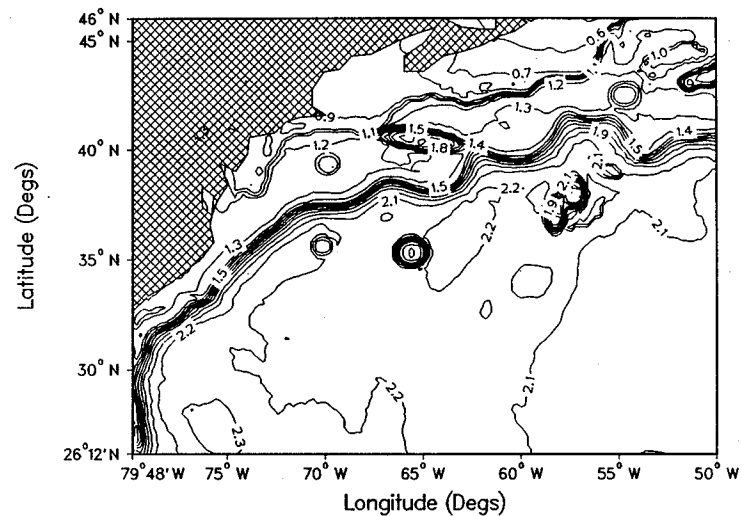
Dynamic Height (0/2000 Dbars) Date: 90/09/07

(a)



Dynamic Height (0/2000 Dbars) Date: 90/09/08

(b)



Dynamic Height (0/2000 Dbars) Date: 90/09/13

(c)

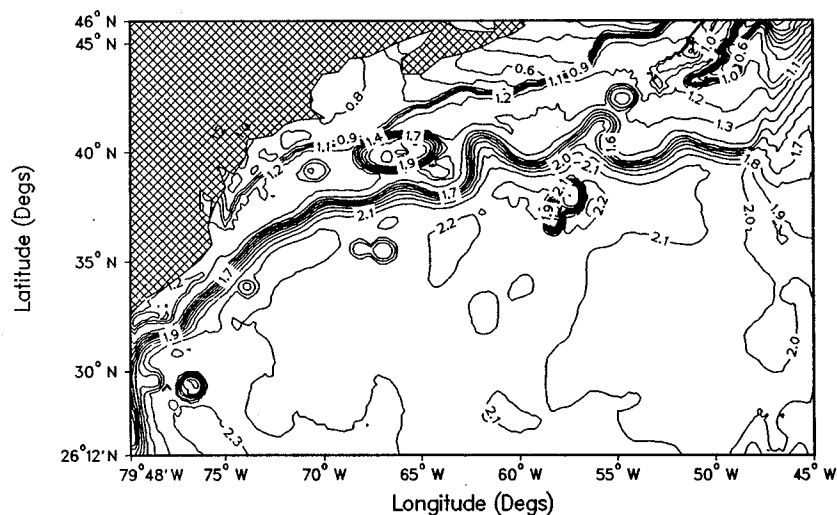


Figure 40. Surface topography maps derived from OTIS of the experimental area for (a) 7 September, (b) 8 September, (c) 13 September.

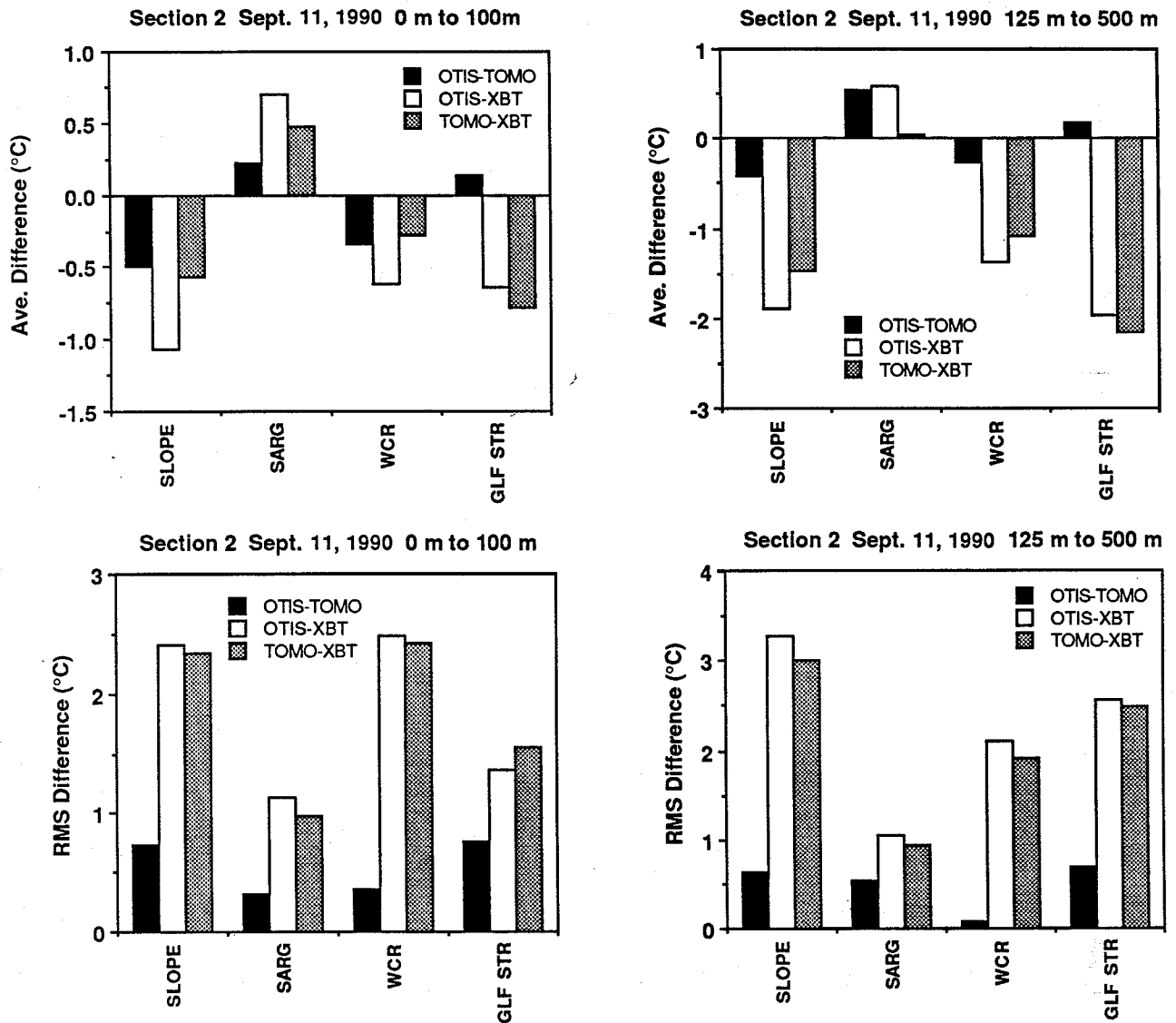


Figure 41. Average and rms differences between OTIS and tomography results, OTIS and AXBT results, and tomography and AXBT results, for each water mass in two depth intervals. For 11 September.

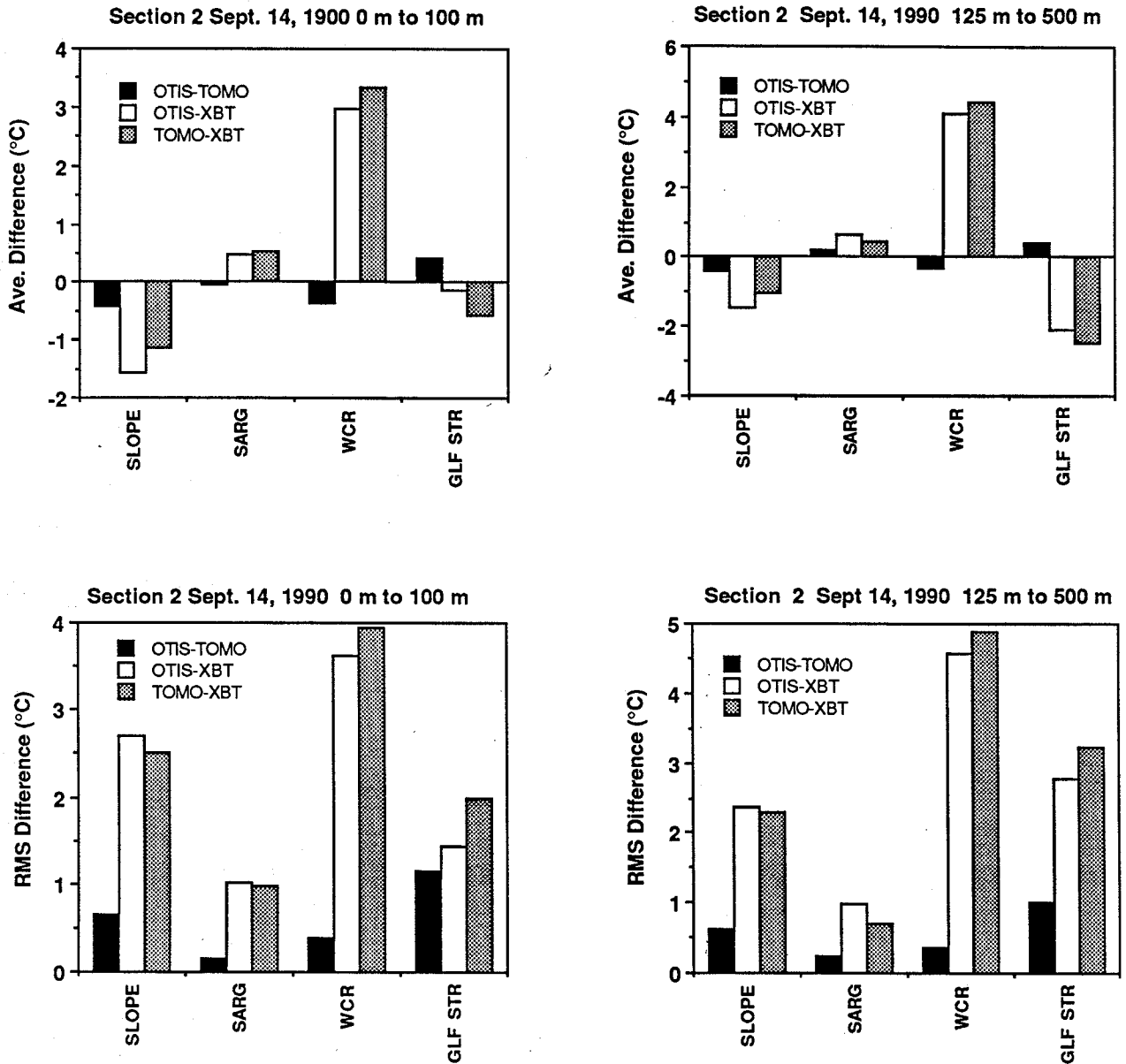


Figure 42. Average and rms differences between OTIS and tomography results, OTIS and AXBT results, and tomography and AXBT results, for each water mass in two depth intervals. For 14 September.

3.2 Comparisons with OOC Fronts

Daily 0000Z travel times were extracted from the filtered, tracked-path data sets for paths 1006 and 1015 to form a data subset for analysis. Perturbation travel times, δT , were formed by subtracting a reference travel time; for path 1006, the reference travel time was that measured on day 199 (when there were AXBT data); for path 1015, it was that measured on day 265. Using this data set, we calculated relative front positions, δR , using the ‘rule of thumb’ relationship

$$\delta R = -\delta T(s) \times (1 \text{ km}/0.005 \text{ s}) \text{ km}.$$

Spiesberger (1989) determined that each 5 ms change in acoustic travel time adheres closely to a 1 km spatial translation of the Gulf Stream along acoustic paths that are normal to the front. We have confirmed this by tracing rays through an OTIS field with a simple front, and translating the front a known amount.

The composite frontal analyses prepared by OOC four times each week and used as input to OTIS were used to tabulate along-slice positions of the north wall of the Gulf Stream. The positions derived from these OOC analyses were normalized to fit the zero-based reference frame of the acoustically derived spatial data. IR satellite imagery (when cloud free) was also reviewed to verify the OOC frontal analyses. Finally, the positions derived from acoustic travel times were compared with the tabulated positions derived from the OOC frontal analyses.

Figures 43 and 44 show the variation in the position of the north wall for paths 1006 and 1015, respectively, as calculated from acoustic travel time measurements and as derived from OOC subjective analyses. The figures are based on the average travel time for all tracked acoustic-ray arrivals along the respective source/receiver paths. Very similar figures are obtained if only the first arriving (fastest) ray is used. The AXBT front locations are also shown.

In Figures 43 and 44, time intervals are marked when warm and cold eddies and multiple Gulf Stream fronts due to meandering are present. The simple comparison between OOC Gulf Stream front positions and the acoustically derived front position makes sense only when there is a simple Gulf Stream front and no other features. The

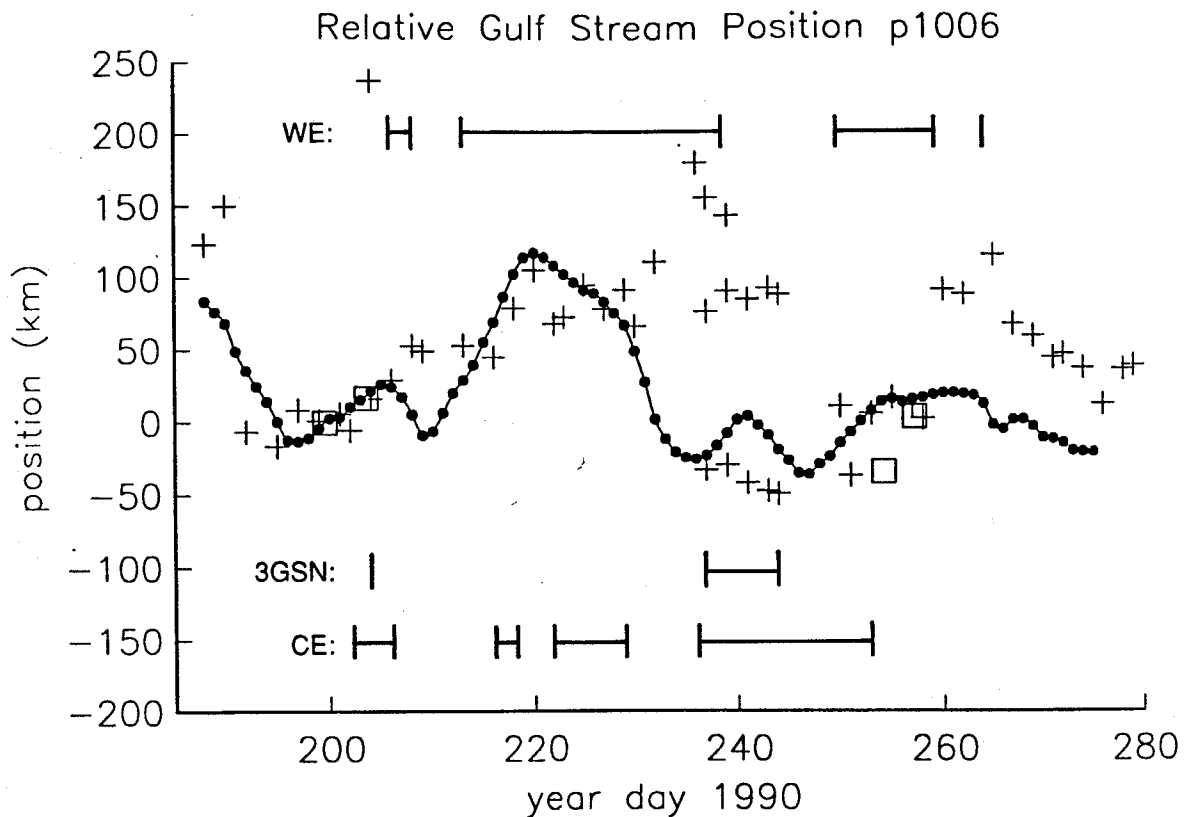


Figure 43. Relative front locations of Gulf Stream north wall along path 1006. The crosses show the estimates from OOC; the solid circles and line show the locations derived from the acoustic data using the rule of thumb that 5 ms corresponds to 1 km of movement. Times when cold eddies (CE), three Gulf Stream north-wall fronts (due to looping, 3GSN), and warm eddies (WE) were reported by OOC are marked. The frontal locations determined from the AXBT data are shown as squares.

marked intervals are an indicator of when not to make a direct comparison. For path 1006, only the beginning and end of the record have a simple Gulf Stream; during most of the record, a warm- and cold-core ring are present. The latter is notoriously difficult to detect on IR images and probably was present longer than indicated; it was not seen in either the July or September AXBT data. At the end of the record, when the OOC results indicate only the Gulf Stream is present, the tomographic estimate places the front roughly 50 km south of the OOC location. This may mean that the same or a different cold-core ring had wandered into the slice.

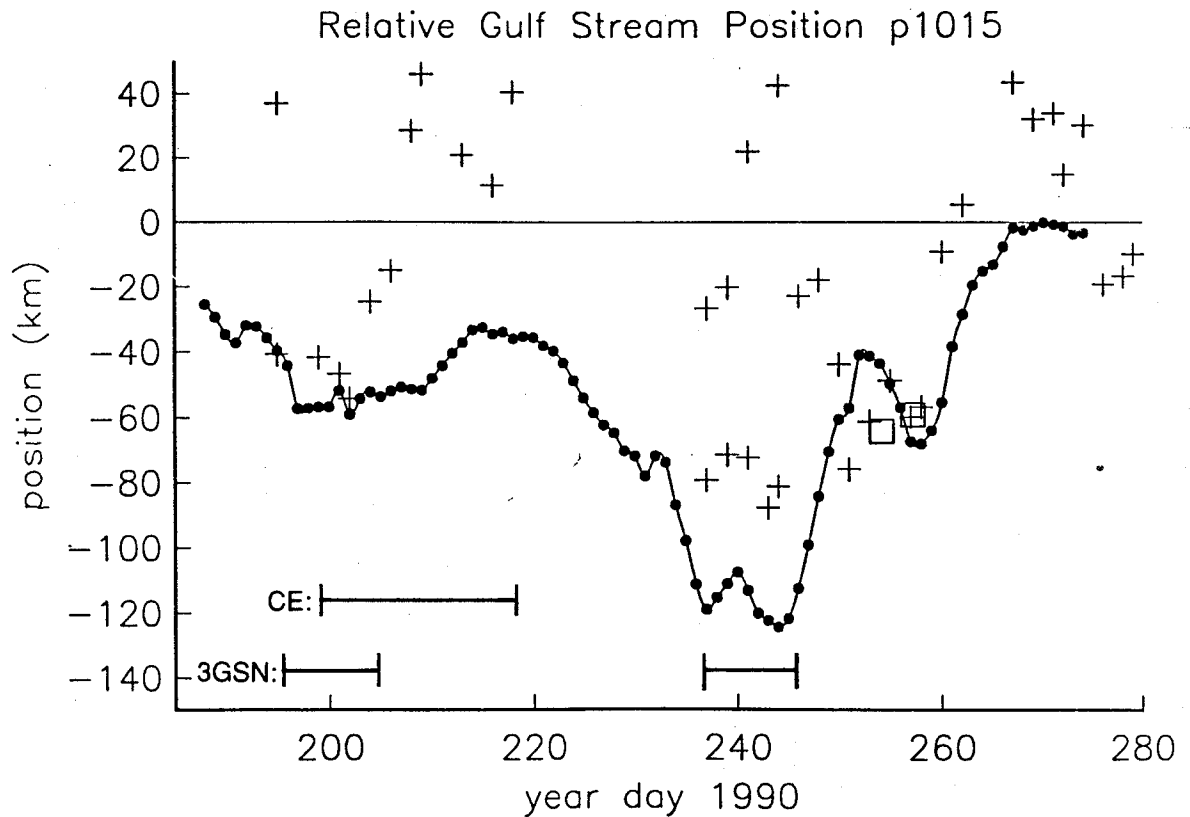


Figure 44. Relative Gulf Stream north wall front location along path 1015. As in Figure 43.

For path 1015, the interpretation is somewhat easier because the geometry excludes warm-core rings. The effect of the cold-core ring can be seen in the first half of the record. The acoustically derived front position is south of the OOC-derived one because more cold water is present in the slice. This effect must have been very large between days 220 and 236 because the OOC front estimate is off scale to the north. During this period, OOC did not report a cold eddy. This is an example of what the acoustic data can do: If OOC is sure of the Gulf Stream's position and there is a large discrepancy like this, OOC can then say that there is a cold-core ring along the slice. No cold eddies were reported during the latter part of the record from day 248 on, and the OOC, AXBT, and tomography front estimates agree reasonably well.

It is important to keep in mind the different nature of these data. The OOC fronts are based on IR imagery, the tomography results on acoustic averaging, and the AXBT

fronts on point measurements. It would be surprising if they agreed too closely! They can be rigorously compared only if the errors for each are accurately modeled, so that apples can be compared with apples and not oranges. Keep in mind also that ocean mapping is a four-dimensional problem and taking 2-D slices at an instant of time and ignoring the other two dimensions can lead to problems. For instance, because the travel time records are so smooth, one might be tempted to say that the OOC positions along the slice are too noisy. This would be incorrect, because there are many situations (see the sea surface temperature images in Figure 31 or the dynamic height fields in Figure 40) where the front and rings are so contorted that there can be instantaneous jumps in location along a slice. Consider a front that is nearly parallel to the slice in question. As the front is advected across the slice, there can be very large apparent frontal velocities in the slice direction, a simple artifact of geometry. One needs to look at the full 4-D picture.

The most direct comparison with our data is that in Figure 17, which shows the measured travel times and the travel times predicted by tracing rays through the OTIS field.

3.3 Comparisons with OTIS Fields

This section compares time series of vertical temperature sections derived along section 2 (path 1006) by OTIS and by acoustic tomography for 23 August to 16 September. Each vertical temperature section was subdivided according to water type (or specific mesoscale feature) and depth interval. The six different water types used are Sargasso Water, Slope Water, Shelf Water, Gulf Stream Front, and Warm- and Cold-Core Rings. The divisions between these water types may differ on the OTIS, AXBT, or tomography sections. However, each section was divided according to the water types found on the standard OTIS product. An example of these sections is shown in Figure 45, for the OTIS thermal section on 26 August. The vertical section passes through the edge of a cold-core ring in the Sargasso Water centered near profile 14 (22 km elapsed between profiles), but the section is classified as Sargasso Water because it is outside the core (inner $2/3$ radius) of the ring, within which it is modeled with solid body

rotation. Another region requiring explanation is the one with profiles 34, 35, and 36 marked as Gulf Stream and bounded on each side by Slope Water. This situation is caused by a meander of the Gulf Stream, which loops back into the plane of the vertical section and nearly connects with the warm-core ring. During the time series, the warm-core ring was captured, tenuously, by the Gulf Stream and was then classified as Gulf Stream. The ring later separated from the stream.

Each subsection is divided into four depth intervals: (1) 0 to 100 m, encompassing the surface mixed layer and the seasonal thermocline; (2) 125 to 500 m, spanning the thermostad (18° water) between the seasonal thermocline and the permanent thermocline in the Sargasso Water and encompassing the main thermocline in the Slope Water; (3) 600 to 1200 m, spanning the main thermocline in the Sargasso Water and below the thermocline in Slope Water; and (4) the deep water region from 1300 m to 5000 m.

The time series of the mean and rms daily difference between the standard OTIS temperature and the tomography temperature for each water type and depth interval are shown in Figures 46a through 46d. The tomographic temperature section is derived using the OTIS section as a first guess and, perhaps as a result, the two sections typically appear very similar. In the Sargasso Water, the mean difference increases to a maximum near 3 and 4 September at all depths, and then decreases to a minimum near 10 September. This difference corresponds to a general cooling of the Sargasso Water at all depths in the tomography section, as shown in the vertical sections and difference plots for 4 September in Figure 47. Temperatures in the two sections are nearly equal at the southern end of the transect, and the position and structure of the cold-core ring is basically unchanged. In the Sargasso Water, differences are smallest during periods when the sections pass near the center of the warm-core ring (north of the front) and greatest when the sections pass near the edge or outside the ring. This is clearly seen by comparing the OTIS vertical section for 4 September in Figure 47 with the OTIS sections for 31 August and 10 September in Figure 48. The dependence of the Sargasso Water structure in the tomography section on the presence of the warm-core ring in the Slope Water may or may not be true. This dependence might be explained by the cold-core ring south of the Gulf Stream front; this ring was never well observed, and it could very well have

influenced the travel time measurements. The correct thermal structure can only be determined by additional *in situ* observations; however, OTIS sets thermal structure in the Sargasso Water to the historical data base at positions far enough away from the front or rings, and therefore represents average conditions.

The plot of mean and rms difference versus time for Slope Water (Figure 46c) shows the rms difference peaking on 4 September in a manner similar to the mean and rms for Sargasso Water. Unlike for the Sargasso Water, however, the mean difference is generally small at all depths except during the first 2 days of the series and for 3 days after the peak in rms is reached. The larger differences occur because of a drop in the Slope Water temperature in the tomography section, either as a broad region of uplifted isotherms (as seen on 24 August in the region between the Gulf Stream front and the warm-core ring in Figure 49) or as a local upward spike in the isotherms (as seen on 7 September in Figure 50). In both cases, the resulting tomographic section is unrealistic: measured temperature profiles under Slope Water decrease to 3°C only at depths greater

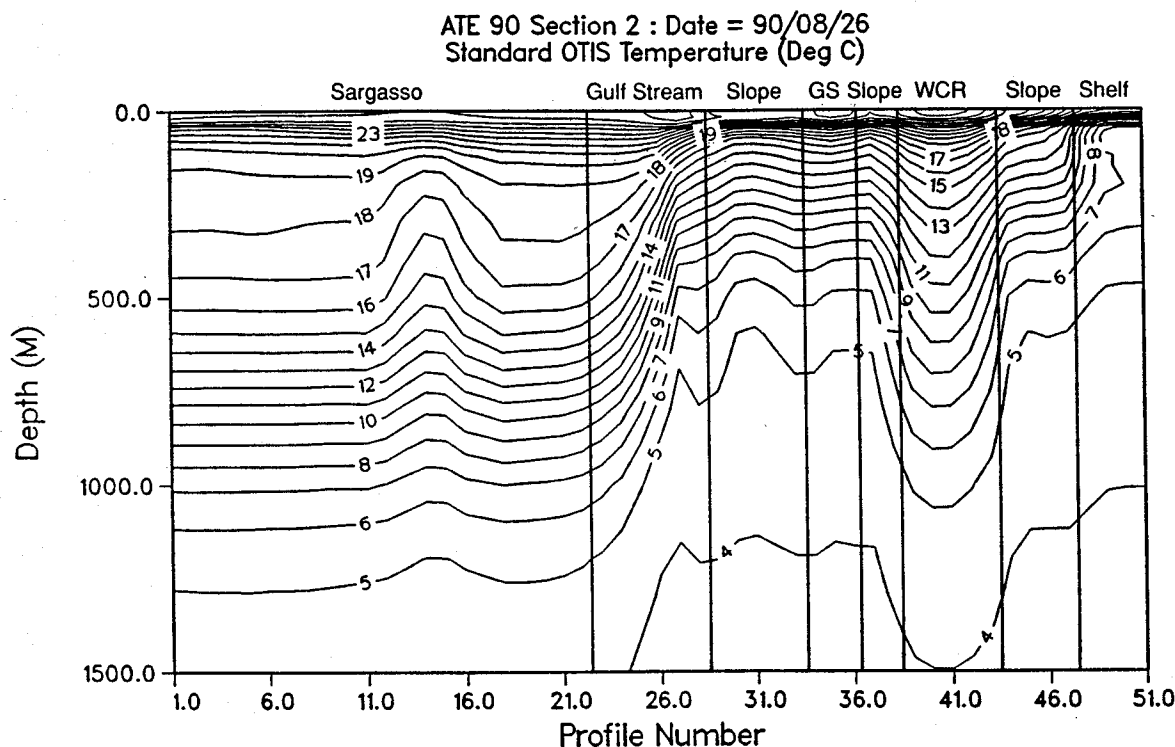


Figure 45. Temperature along slice 1006 (section 2) for 26 August (day 238). The various water masses are identified.

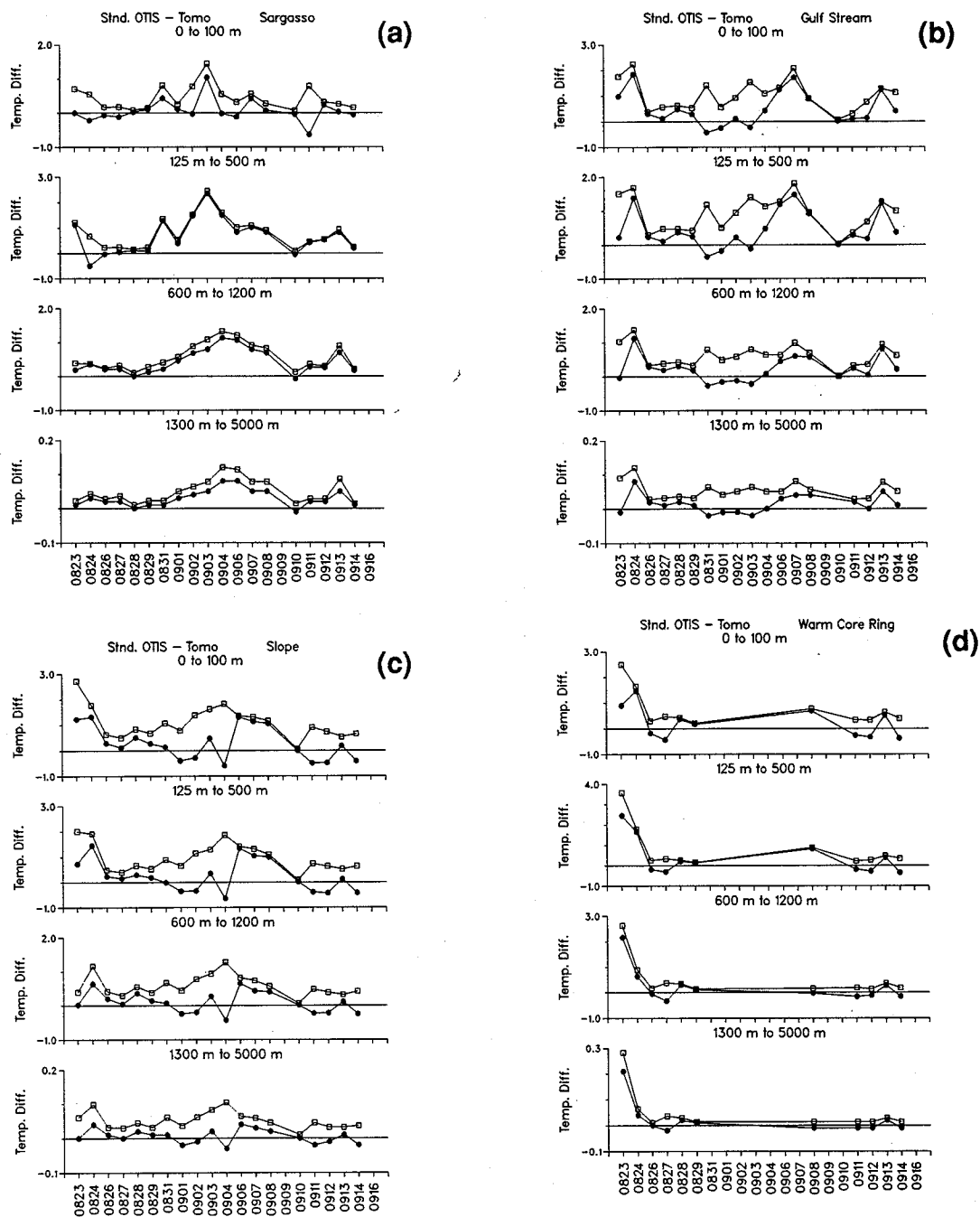
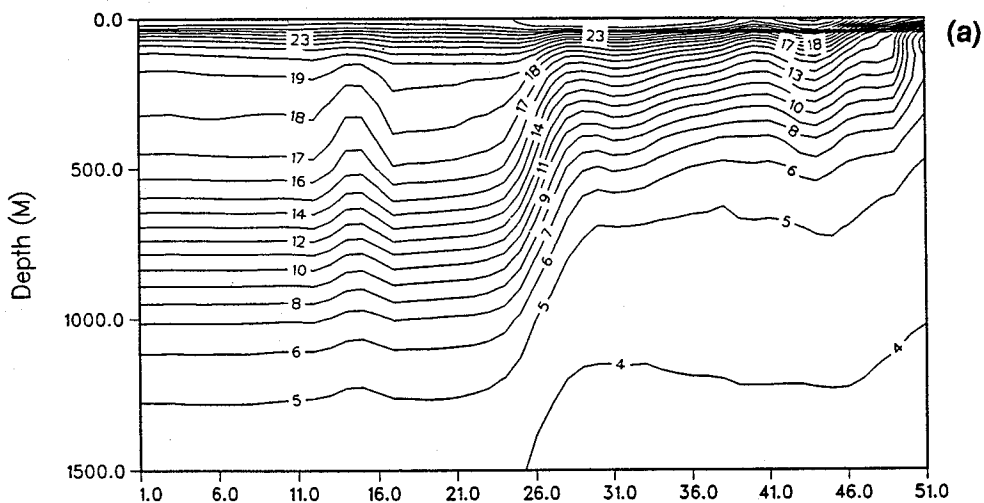
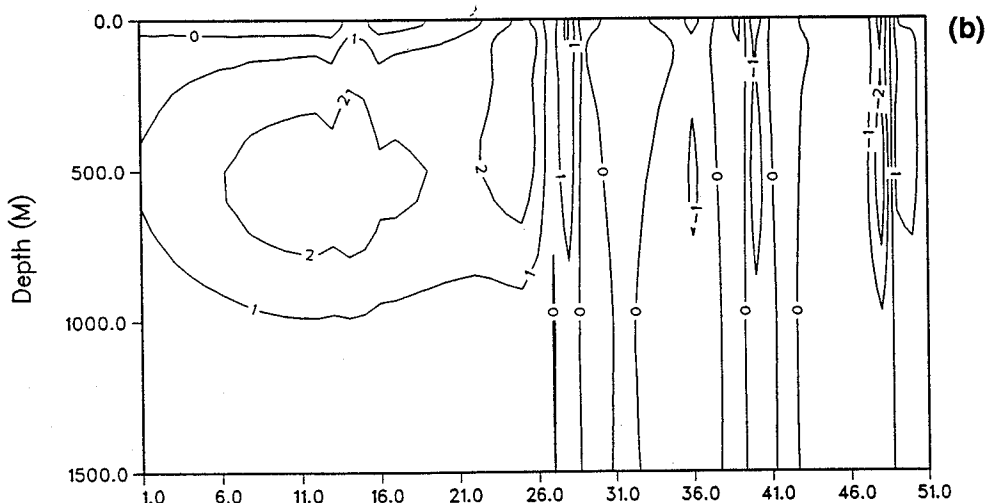


Figure 46. Daily rms difference between standard OTIS and tomography temperature as a function of depth for the different water masses: (a) Sargasso Sea, (b) Gulf Stream, (c) Slope, and (d) Warm-Core Ring.



ATE 90 Section 2 : Date = 90/09/04
otu - tom Temperature Difference (deg C)



ATE 90 Section 2 : Date = 90/09/04
Tomography Temperature (Deg C)

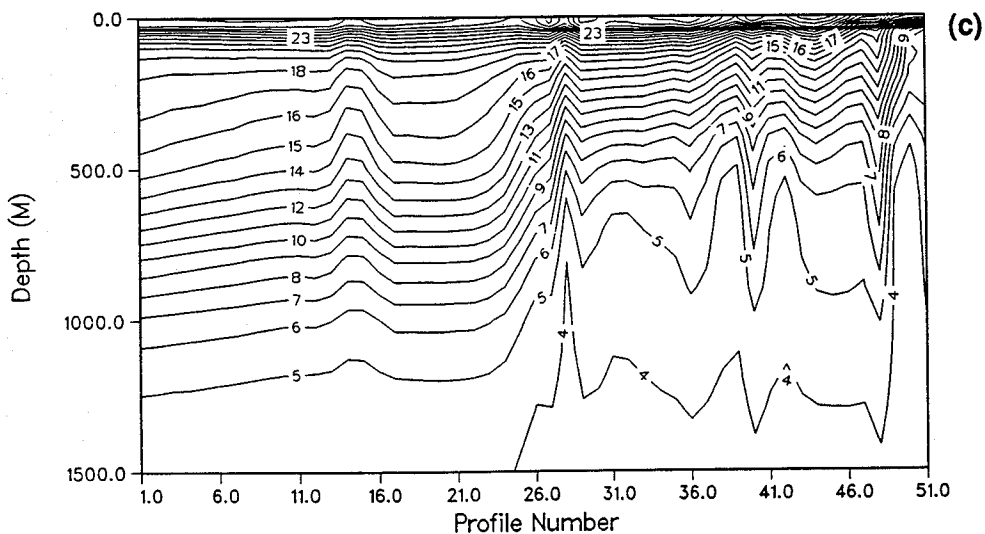


Figure 47. (a) Standard OTIS temperature on 4 September minus (c) tomography temperature = (b) the difference.

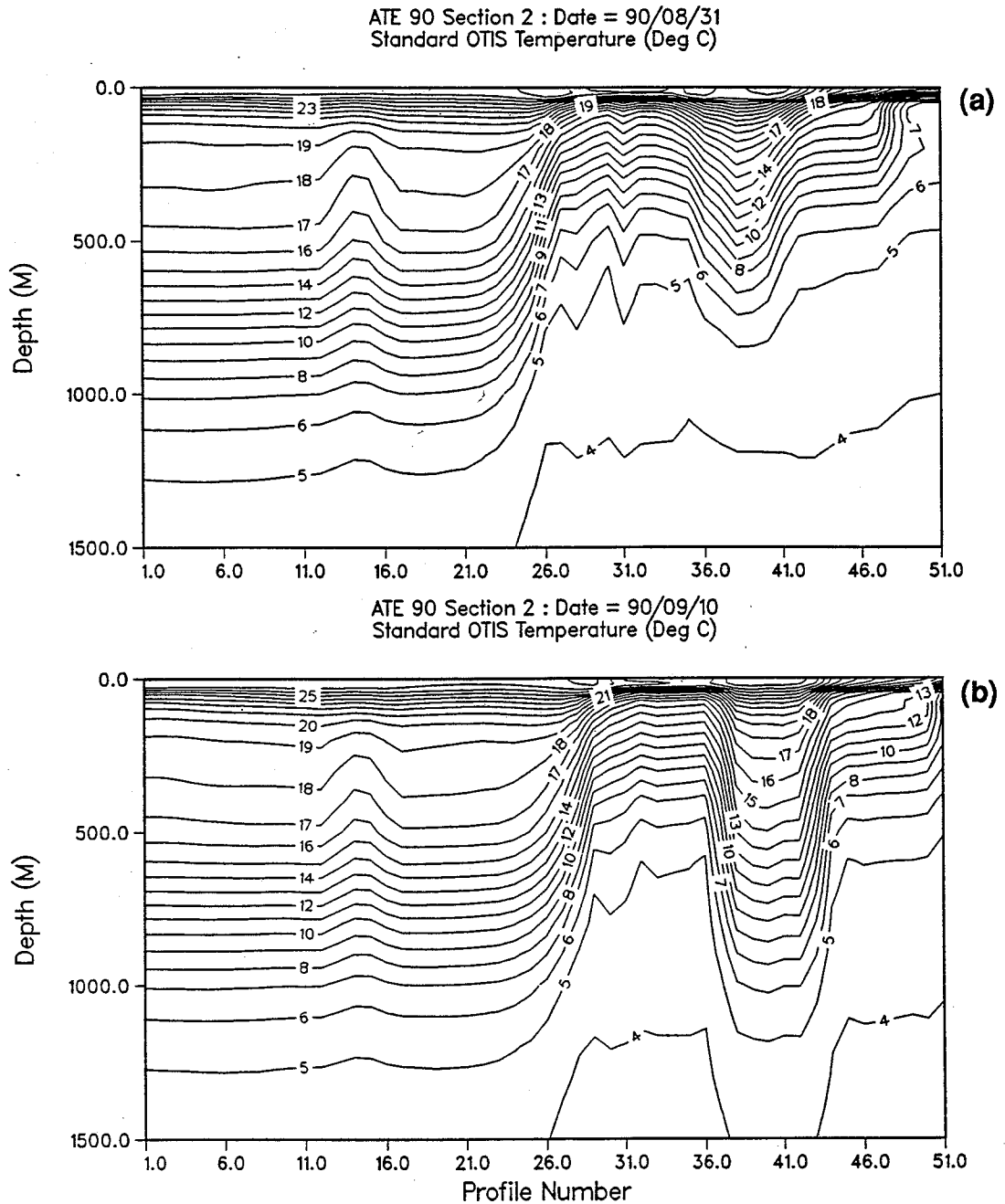


Figure 48. OTIS temperature section for (a) 31 August and (b) 10 September for slice 1006.

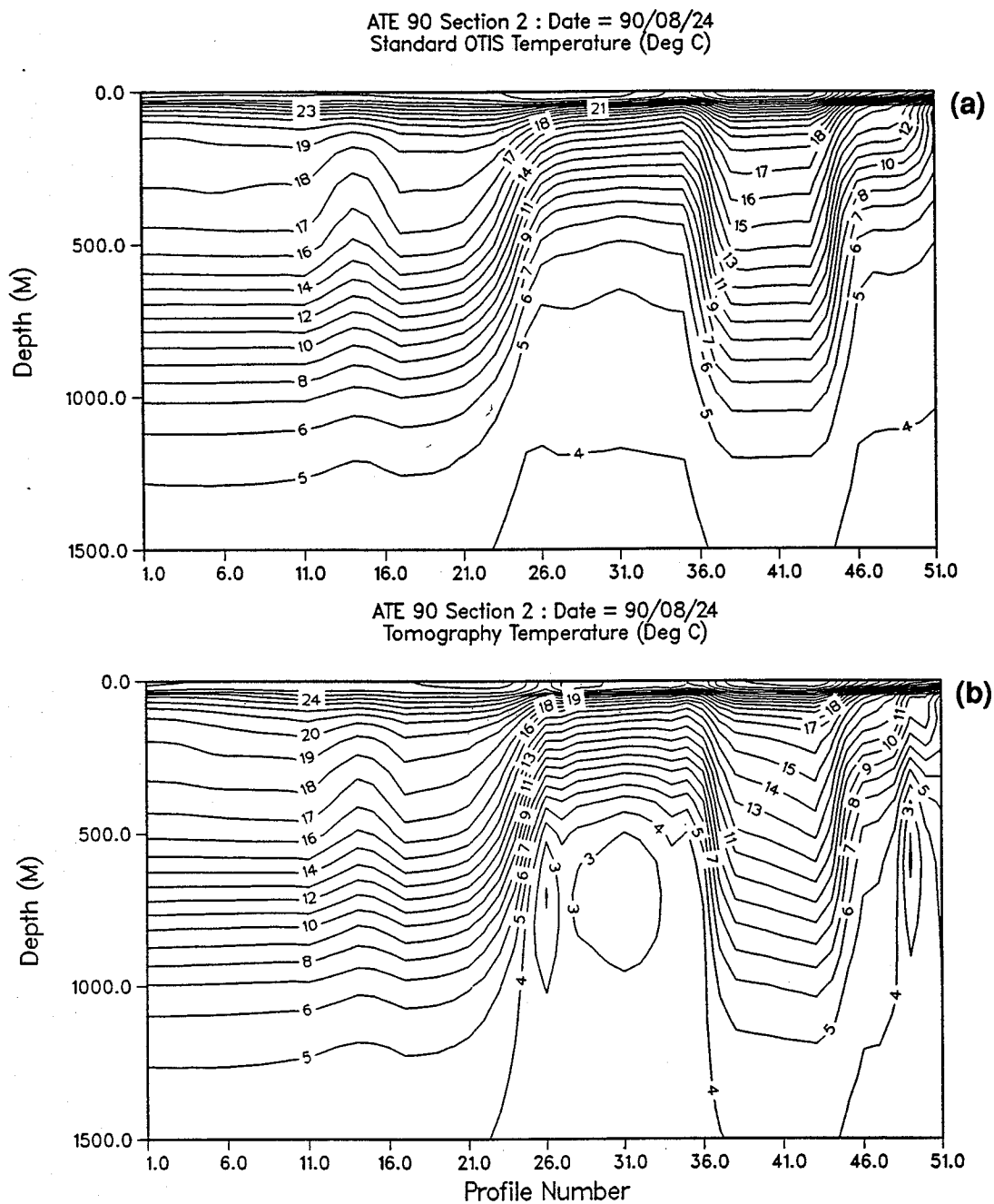


Figure 49. Temperature section for 24 August along slice 1006: (a) OTIS, (b) tomography.

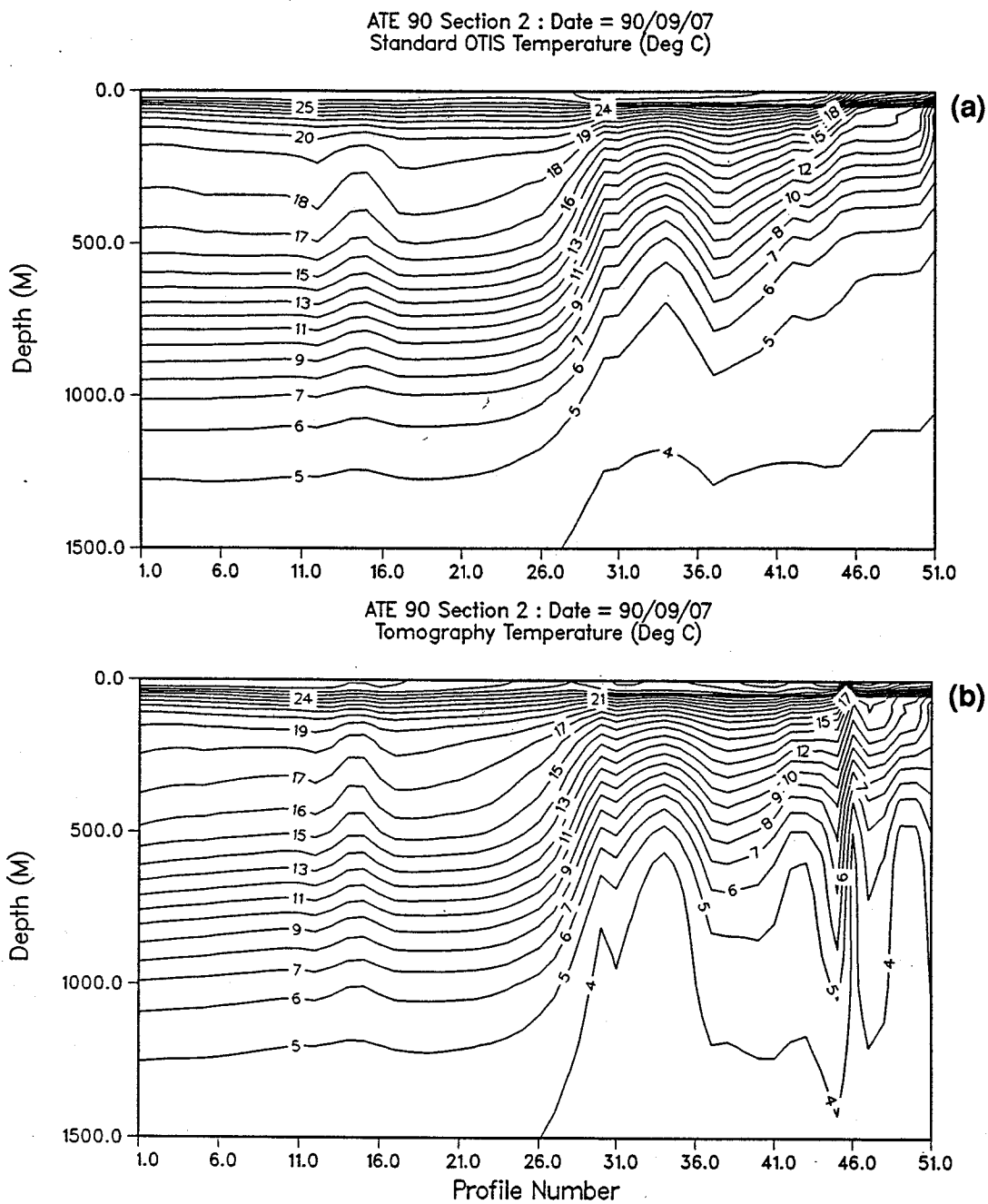


Figure 50. Temperature section for 7 September along slice 1006: (a) OTIS, (b) tomography.

than 2000 m, not at 750 m as shown in the tomography section, and a temperature minimum at 750 m is not seen in other measurements.

The time series plot of mean and rms differences for the Gulf Stream front (Figure 46b) is similar in character and magnitude to that for Slope Water. Larger differences are always positive, indicating colder tomography temperatures. In all cases, the position, frontal slope, and horizontal gradient of the front in the tomography sections are nearly identical to those in the OTIS sections (except for two cases). Differences occur as broad (order 100 km) depth changes in isotherms, not in lateral movement of the basic frontal structure. Most tomography sections also exhibit a sharp upward spike in the isotherms near the northern edge of the Gulf Stream front, as seen at profile 28 in Figure 47, profile 26 in Figure 49, and profile 30 in Figure 50. The manner in which this spiking occurs mimics, in exaggerated fashion, an error known to occur in OTIS 3.0 in its derivation of the thermal structure near the northern edge of the front.

The time series of mean and rms differences for the warm-core ring, Figure 46d, shows only small differences at all depths except on 23 and 24 August. From 31 August through 7 September, the ring was attached to the Gulf Stream and therefore not classified by OTIS as a ring. On 23 August, the tomographic thermal analysis modified the OTIS first-guess field by reducing the ring's radius from about 110 km to 75 km and also moved the center southward about 50 km. On later dates, the ring's size and position in the tomographic sections are nearly identical to those in the OTIS sections. The typical differences appear as weak and uniform cooling or warming of the ring.

As part of ATE90, tests were conducted to evaluate ways of assimilating tomographically derived data into the operational OTIS thermal analysis. The tomographically derived temperature sections can be assimilated by OTIS in two ways: as temperature measurements (profiles and surface observations) and as positions of front or eddy boundaries determined primarily from the high-radiance-gradient boundaries observed in satellite IR images. Both ways were tried during the experiment.

OTIS derives synthetic profiles using models of the Gulf Stream front and eddies that depend primarily on distance from the input front and eddy boundary positions. The

synthetic profiles are derived at enough positions throughout the analysis regions to resolve all modeled mesoscale features sufficiently. Once computed, the synthetic profiles are combined with observed temperature measurements to produce a gridded 3-D thermal field by optimal interpolation.

The position of the north wall of the Gulf Stream was estimated daily from the temperature sections produced by the acoustic tomography analysis. The north wall is defined for this purpose as the position where the 15°C isotherm intersects the 200 m depth level. This position was sent each day to OOC at the Naval Oceanographic Office, where it was combined with other data (primarily IR images) to produce frontal position maps. As part of its operational duties, OOC normally prepares maps of front and eddy boundaries on Monday, Wednesday, Friday, and Saturday. These maps are sent to the Fleet Numerical Oceanography Center, where they are used in the OTIS runs for 0000Z on Tuesday, Thursday, Saturday, and Sunday. OTIS analyses run on other days use the front and eddy maps prepared 2 days earlier, but use all measured thermal data available up to the analysis time. As a part of this experiment, OOC prepared, at their usual times, two separate frontal analyses, one done in the usual fashion and another in which the standard product was altered to match the tomographically estimated front positions.

Two OTIS runs were made daily at FNOC. The standard run used no tomographically generated product. The other used both (a) the frontal positions altered by tomography and supplied to FNOC by OOC and (b) tomographically produced temperature profiles from section 2 (path 1006).

Problems with this scheme for assimilation of tomography data were encountered. Most serious were the unwarranted shifts in frontal location when preparing the frontal location maps. The OTIS temperature sections prepared without tomography data and the tomography temperature sections were often similar, but the front positions derived from the tomography data often differed considerably from those used in preparing the OTIS section. (This may be due to a software error in the program that encoded the front locations before they were sent to OOC. This bug was discovered on 4 September.) As a result, the OTIS analysis prepared with tomography data often differed considerably

from both the standard OTIS analysis and the tomographic section. The front positions determined tomographically are for 200 m and must be converted to a surface position before being combined with the surface frontal positions derived from IR imagery; this was not done. An algorithm for performing this conversion does exist, but it is based on average observed relationships and does not take into account stream curvature or the angle between the stream axis and the section direction. A more reliable and accurate algorithm for performing this conversion must be devised before tomographically derived frontal data can be properly assimilated into OTIS.

Cumulative statistics on differences between the tomographic temperature profiles and the profiles derived by OTIS have been computed using all daily analyses for the period 22 August to 15 September. For each tomography temperature profile produced during this period, three corresponding estimates were produced: the climatological profile for that position and time of year, computed from the Generalized Digital Environmental Model (GDEM); a profile produced by OTIS given only the time of year and the front and eddy map (using the front and eddy feature models); and the OTIS analysis produced using the tomography profiles and the front map altered by the tomography data.

The mean (bias) and rms difference between the tomography profiles and each of the three corresponding estimates are shown plotted versus depth in Figure 51. The tomography profiles are most similar to the OTIS analysis and least similar to climatology. As expected, addition of tomography data to OTIS tends to make the OTIS result more similar to the tomography data than if the tomography data had not been added and assimilated. Of course, adding the tomography data to OTIS is useful only when these data are more representative of the true ocean structure than OTIS without tomographic data.

A quantitative measure of the "value added" by the acoustic travel time data to the OTIS sections is given by the percent reduction in error variance:

$$\% \text{ reduction} = \frac{E_{\text{OTIS}} - E_{\text{OTIS+TOMO}}}{E_{\text{OTIS}}} \times 100,$$

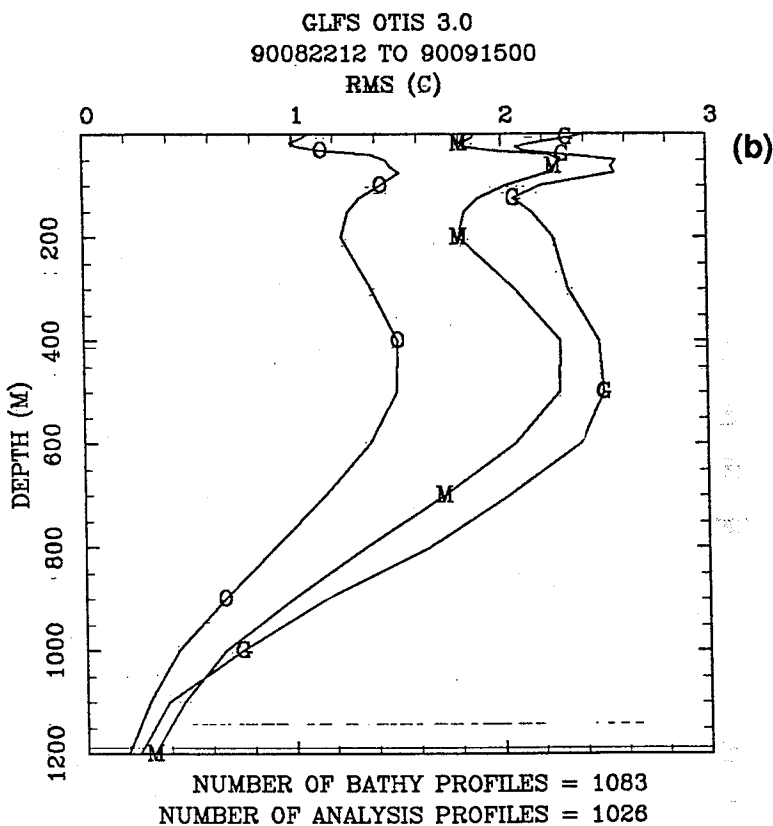
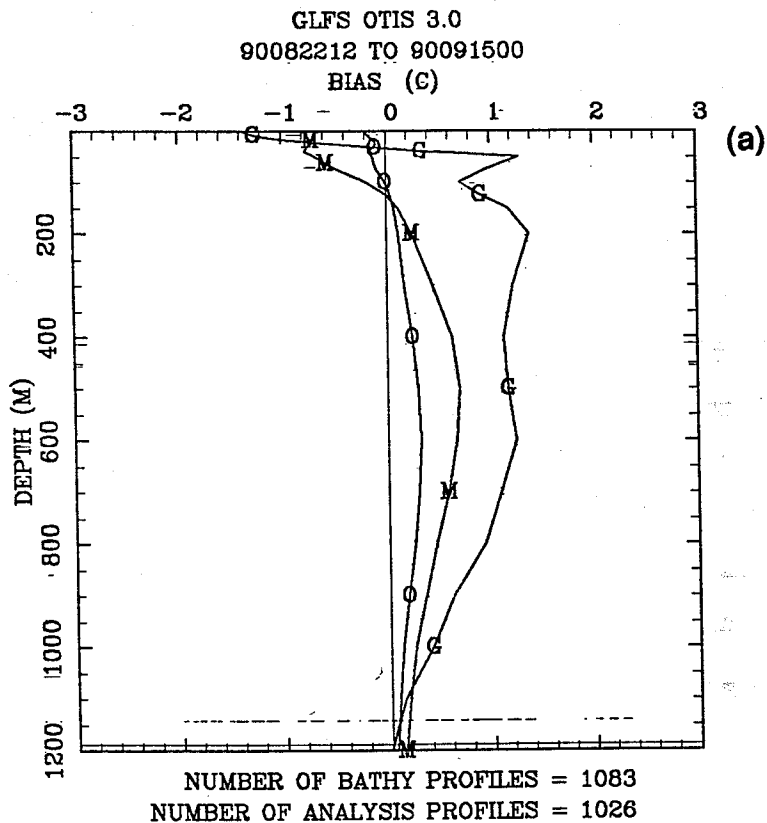


Figure 51. (a) Mean and (b) rms difference between tomography results and OTIS results (O), front and eddy models (M), and GDEM predictions (G).

where $E_{\text{OTIS+TOMO}}$ and E_{OTIS} are the temperature (or sound speed) errors with and without tomography data, respectively, averaged over the slice. This quantity is bounded by 0 (the data carry no additional information) and 100% (the data fully resolve the field). For this experiment, the reduction was typically 20% (Figure 52).

3.4 Acoustic Comparisons

The most direct acoustic comparisons are between the measured arrival patterns and those predicted using the OTIS fields (Figure 16). Future work in source detection and localization, the primary Navy concern, will most likely involve some type of matched-field processing. In this process, above some SNR threshold, it is acoustic phase that is most important. Thus, comparison of travel times (as in Figure 16) bears directly on the matched-field problem. Inversion of the tomographic data changes the ocean so that it is consistent with the measured travel times within the error bars.

As mentioned above, the SNR must be above a certain level to permit detection, let alone localization. Thus it is relevant to determine the effect of the tomography data on calculation of transmission loss (TL). Because there are no measured data on TL , we can only look at the TL calculated in an OTIS field (for example, 31 August along path 1006) and the TL calculated in the corresponding OTIS + tomography field (Figures 53 and 54, respectively). Shown in the figures are the predicted TL for a source at 122 m depth as a function of range and depth. The acoustic frequency was 25 Hz. (This and subsequent figures are courtesy of Bruce Williams, NOSC.) The usual convergence zone pattern is evident. The TL differences are more easily seen in Figure 55. The black striped areas show where TL differences are between 8 and 100 dB, associated with shifts in convergence zones of about 10 km.

3.5 SURTASS Data

From 16 July to 22 July the SURTASS ship USNS *Bold* towed a horizontal array on a northeast course north of the Gulf Stream to provide additional data coverage (see Figure 56). The array was towed at a depth near the sound channel axis and a velocity of

2 knots. As mentioned in section 2.1.2, data were recorded with a 386-AT system similar to those used at shore listening stations. Some processing was done onboard ship, but further signal processing and correction were done following the cruise.

Ship position was tracked with LORAN, Motorola Eagle GPS, and P-Code GPS receivers. A Kinometrics GPS receiver with a rubidium oscillator was used as a time base. Array position was monitored with depth and direction sensors. Automatic logging of P-Code data failed early in the experiment due to failure of a commercial circuit board used to convert the data to an RS-232 format. Subsequent logging was done manually at 20 minute intervals (at times of signal reception). The estimated error for array position is on the order of 50 m, or equivalently 30 ms in travel time.

Figure 57 is a single reception from year day 197. Doppler and beam processing were especially critical for these data since the array was under way and was constantly changing its orientation. Average Doppler shift was -1.8 knots, and the beam angle varied between 100° and 150° . Typical maximum SNR for the receptions was 30 dB. Figure 57 illustrates the high amplitude axial arrivals common to the SURTASS arrival patterns. Also note the pronounced axial signal cut-off to the noise level at a relative travel time of 19.5 s in this figure. A trailing bottom bounce lags the axial arrivals and is common to most receptions. Steeper arrivals, like the fixed-station receptions, are only trackable as groups and not as individuals. Peaks with an amplitude above the noise level are displayed in the following figures rather than the entire arrival trace.

Figure 58 is a plot of the entire sequence of receptions vs. transmission time. Each short segment corresponds to a complete reception similar to that displayed in Figure 57. Gaps during year days 199 and 201 are due to receiver malfunctions. The 300 s difference in travel time between the first and last reception is a result of a source to receiver range increase of nearly 500 km over the 7 day period. Prior to studying the arrival patterns, this range-dependent portion of travel time must be subtracted from the arrival sequence. Because the ship is moving continuously, roughly paralleling the front, the horizontal axis roughly corresponds to distance along the front (see Figure 56). The

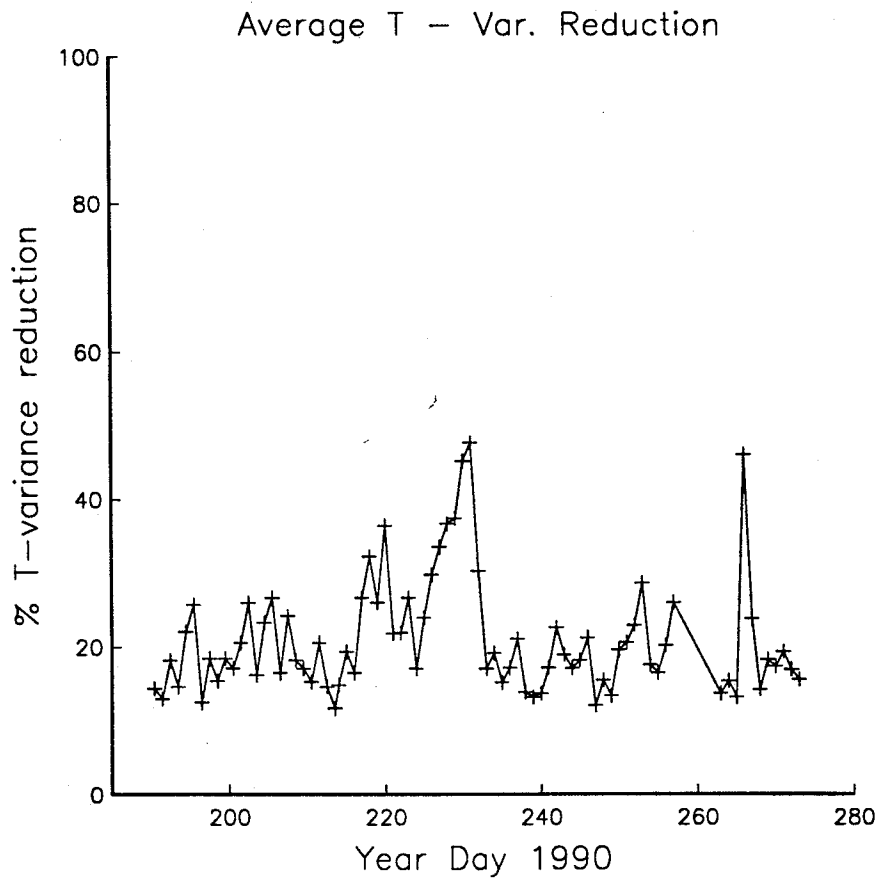


Figure 52. Percent reduction in temperature variance averaged along the slice as a function of time. A value of 100% would mean the travel-time data resolved the field perfectly; a value of 0 would mean the travel-time data made no contribution.

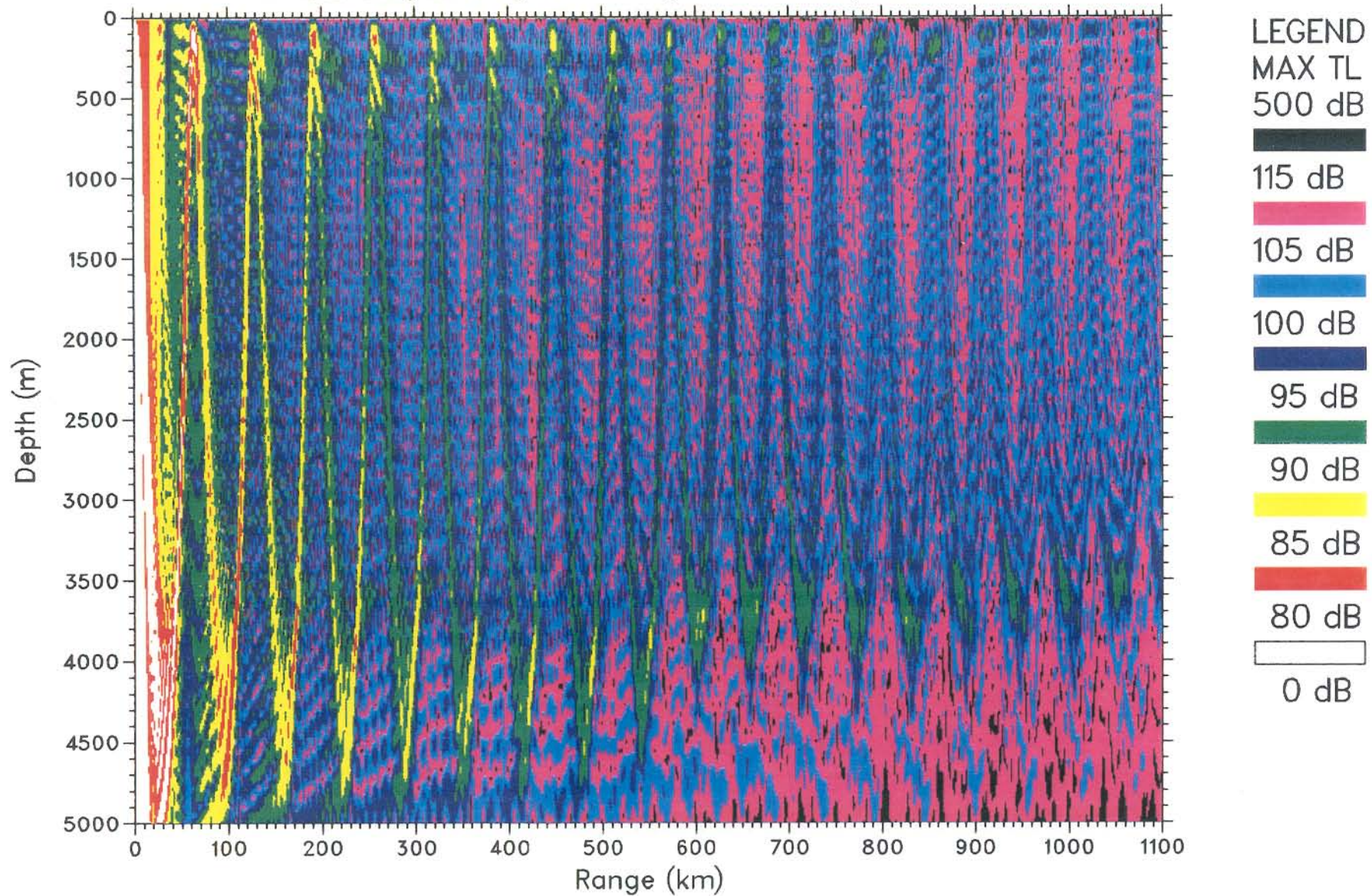


Figure 53. Transmission loss along path 1006 calculated using the sound speed field derived from OTIS.

PE 3.0, 25 Hz, S:121.9m, Inverted FNOC Data, YD-243

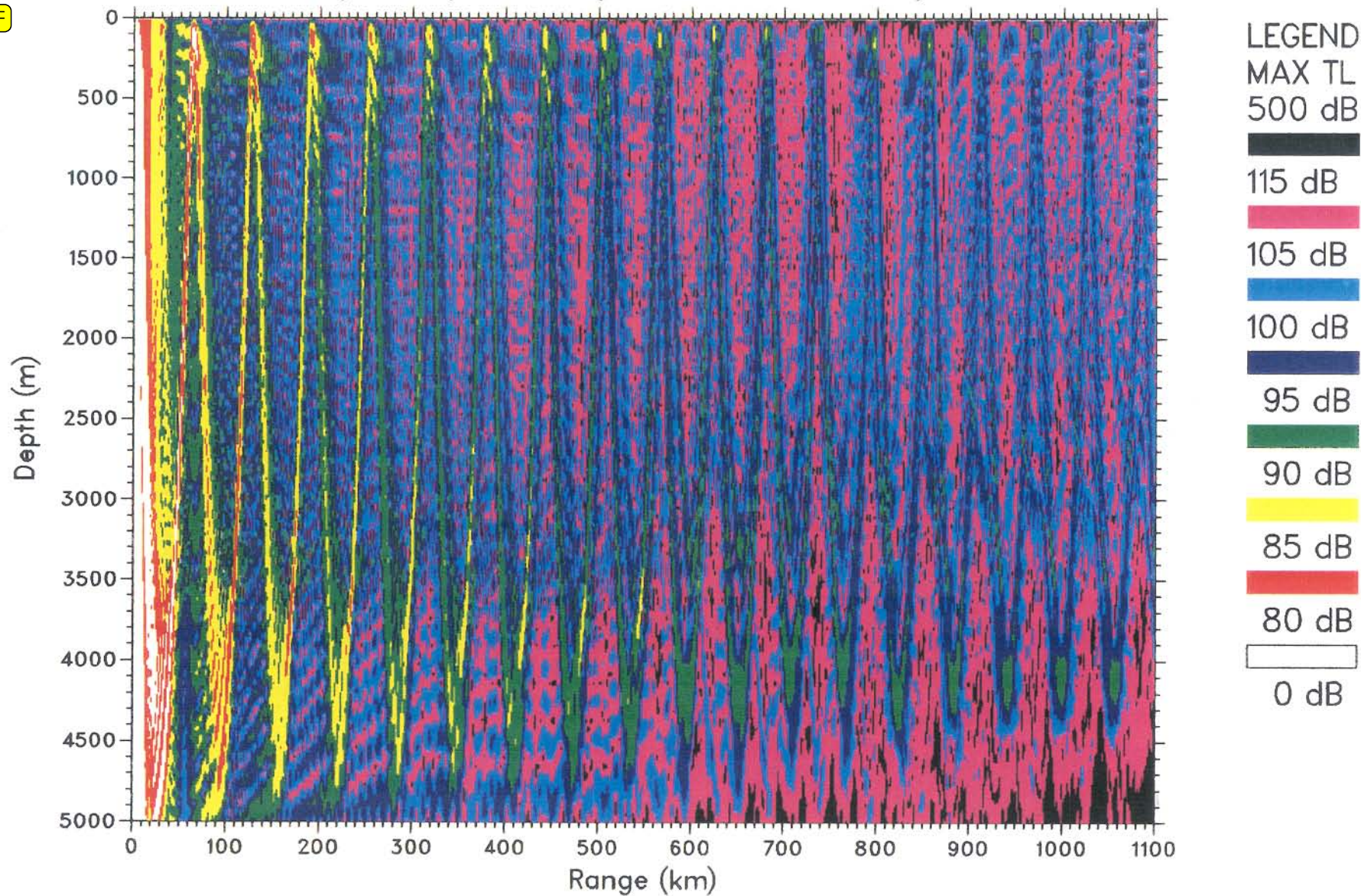


Figure 54. Transmission loss along path 1006 calculated using the sound speed field incorporating tomography data.

PE 3.0, 25 Hz, S:121.9m, ABS(Diff) FNOC Data, YD-243

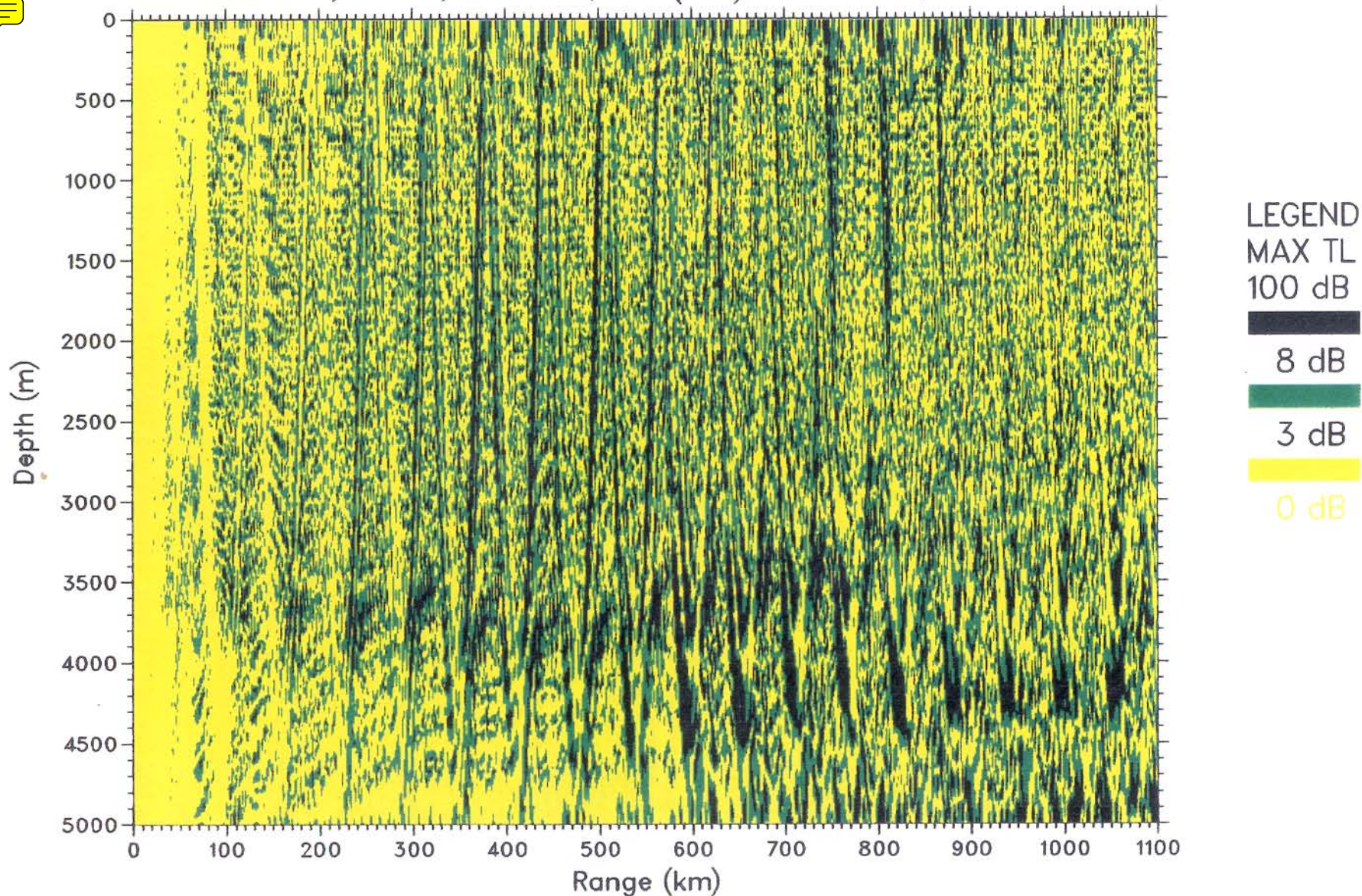


Figure 55. Difference in transmission losses calculated from OTIS results (Figure 53) and from tomography results (Figure 54) as a function of range and depth for a source at 122 m.



15

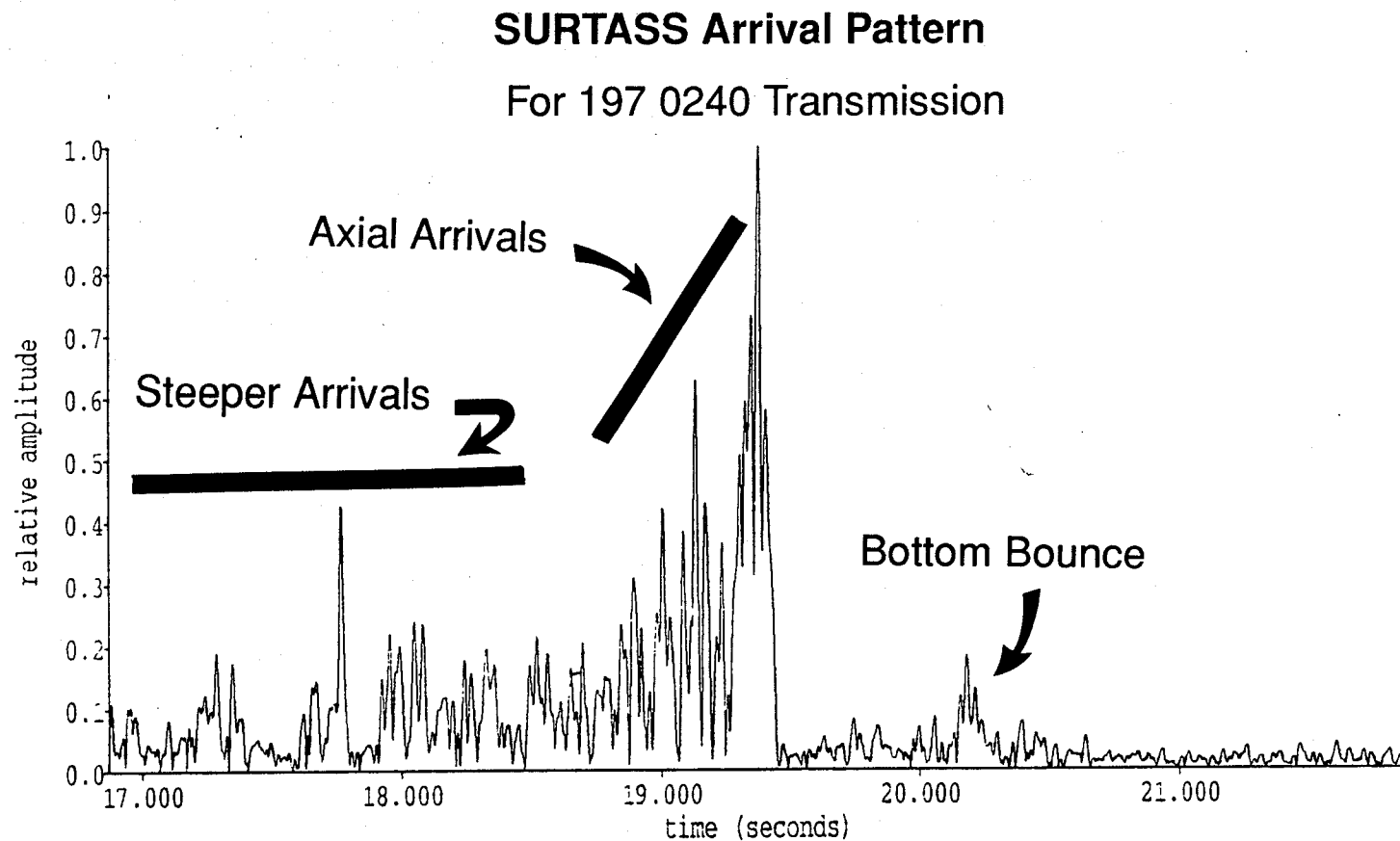


Figure 57. Typical reception during day 197. Steep arrivals are noticeable between 17 s and 18.5 s; axial arrivals at about 19 s. A later arriving bottom bounce trails the axial arrivals.

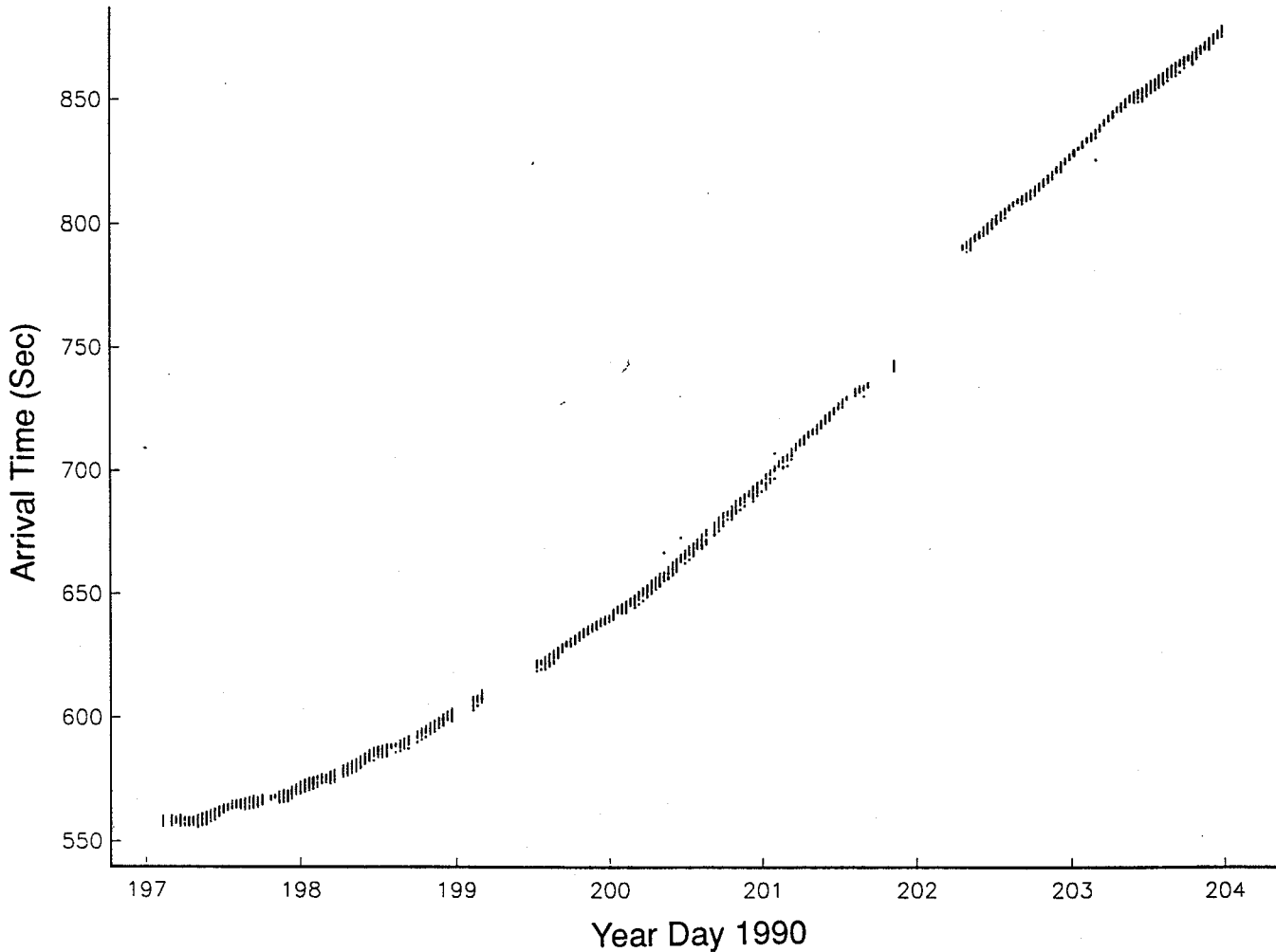
SURTASS Arrivals Uncorrected for Ship Position

Figure 58. Plot of all arrivals. Each short segment is the recorded arrival pattern. The 300 s travel time difference during the 7 day period is due to increasing range from the source. The jump in arrival time during day 202 is from a sudden change in ship's course. The range-dependent portion of travel time must be subtracted in order to study the arrival patterns.

approximately hyperbolic shape to the plot can be explained if one goes back to Figure 56. The ship track (bold line) and rays form an approximate right triangle. The resulting travel time for this geometry is hyperbolic:

$$T_0^2 = T^2 - X^2/C^2,$$

where

T_0 is travel time to ship on day 197

T is travel time to the array

X is distance from the ship's original position on day 197

C is the average sound speed between source and receiver.

The offset in the curve at day 202.3 is due to a larger than normal range increase during the time gap.

The arrival peaks, after subtracting the range-dependent portion of travel time, are displayed in Figure 59. In this figure pixel darkness is representative of amplitude. A constant sound speed of 1492 m/s was used for the entire set of arrivals. This velocity was used to make axial events nearly flat. Clusters of high amplitude events around 1 s are axial arrivals—groups of steeper arrivals are apparent between -3 s and 0 s. Lower amplitude bottom bounce events are seen at about 2 s. Much of the high frequency jitter is probably not due to signal from the Gulf Stream but rather to array position error. If one tracks a continuous event, such as the axial cut-off, and assumes the time constant for a Gulf Stream signal is greater than the time between receptions, much of this jitter can be removed by smoothing this trackable event over some finite window.

Figure 60 is the result of this smoothing. A running average of five axial cut-off events was used in this smoothing operation. This corresponds to assuming the Gulf Stream signal varies smoothly over a 3.3 hour period and a ~10 km distance. Six or seven arrival groups can be tracked from year day 197 to about day 201. The nearly hyperbolic trajectory of these events is a result of these rays sampling shallower, higher-sound-speed water. The reference sound speed of 1492 m/s has corrected events near 0 s

but has “over corrected” events below 0 s. Continued work determining depth-dependent average sound speeds from these deviations from horizontal is being pursued. Tracking the arrival patterns is rather difficult across the discontinuity at day 198.6 and particularly across the gap at day 199. To aid in this tracking, arrival pattern predictions were calculated along paths coinciding with FNOC slices.

Figure 61 displays the three ray predictions spliced into the data in their appropriate day locations. The closest position and depth for the SURTASS array was projected onto the FNOC slice in order to calculate the eigenrays and associated travel times. Shifts required for best alignment with the data were +250 ms, -180 ms, and -200 ms, for FNOC slices 1, 2, and 3, respectively. Predictions were only run for rays steeper than 5°; thus, axial portions at the top of each prediction are blacked out. Vertical alignment of predictions was made by matching arrival group spacing in the 0 s to -3 s regions as best as possible. Strong arrivals for the 1001 path are predicted but absent in the data. Alignment was completed by projecting the axial cut-off time onto the prediction. It is not clear why earlier arrivals are absent after day 201; this topic is still under study.

Figure 62 demonstrates the complexity of the Gulf Stream meander system. The position estimates for the Gulf Stream features along with its associated warm and cold rings is from OOC data for year day 201. Granted, these features move with time, but for purposes of this illustration assume they did not change from day 197 to day 204. One can see that during day 197 rays would cross the Gulf Stream once and on later days the rays make multiple front crossings. These multiple front crossings tend to “smear” the imaged position of the front. The dashed curve is the model response to a single front crossing model using feature positions from the OOC data base. The two naturally match in the year day 197 region, but on subsequent days the two are offset due to multiple front crossings and intervening ring structures. The solid curve is the Gulf Front location using the unsmoothed SURTASS axial arrivals (Figure 59). Warm and cold water velocities were chosen to align the curve on the left edge (morning of year day 197). Work toward using inversion techniques which use *a priori* knowledge of feature locations and error estimates is in progress. The purpose of this diagram is to illustrate that, given the source

and receiver geometry and the complicated configuration of the front and ring structures, an inversion with no *a priori* knowledge of changing meander configuration will not accurately image the Gulf Front.

In Figure 63 predicted axial arrival times are compared with the data. Figure 63 should be looked at in conjunction with Figure 62. The predicted times were calculated using all appropriate OOC feature positions for days 197 to 204. Two velocities were assigned to the features: 1491 m/s for Sargasso Water and warm-core rings, and 1483 m/s for cold water north of the Gulf Stream and cold-core rings. These features were assumed to extend vertically from the surface; that is, surface positions correspond to positions at depth. Identical range correction times were subtracted from the estimated times as from the data. As can be seen in Figure 63, the overall shape of the curve matches the envelope of axial arrivals but the two do not totally agree.

Starting from the left side and tracing to number 1 on the travel time plot, the data increase while the prediction times remain about flat. This increase in travel time corresponds to a displacement of the Gulf Front southward approximately 60 km (1 s deflection in time corresponds to about 200 km displacement in Gulf Stream position). At number 2, both travel time curves abruptly decrease because rays are passing through a portion of warm water behind the front. In the number 3 region, predicted time is about 300 ms greater than measured axial time. This is possibly due to differences in estimated position of the cold-core ring to the south or the weakening of its effect at depth. This discrepancy is still being looked at. The downward trend in predicted travel time at number 4 is due to a warm-core ring almost directly in line with the ship track. The downward trend in axial data seems to be less pronounced, but the gap in the data makes it difficult to determine. The upward trend in both travel time curves at number 5 is a result of rays being influenced by the cold meander loop to the south. The travel time data tend to decrease after number 5 because rays are skirting the bottom end of the loop.

The SURTASS data demonstrate the value gained from additional information obtained between shore stations. The data not only provide insight into signal response and frontal position between the fixed stations, but also provide axial arrival information

which is limited on shore receptions. Loss of all but axial arrivals after year day 201 is intriguing and will continue to be looked at. Although Gulf Stream complexities make estimating frontal position difficult, the use of *a priori* estimates will improve imaging. Future work with a number of sources will improve imaging. Receiver tracking error seems to be a major noise component; automatic P-code logging and improved array tracking would enhance data quality.

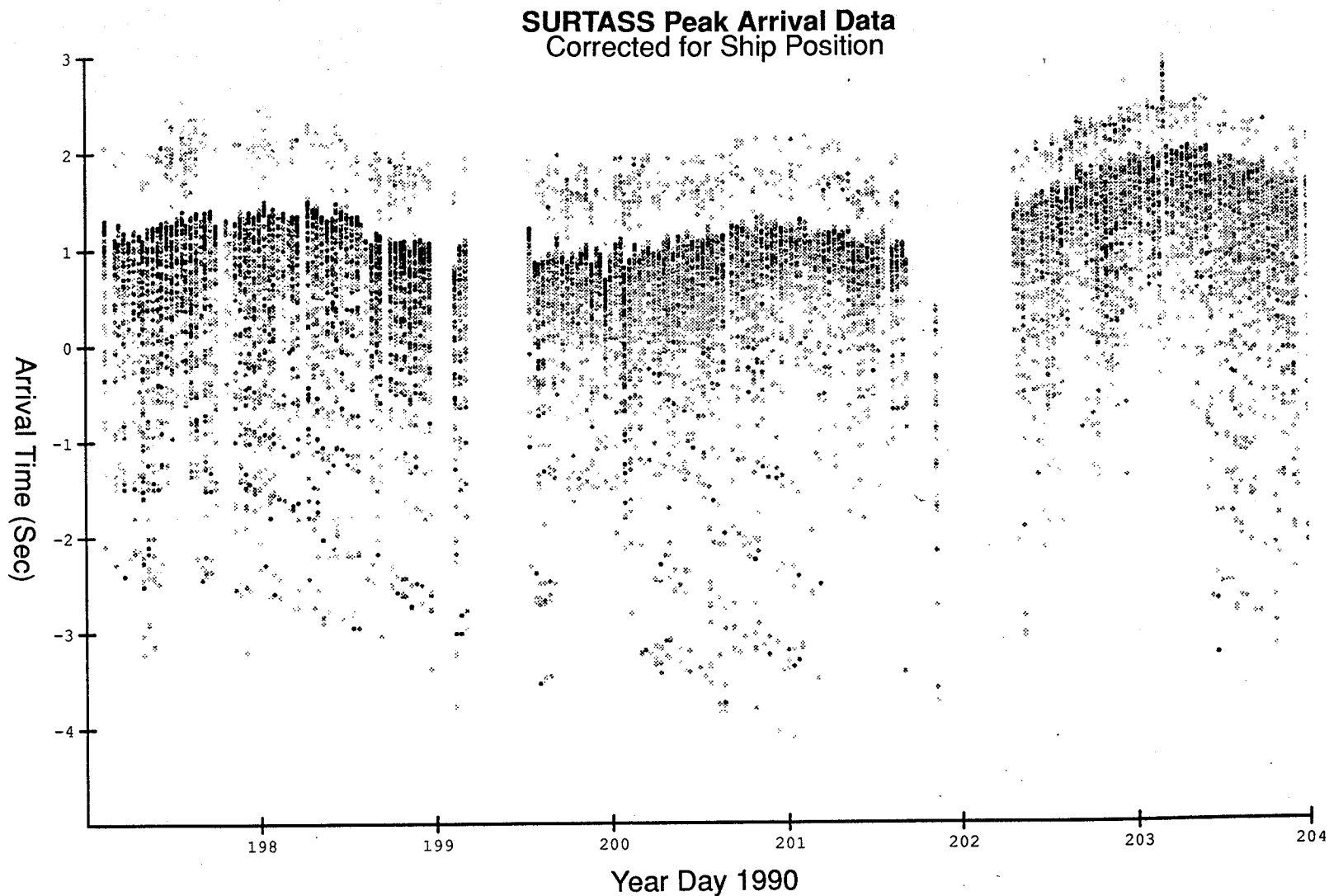


Figure 59. Arrival peaks after subtracting travel time to the array using a sound speed of 1492 m/s. Much of the "high frequency jitter" is probably due to array position error.

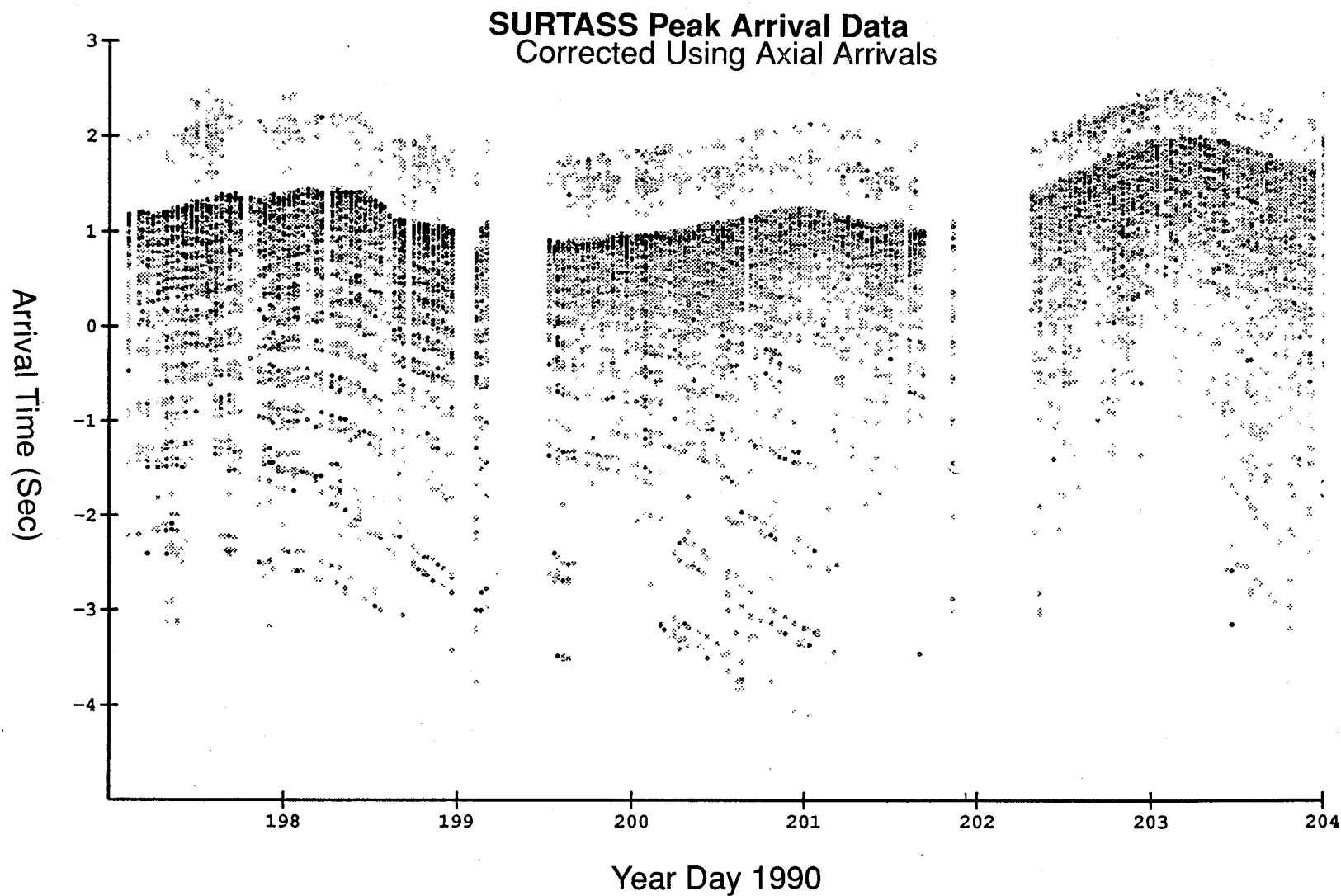


Figure 60. Peaks after smoothing. The axial cut-off was smoothed using a running average of five arrival sequences. This corresponds to about a 3.5 hour time period. Corrections were calculated by smoothing the axial cut over a five arrival window. Much of the jitter in arrivals has been removed. Although a particular arrival cannot be tracked, ray groups are more apparent.

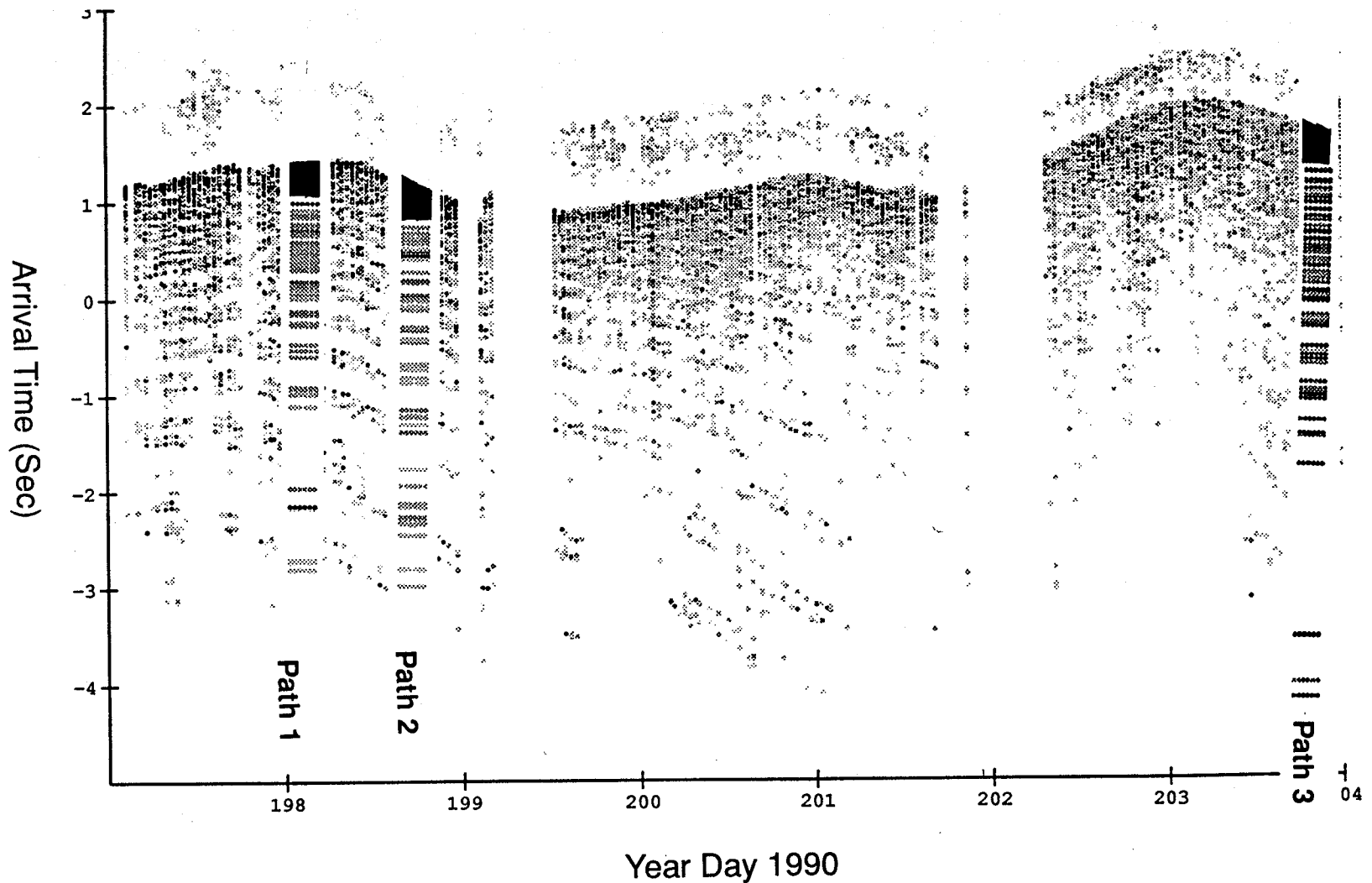


Figure 61. Comparison with the three ray trace simulations along FNOG slices. The simulations are inserted at the day number at which the ship crossed the FNOG slice paths. The ray trace models were only run for rays with angles greater than 5° , so some axial arrival information is not displayed (blacked-out portions of simulations). The simulations were aligned matching the spacing of the arrival groups as best as possible. The shift necessary to align the three predictions was not identical. Arrivals for the 1001 path are predicted, but are in weak agreement with the actual data.

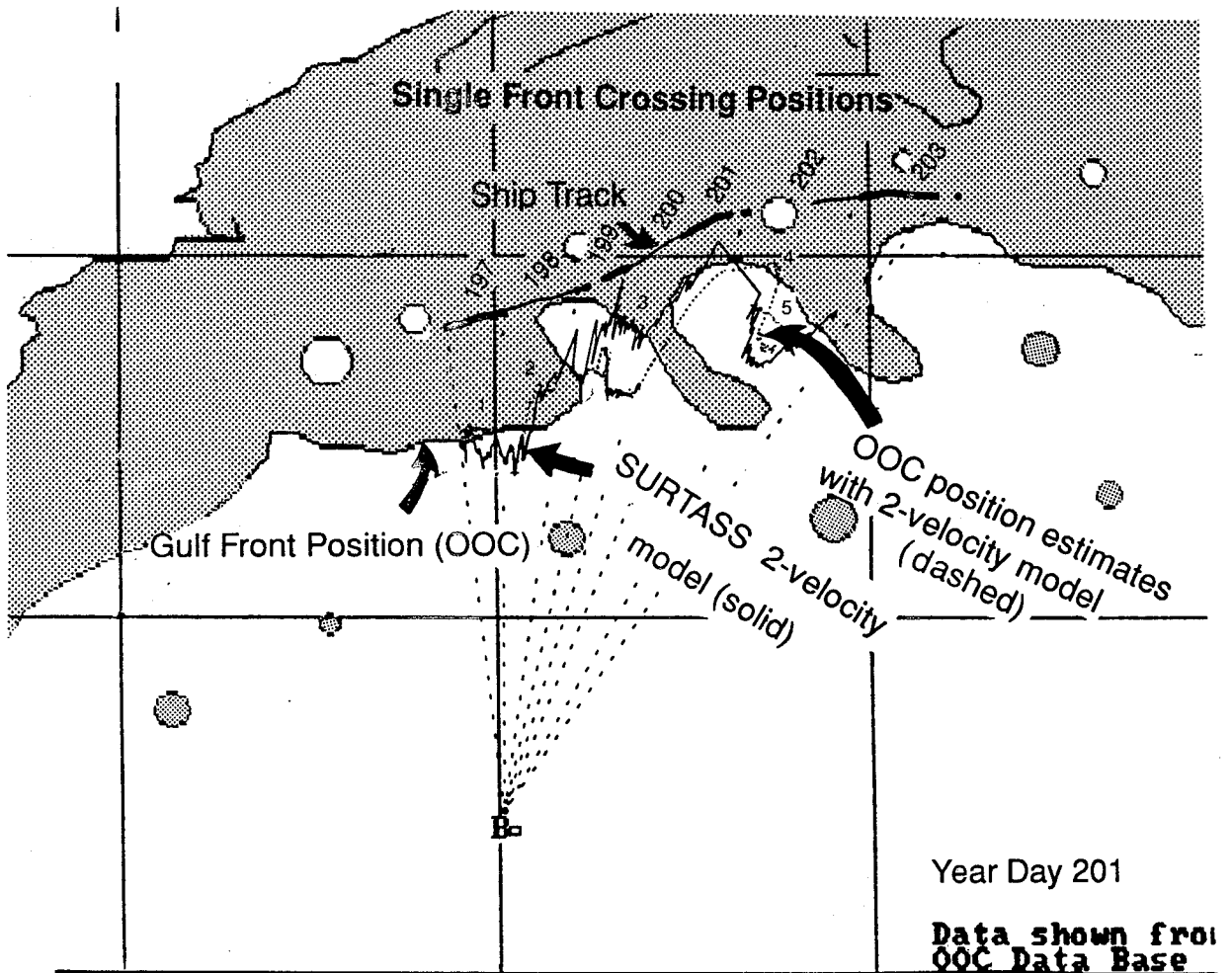


Figure 62. Figure demonstrating the complexity of the Gulf Stream meander system and how multiple front crossings of rays make estimating frontal location difficult. The OOC map is for year day 201. The dashed curve is the positional estimate for the Gulf Stream if rays are assumed to cross the front only once. The solid curve is estimated location using axial SURTASS data (same single front assumption). In both cases true frontal location is smeared. The true front location is more complex and best determined when rays transect the front only once.

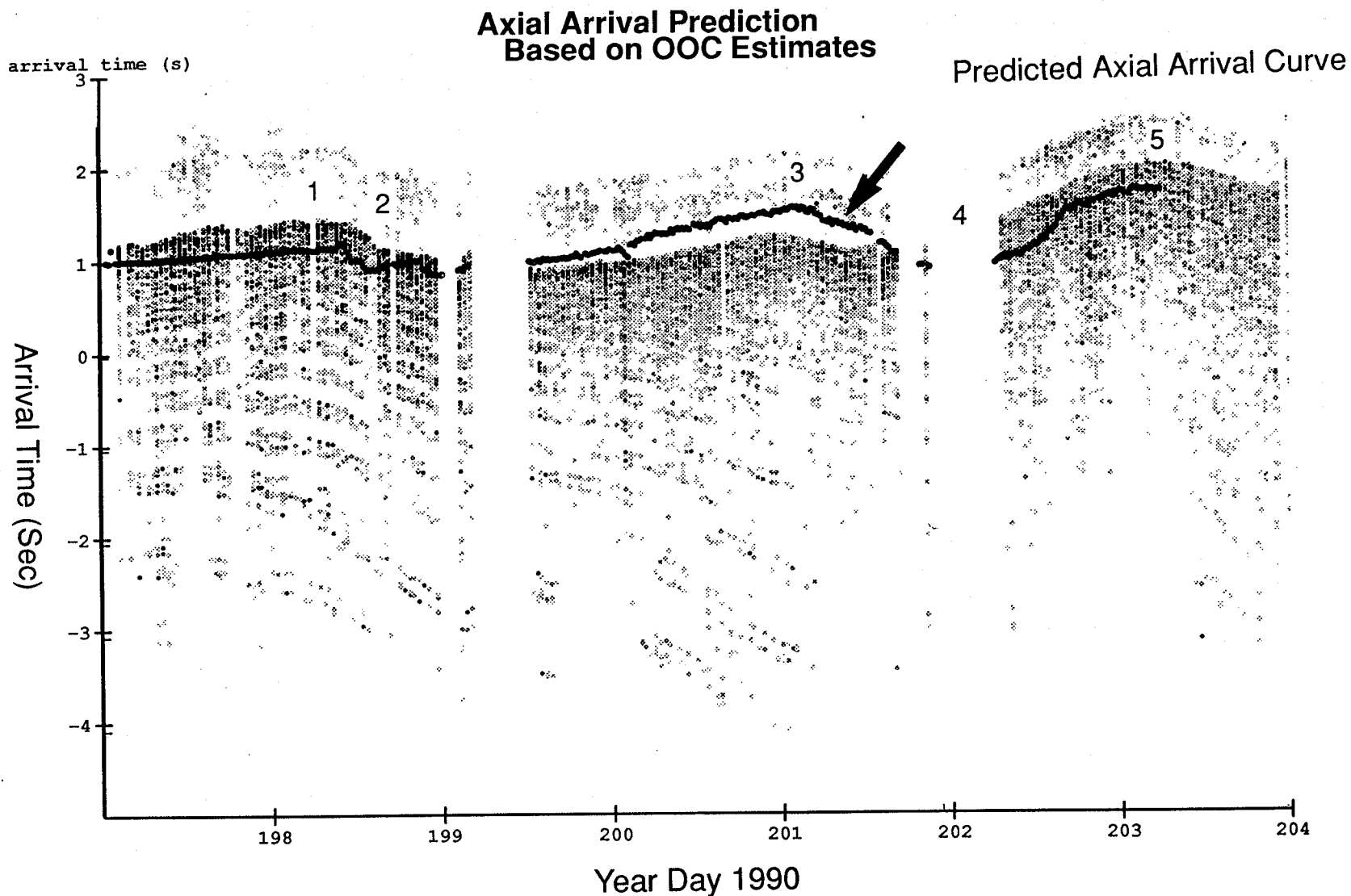


Figure 63. In this figure OOC positions were used to calculate travel times for the later axial arrivals. Two velocities were used and features were vertically infinite in extent. Cold water masses were assigned a velocity of 1483 m/s and warm masses a velocity of 1491 m/s. Temporal variation was accounted for by using the OOC estimates for the appropriate reception day. Ship position travel time subtracted from the data was likewise subtracted from the predicted times.

4. DISCUSSION

The purpose of this experiment was to demonstrate the mechanics of a real-time ocean monitoring system based on tomography and existing environmental data. The location of the experiment was chosen because of the large changes in acoustic travel times produced by the Gulf Stream and because FNOC produces nowcasts for this region. Unfortunately, along with this strong “signal” comes increased “noise” in the travel-time measurements. This means that localizations of the Gulf Stream were relatively easy, but the resolution of secondary features such as rings suffered from a lack of quality data.

The quantitative results of this experiment can be best understood if one thinks of the “tomography” configuration used in this particular experiment as an inverted echosounder (IES) turned on its side. The IES is an instrument that sits on the ocean bottom pinging at the surface and recording the round-trip travel time. If one assumes a two-layer ocean, with the sound speed (temperature) known in each layer, one can easily solve for changes in the depth of the interface between the two layers, the purpose of the IES. This is analogous to the ATE90 situation when only a simple, single front is present, i.e., Figure 35. (Had we been aware of the paucity of receivers in the region prior to our commitment to the experiment, we might have chosen a different location, thereby providing more than an IES-type measurement. Nevertheless, the basic mechanics of an ocean monitoring system have been demonstrated, the value to the Navy standard nowcast has been estimated, and the accuracy of the method has been confirmed by direct comparisons with the July AXBT data.)

When the frontal structure becomes more complicated, say by the addition of a warm-core ring, interpretation of the acoustic data becomes more difficult. Then we are almost entirely dependent on the validity of the error field supplied to us by FNOC. This error field tells the inversion process how to distribute the information in our, for all practical purposes, single travel time datum. Given this error field, the rigorous data inversion procedure we have used provides a quantitative measure of the “value added”—

how information in the data reduces the model uncertainty. Figure 52 shows that the reduction in error variance is typically 20%.

The error fields supplied by FNOC are a mix of subjective and objective analyses; in fact, we have had the dubious distinction of being the first users of these fields. Knowing the uncertainty of a field (and having confidence in this estimate of uncertainty) is as important as having an estimate of the field itself. We believe the greatest weakness in the OTIS analysis is in the accounting (or lack thereof) of the error in the OOC bogus analysis.

In the near future, we will be incorporating the data from the 1015 path with that from the 1006 path in a 3-D inverse to improve the horizontal resolution. This should improve the situation when a warm-core ring is present; a cold-core ring may still confuse the situation. In 1991, six AMODE acoustic moorings will be deployed between Bermuda and Puerto Rico. There should be several usable paths between these sources and the 06 and 15 receivers with which the horizontal resolution can be improved (Figure 64). Keep in mind that a true tomographic system should have many different paths crossing at many different angles (see Kak and Slaney, 1988).

One of the sore disappointments in this experiment was that we were unable to resolve arrivals of individual rays; only ray clusters were resolvable, with an attendant higher noise level—by an order of magnitude. This prevented the use of “loop harmonics” (see Cornuelle and Howe, 1987) to unambiguously resolve range-dependent information, such as frontal and ring positions. We had based our optimism on the interpretation of the 1981 data (Spiesberger et al., 1983) which implied that individual rays could be resolved. Individual rays could be resolved if the existing arrays were augmented with vertical arrays, drifters, towed arrays such as SURTASS, or some combination of these. If this is done, the information content of the data should increase an order of magnitude, because the travel time error can be reduced from roughly 20 ms rms to 5 ms rms (for a similar transmission schedule) and there will be more data; instead of 6 ray clusters, we should have 12 or more resolved rays. It is also possible that large travel

time variances were caused by a particularly energetic internal wave field or by strong small-scale features associated with the Gulf Stream frontal boundary. Resolution of individual rays is necessary to quantify the magnitude of different possible effects and their contribution to the overall travel time variance.

In our inversions, we have assumed that our initial reference state (the OTIS field from FNOC) is sufficiently close to the true state that we can assume linearity of the inverse problem. For rms errors of order 20 ms, which we have used, this does apply. If and when individual rays are resolved and smaller error bars are used, this assumption will have to be checked. Our feeling at this time is that the problem will remain linear, or that simple iteration will be adequate (see Mercer and Booker, 1983, and Spiesberger, 1985).

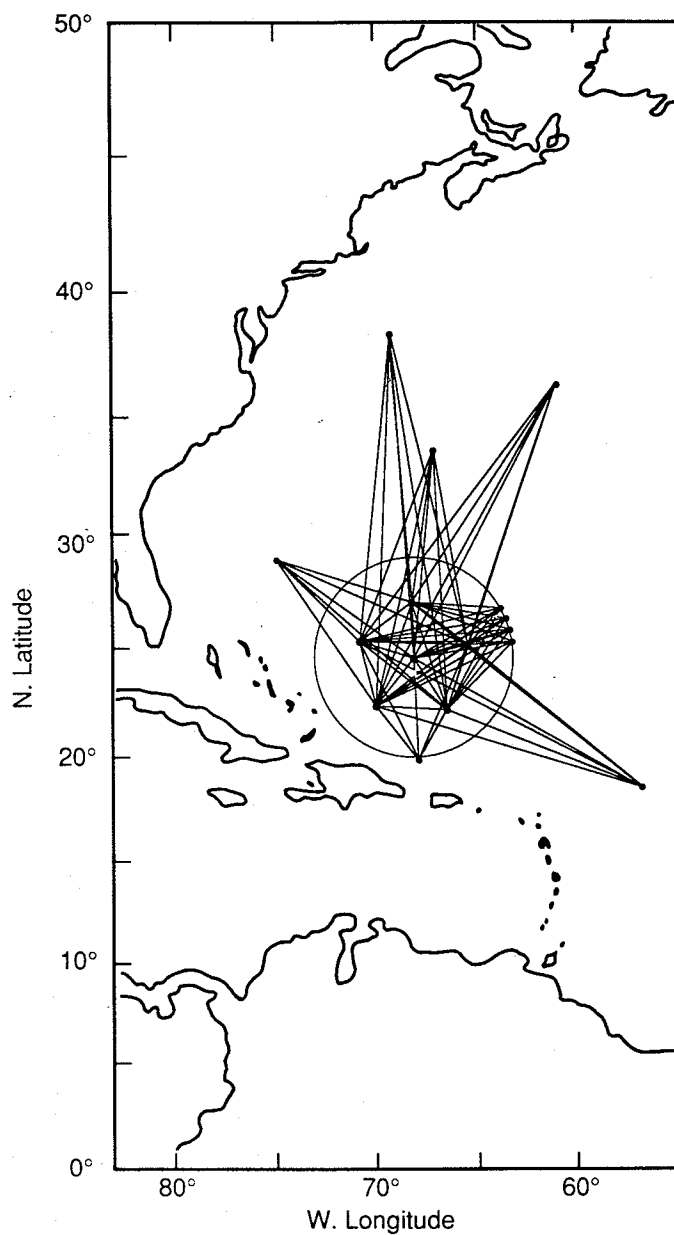


Figure 64. Map showing possible ray paths between the AMODE moorings and fixed receivers. Also shown is the expected track of the ship during the Moving Ship Tomography Experiment (the circle) and some of the paths associated with it.

5. CONCLUSIONS AND RECOMMENDATIONS

We list first the conclusions directly related to the oceanographic and acoustic parts of the experiment.

- (1) Measurements of acoustic travel time can accurately track movements of the Gulf Stream front. Errors are less than 10 km, substantiated by direct comparison with AXBT measurements (Figure 35). This conclusion applies only for the simple case of a single front.
- (2) When more complicated features such as rings are present, the acoustic travel time data can reduce the error variance of the Navy standard nowcast sound speed (temperature) field by 20% (Figure 52), but additional paths are required to localize the front to <10 km.
- (3) Acoustic predictions of sound speed fields calculated with and without tomographic data show differences of 10 dB and greater and convergence zone shifts of about 10 km (Figure 35).
- (4) With one or just a few horizontal paths, the simplest way to think of the experimental setup is in terms of an inverted echosounder. Effectively, only one travel time is measured, albeit with extremely good precision. How much information one can extract from this one datum depends on the complexity of the field.
- (5) Bottom mounting sources on steep slopes does not adversely affect the tomography signal and allows real-time analysis. The present site of source 10 on the northwest slope of Bermuda is a good one for a permanently cabled source.
- (6) Towed array data, even without the benefit of new array localization systems, agree well with crude predictions and show great promise for future ocean monitoring systems.

- (7) The absence of a coherent signal at the distant northeast receiver is unexplained.

Conclusions (1)–(3) quantify the “value added” to standard Navy products.

We draw these general conclusions about the “applied tomography system”:

- (1) The data-acquisition and signal-processing system is robust. With no burn-in period, only 4% of the data was lost because of equipment failure. Repairs could be effected remotely with minor assistance from personnel at the receiver stations.
- (2) The automated data transfer between the Navy facilities and APL-UW works well.
- (3) The data analysis at APL-UW is approaching the fully automated state. The weak points are two: first, matching the measured arrivals with the predicted rays still requires a person to check the identification, and, second, the data transfer between APL and FNOC needs automating.
- (4) The tomography inverse result depends heavily on the error estimates provided by FNOC.
- (5) Passing travel time data (or an estimated front location using the “rule-of-thumb”) to OOC did not work because of the difficulty in interpreting these data when the fronts and rings along the slice were complex.

Based on the foregoing conclusions, we make the following recommendations.

- (1) Continue and expand the present operation with battery-operated sources until cabled sources can be installed.
- (2) Make the inversions three dimensional (incorporate data from multiple receivers).

- (3) Improve the reporting of frontal errors by OOC. Each frontal location estimate should have an accurate time stamp and a position error estimate associated with it (preferably, the entire front should have an error covariance matrix associated with it). These improvements are impossible to incorporate with the present subjective analysis procedure. It is highly recommended that research be funded to make the image analysis objective. This objective analysis most likely must be coupled to other data analyses in an objective way, i.e., Kalman filtering. The OOC bogus analysis presently is the primary input to OTIS, and is likely to remain so, even when altimetry and tomography come on line. A global Ocean System cannot run on subjective analyses.
- (4) Modify OTIS to account for correlated frontal errors. This should be done independently of any tomography considerations.
- (5) Incorporate the present tomographic data stream into the operational OTIS run. Automate the data link.
- (6) Modify OTIS to assimilate travel times directly.
- (7) Instrument towed-array ships. Establish an operational communications link for tomography data.
- (8) Initiate the installation of cabled sources. The first sources should be placed off Bermuda where cables are available, on the northwest and southern-facing slopes. Initiate investigations as to subsequent locations. Cabled sources should be viewed as community resources.
- (9) Initiate development of inexpensive moored receivers and drifting buoys/hydrophone arrays with data telemetry to augment the receiver network.
- (10) Use vertical arrays to resolve individual rays.
- (11) Develop range-dependent internal wave predictions of acoustic parameters such as travel time and intensity.

- (12) Continue analysis of the data collected to date. Investigate the lack of a signal at the northeast receiver.
- (13) Instrument Pacific Navy facilities and install a source that is not bottom limited.
- (14) Form a working group to
 - provide a forum between modelers, data analysts, and experimentalists
 - pursue technical issues
 - assess progress and suggest future directions, reporting on both annually.

For the future, we envision a large number of fixed sources and receivers deployed in the Atlantic and other oceans to monitor the ocean weather. Figure 65 presents one idea for the deployment in the Atlantic Ocean. As additional measurement platforms, particularly towed sources and receivers and inexpensive receivers on moorings and drifters, become available, the detailed monitoring of ocean weather and climate should become a reality.

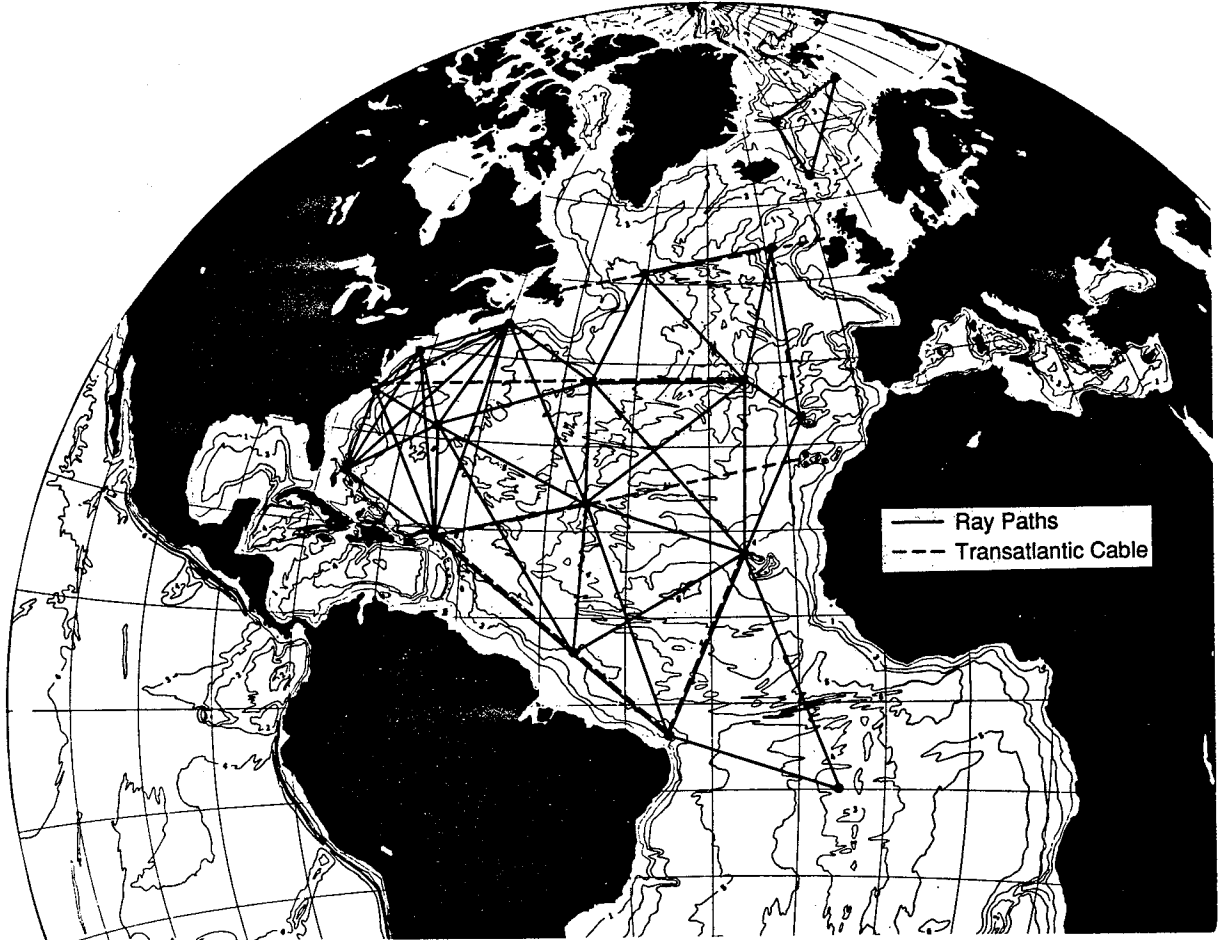


Figure 65. An idea for using applied tomography in the North Atlantic. Shown are fixed transceivers; additional coverage could be obtained by using sources and/or receivers on ships or drifters.

6. REFERENCES

- Aki, K., and P. G. Richards, *Quantitative Seismology*, 2 vols., Freeman, 932 pp., 1980.
- Boyd, J., and R. S. Linzell, Aircraft measurements in support of the Applied Tomography Experiment July 1990, NOARL Tech. Note 67, 1990a.
- Boyd, J., and R. S. Linzell, Aircraft measurements in support of the Applied Tomography Experiment September 1990, NOARL Tech. Note 86, 1990b.
- Chen, C., and F. J. Millero, Speed of sound in seawater at high pressures, *J. Acoust. Soc. Am.*, 62, 1129–1135, 1977.
- Cornuelle, B., and B. M. Howe, High spatial resolution in vertical slice ocean acoustic tomography, *J. Geophys. Res.*, 92, 11,680–11,692, 1987.
- Cornuelle, B., C. Wunsch, D. Behringer, T. Birdsall, M. Brown, R. Heinmiller, R. Knox, K. Metzger, W. Munk, J. Spiesberger, R. Spindel, D. Webb, and P. Worcester, Tomographic maps of the ocean mesoscale. Part 1: Pure acoustics, *J. Phys. Oceanog.*, 15, 133–152, 1985.
- Howe, B. M., P. F. Worcester, and R. C. Spindel, Ocean acoustic tomography: mesoscale velocity, *J. Geophys. Res.*, 92, 3785–3805, 1987.
- Kak, A. C., and M. Slaney, *Principles of Computerized Tomographic Imaging*, IEEE Press, New York, 1988.
- Menke, W., *Geophysical Data Analysis: Discrete Inverse Theory*, Revised Edition, Academic Press, San Diego, 1989.
- Mercer, J. A., and J. R. Booker, Long-range propagation of sound through oceanic mesoscale structures, *J. Geophys. Res.*, 88, 689–699, 1983.
- Munk, W., and C. Wunsch, Ocean acoustic tomography: a scheme for large scale monitoring, *Deep-Sea Res.*, 26A, 123–161, 1979.
- Ocean Tomography Group, A demonstration of ocean acoustic tomography, *Nature*, 299, 121–125, 1982.
- Spiesberger, J. L., Ocean acoustic tomography: Travel time biases, *J. Acoust. Soc. Am.*, 77, 83–100, 1985.
- Spiesberger, J. L., Remote sensing of western boundary currents using acoustic tomography, *J. Acoust. Soc. Am.*, 86, 346–351, 1989.

- Spiesberger, J. L., T. G. Birdsall, K. Metzger, R. A. Knox, C. W. Spofford, and R. C. Spindel, Measurements of Gulf Stream meandering and evidence of seasonal thermocline development using long-range acoustic transmissions, *J. Phys. Oceanog.*, 13, 1836–1846, 1983.
- Worcester, P. F., B. Dushaw, and B. M. Howe, Gyre-scale reciprocal acoustic transmissions, *Ocean Variability and Acoustic Propagation*, J. Potter and A. Warn-Varnas, Eds., Kluwer Academic, Boston, pp. 119–134, 1990.
- Worcester, P. F., D. A. Peckham, K. R. Hardy, and F. O. Dormer, AVATAR: Second-generation transceiver electronics for ocean acoustic tomography, *OCEANS'85 Conference Record*, IEEE, New York, pp. 654–662, 1985.

REPORT DOCUMENTATION PAGE

Form Approved
OMB No. 0704-0188

| | | | | | |
|--|-------|--|---|--|----------------------------|
| 1a. REPORT SECURITY CLASSIFICATION Unclassified | | | 1b. RESTRICTIVE MARKINGS | | |
| 2a. SECURITY CLASSIFICATION AUTHORITY | | | 3. DISTRIBUTION/AVAILABILITY OF REPORT Approved for public release; distribution is unlimited. | | |
| 2b. DECLASSIFICATION/DOWNGRADING SCHEDULE | | | | | |
| 4. PERFORMING ORGANIZATION REPORT NUMBER(S) APL-UW TR 9106 | | | 5. MONITORING ORGANIZATION REPORT NUMBER(S) | | |
| 6a. NAME OF PERFORMING ORGANIZATION Applied Physics Laboratory University of Washington | | 6b. OFFICE SYMBOL (If applicable) | | 7a. NAME OF MONITORING ORGANIZATION | |
| 6c. ADDRESS (City, State, and ZIP Code) 1013 N.E. 40th Street Seattle, WA 98105-6698 | | | 7b. ADDRESS (City, State, and ZIP Code) | | |
| 8a. NAME OF FUNDING/SPONSORING ORGANIZATION ASW Environmental Acoustic Support (AEAS) | | 8b. OFFICE SYMBOL (If applicable) 124A | | 9. PROCUREMENT INSTRUMENT IDENTIFICATION NUMBER SPAWAR N00039-88-C-0054 | |
| 8c. ADDRESS (City, State, and ZIP Code) Ballston Tower 800 N. Quincy Street Arlington, VA 22217-5000 | | | 10. SOURCE OF FUNDING NUMBERS | | |
| | | | PROGRAM ELEMENT NO. PE63785N | PROJECT NO. R0120 | TASK NO. |
| 11. TITLE (Include Security Classification) The Applied Tomography Experiment of 1990 | | | | | |
| 12. PERSONAL AUTHOR(S) | | | | | |
| 13a. TYPE OF REPORT Technical | | 13b. TIME COVERED FROM 3/90 TO 9/90 | | 14. DATE OF REPORT (Year, Month, Day) 28 February 1991 | |
| 15. PAGE COUNT 120 | | | | | |
| 16. SUPPLEMENTARY NOTATION | | | | | |
| 17. COSATI CODES | | | 18. SUBJECT TERMS (Continue on reverse if necessary and identify by block number) | | |
| FIELD | GROUP | SUB-GROUP | Acoustic travel time Gulf Stream Sound speed | | |
| 20 | 01 | | Applied tomography Ocean temperature field | | |
| 08 | 03 | | | | |
| 19. ABSTRACT (Continue on reverse if necessary and identify by block number) | | | | | |
| <p>The feasibility of an operational tomography capability has been demonstrated. Daily inversions of acoustic travel time data produced sound speed profiles that were successfully integrated into the standard Navy operational product for the NW Atlantic. Improved estimates of the sound speed (and thus temperature) reduced the error variance approximately 20% along the source-receiver vector. The resultant temperature fields, produced on a daily basis, have been reformulated as synthetic bathythermographs for input to the Optimal Thermal Interpolation System at the Fleet Numerical Oceanography Center. Sound speed fields based on tomographic results change predicted convergence zone ranges by about 10 km, with corresponding changes in the local acoustic intensity of 10 dB or greater. In addition, acoustic transmissions from Bermuda through the Gulf Stream were used to estimate the position of the Gulf Stream in real time. The precision (using air-dropped expendable</p> <p style="text-align: right;">(cont.)</p> | | | | | |
| 20. DISTRIBUTION/AVAILABILITY OF ABSTRACT <input checked="" type="checkbox"/> UNCLASSIFIED/UNLIMITED <input checked="" type="checkbox"/> SAME AS RPT. <input type="checkbox"/> DTIC USERS | | | 21. ABSTRACT SECURITY CLASSIFICATION Unclassified | | |
| 22a. NAME OF RESPONSIBLE INDIVIDUAL Robert Feden | | | 22b. TELEPHONE (Include Area Code) (703) 696-6939 | | 22c. OFFICE SYMBOL 124A |

20, cont.

bathythermograph (AXBT) data as ground truth) is better than 10 km under certain circumstances. This information can be used by the Operational Oceanography Center to improve estimates of Gulf Stream frontal location, which are presently based on IR satellite images. The transmissions from Bermuda northward are continuing. The deployment of six acoustic sources south of Bermuda in 1991 will improve the horizontal resolution. Recommendations are given for future work.